Fluid and kinetic aspects of collissionless magnetic reconnection

Citation for published version (APA):
Valori, G. (2001). *Fluid and kinetic aspects of collissionless magnetic reconnection*. [Phd Thesis 1 (Research TU/e / Graduation TU/e), Applied Physics and Science Education]. Technische Universiteit Eindhoven. https://doi.org/10.6100/IR554069

DOI:
10.6100/IR554069

Document status and date:
Published: 01/01/2001

Document Version:
Publisher’s PDF, also known as Version of Record (includes final page, issue and volume numbers)

Please check the document version of this publication:

• A submitted manuscript is the version of the article upon submission and before peer-review. There can be important differences between the submitted version and the official published version of record. People interested in the research are advised to contact the author for the final version of the publication, or visit the DOI to the publisher's website.
• The final author version and the galley proof are versions of the publication after peer review.
• The final published version features the final layout of the paper including the volume, issue and page numbers.

Link to publication

General rights
Copyright and moral rights for the publications made accessible in the public portal are retained by the authors and/or other copyright owners and it is a condition of accessing publications that users recognise and abide by the legal requirements associated with these rights.

- Users may download and print one copy of any publication from the public portal for the purpose of private study or research.
- You may not further distribute the material or use it for any profit-making activity or commercial gain
- You may freely distribute the URL identifying the publication in the public portal.

If the publication is distributed under the terms of Article 25fa of the Dutch Copyright Act, indicated by the “Taverne” license above, please follow below link for the End User Agreement:

www.tue.nl/taverne

Take down policy
If you believe that this document breaches copyright please contact us at:

openaccess@tue.nl

providing details and we will investigate your claim.

Download date: 07. Jul. 2024

Fluid and kinetic aspects of collisionless magnetic reconnection

PROEFSCHRIFT

ter verkrijging van de graad van doctor aan de
Technische Universiteit Eindhoven, op gezag van de
Rector Magnificus, prof.dr. R.A. van Santen, voor een
commissie aangewezen door het College voor
Promoties in het openbaar te verdedigen op
maandag 17 december 2001 om 16.00 uur

door

Gherardo Valori

geboren te Montecatini Terme, Italië

Dit proefschrift is goedgekeurd door de promotoren:

prof.dr.ir. T.J. Schep
en
prof.dr. F.W. Sluijter

Copromotor:
dr. H.J. de Blank

Fluid and kinetic aspects of collisionless magnetic reconnection
by Gherardo Valori, 2001
Proefschrift – ISBN 90-9015313-6
Subject headings: plasma dynamics / magnetic reconnection

Druk: Print Partners Ipskamp, Enschede

The work described in this thesis was performed as part of the research program of the ‘Stichting voor Fundamenteel Onderzoek der Materie’ (FOM) with financial support of the ‘Nederlandse Organisatie voor Wetenschappelijk Onderzoek’ (NWO) and Euratom, and was carried out at the ‘FOM-Instituut voor Plasmafysica Rijnhuizen’ in Nieuwegein, The Netherlands.

Contents

1 Introduction **9**
- 1.1 Plasmas and magnetic reconnection 9
  - 1.1.1 Small scale effects in a plasma 9
  - 1.1.2 Flux conservation and its violation 11
  - 1.1.3 Singularities in the MHD description 12
  - 1.1.4 Reconnection in non collisional plasmas 13
- 1.2 Stationary reconnection 14
- 1.3 Reduction to slab geometry 17
- 1.4 Effects of temperature gradients on reconnection 17
- 1.5 This thesis 18

Part One: Fluid Theory **21**

2 The drift-Alfvén two fluid model **23**
- 2.1 The two fluid model 23
  - 2.1.1 Electron fluid 24
  - 2.1.2 Ion fluid 25
- 2.2 The drift-Alfvén two fluid model 26
- 2.3 Hamiltonian structure 28

3 Linear theory of the drift-Alfvén model **31**
- 3.1 Taylor's problem 31
  - 3.1.1 The external solution 32
  - 3.1.2 Solution in the reconnection layer 34
  - 3.1.3 The linear picture of forced reconnection 43
- 3.2 Unstable perturbations 44
- 3.3 Tokamaks and slabs, kink and tearing modes 45
- 3.4 Non stationary solution 46
  - 3.4.1 Ideal, non stationary solution 47
  - 3.4.2 Small scale, non stationary solution 47

4 Nonlinear dynamics **49**
4.1 The numerical implementation 50
4.2 The forced case 52
4.2.1 Reconnection on the scale of d_e 54
4.2.2 Ion sound gyroradius effects 61
4.2.3 Asymmetric forcing 70
4.3 Collisionless reconnection in instabilities and due to external forcing 73
4.3.1 Introduction 74
4.3.2 The model. 75
4.3.3 Numerical calculations. 76
4.3.4 Large-scale behavior. 78
4.3.5 Scale collapse. 82
4.3.6 Discussion and conclusions. 85

Part Two: Kinetic Theory **87**

5 The kinetic model for drift-Alfvén perturbations **89**
5.1 Introduction 89
5.2 The Drift-Alfvén kinetic model 90
5.3 Lagrangian form 91

6 Reconnection of flux tubes with different temperatures **93**
6.1 The governing equations 93
6.2 Steady state reconnection. 93
6.3 Discussion. 98

7 Finite size island and kinetic effects **99**
7.1 Introduction 99
7.2 Linearized equations 100
7.3 Coordinate system with straight field lines 101
7.4 Fourier expansion along field lines 103
7.5 Final set of linearized equations 104
7.6 Dispersion relation 106
7.6.1 The method of asymptotic regions 106
7.6.2 Electron region 108
7.6.3 Fluid-like region 113
7.7 Discussion 115

8 Conclusions **117**
8.1 Fluid and kinetic descriptions 117
8.2 Results presented in this thesis 118
8.3 Outlook 120

Appendices **123**

A Collisional fluid model **125**
A.1 Transport coefficients 125
A.2 Collisional electron equations 127
A.3 Formal limit of low collisionality 128

B The metric tensor $\mathrm{g}(\hat{\psi}, \hat{\lambda})$ **131**
B.1 Notation 131
B.2 The metric coefficients 131
B.3 Fourier series 133

References **139**

Summary **143**

Samenvatting **147**

Curriculum Vitae **151**

Acknowledgements **153**

1. Introduction

1.1 Plasmas and magnetic reconnection

Plasmas are systems of ionized gases in which collective effects due to self-generated or external electric and magnetic fields are more important than direct interactions between charged particles. The electrostatic interaction energy between charged particles is much smaller than their kinetic energy. According to these definitions, many system are ”plasmas” that are apparently very different: the interstellar gas, the solar corona, the earth magneto-tail, the inside of a burning tokamak, the lightening gas in the bulb of a lamp, and many others.
In the presence of a strong magnetic field, charged particles follow trajectories that are, to first approximation, helices around magnetic field lines (gyration). This is the manifestation of the Lorentz force which acts on a charged particle due to its motion perpendicular to the direction of the magnetic field. Plasmas are said to be strongly magnetized if the phenomena of interest have frequencies well below the gyrofrequencies and scale lengths much larger than the gyroradii of the composing particles.
The individual interaction between charged particles are called Coulomb collisions (or just: collisions). In hot plasmas Coulomb collisions are rare, and the mean free paths are long, yielding an almost unconstrained particle streaming along field lines.

From the considerations above it follows that the description of the particle transverse motions in strongly magnetized plasmas is equivalent, in first approximation, to the description of the motion of field lines.
These considerations form the basis for the concept of confinement of hot plasmas for nuclear fusion purposes by means of magnetic fields that lie in closed toroidal surfaces.

1.1.1 Small scale effects in a plasma

The description of large scale phenomena in a plasma can be done using the single fluid model called ideal magneto-hydrodynamics (MHD). This model provides a description on global scales of a perfectly conducting plasma, including the effects of ion inertia, pressure and the electromagnetic field. The ideal MHD equations are characterized by two scales only. These are the size of the system, L_0, and the time scale associated with the background magnetic field, the Alfvén time $\tau_A \equiv L_0/v_A$, where $v_A \equiv B_0/\sqrt{4\pi n m_i}$ is called Alfvén velocity. If the equations are normalized to L_0 and τ_A, then no other time or length scale remains in them. This implies that ideal MHD does not set any limit to the creation of small scales. Small scale effects may drastically alter the plasma picture provided by the ideal description. As is explained in details in the following sections, this is precisely what happens in the case of magnetic reconnection. Coulomb collisions, the small but finite mass of electrons, the electron pressure variations along field lines, and resonance phenomena between waves and particles are the small scale effects considered in this thesis which extend ideal MHD.

In order to address the issue quantitatively we adopt the MHD model where the fluid velocity $\mathbf{v}$ and the electromagnetic field are related by Ohm's law [1],

$$\mathbf{E} + \frac{1}{c}\mathbf{v} \times \mathbf{B} = \eta \mathbf{J}. \tag{1.1}$$

The left hand side of this equation is an ideal fluid equation, while on the right hand side the resistivity, η, is a dissipative effect associated with small scales. This is shown as follows. In order to express the time scale associated with resistivity we use Maxwell's equations,

$$-\frac{1}{c}\frac{\partial \mathbf{B}}{\partial t} = \nabla \times \mathbf{E}, \qquad \frac{4\pi}{c}\mathbf{J} = \nabla \times \mathbf{B}, \qquad \nabla \cdot \mathbf{B} = 0, \tag{1.2}$$

to derive an evolution equation for the magnetic field. The displacement current was neglected in Eq. (1.2) because the time scale of interest is slow compared to that of electromagnetic waves ($\tau \ll c/L_0$). Using the first of Eq. (1.2) in Eq. (1.1) and assuming uniform resistivity we have

$$\frac{\partial \mathbf{B}}{\partial t} = \nabla \times (\mathbf{v} \times \mathbf{B}) + \frac{c^2}{4\pi}\eta \nabla^2 \mathbf{B}. \tag{1.3}$$

Here the two terms on the right hand side relate to the flow and to the magnetic diffusion, respectively. A resistive time scale can be defined as $\tau_\eta \equiv L_0^2 c^2/4\pi\eta$. If Eq. (1.3) is normalized to L_0 and v_A then the coefficient of the resistive term is multiplied by the inverse of the Lundquist number, $S \equiv \tau_\eta/\tau_A$.
The Lundquist number, S, measures the relative importance of the flow with respect to magnetic diffusion. Two opposite limits of S characterize Eq. (1.3). If $S \ll 1$ then the above equation reduces to

$$\frac{\partial \mathbf{B}}{\partial t} = \frac{L_0^2}{\tau_A S}\nabla^2 \mathbf{B} \tag{1.4}$$

a diffusion equation in which the flow does not influence appreciably the magnetic field evolution. The time scale associated with the magnetic field evolution, τ_η, depends linearly on the inverse of resistivity. The resistivity η is a rapidly

decreasing function of the temperature and therefore is small in high temperature plasmas.
However, many astrophysical and laboratory plasmas display phenomena accompanied by magnetic field rearrangement on time scale several orders of magnitude smaller than the diffusion time based on the macroscopic scale L_0, suggesting that in fact much shorter scales are created in the system.
The opposite limit of large Lundquist numbers is, in fact, more relevant for high temperature plasmas. In this case Eq. (1.3) reads

$$\frac{\partial \mathbf{B}}{\partial t} = \nabla \times (\mathbf{v} \times \mathbf{B}) \tag{1.5}$$

which corresponds to the ideal limit of vanishing resistivity in Eq. (1.1). As a consequence, in this ideal limit the electric field component parallel to the magnetic field also vanishes,

$$\mathbf{E}_{\parallel} = 0 \tag{1.6}$$

as it follows from Eq. (1.1) for $\eta = 0$.

1.1.2 Flux conservation and its violation

As the Alfvén theorem [2] proves, Eq. (1.5) implies a very remarkable property: the time derivative of the magnetic flux through a surface moving with the fluid velocity vanishes. More pictorially, magnetic field lines (thin flux tubes) are said to be frozen into the fluid elements, in the sense that a field line will follow the very same fluid element in its motion. The important consequence of this property is that, if the ideal condition pertains everywhere in the plasma, then the magnetic field topology cannot be changed by the plasma dynamics (flux conservation). For this reason Eq. (1.5) it is often referred to as a “frozen-in” law for the magnetic field.
A simple example [3] may help to clarify the underlying mechanism. Imagine that a fluid element is driven with velocity v_x through a static magnetic field B_y with no electric field present. According to Eq. (1.1), a current $J_z = v_x B_y/\eta$ will be generated, which in turn exerts a Lorentz force $F_x = -v_x B_y^2/\eta$ on the fluid itself, counteracting the fluid displacement. This force diverges for $\eta = 0$. Hence, in an ideally conducting plasma it is not possible to move a fluid element across the field lines without generating arbitrary large currents. On the other hand, this force vanishes where B_y vanishes, regardless of the value of η. So locations where the field vanishes are the only ones where fluid motions are not constrained by magnetic field lines.

Regions in which the plasma motion and the field lines are decoupled are called reconnection layers. In a reconnection layer a suitable perturbation can induce field lines to ”reconnect”: field lines which were topologically distinct due to Eq. (1.5) can be connected together. From this point of view resistivity causes local violations of the topological constraint inherent in Eq. (1.5).

The consequences of reconnection are nevertheless global. Indeed, magnetic field lines affect globally the plasma because they extend through regions of space that can be very far apart. Then magnetic reconnection can have important consequences on particles and energy flows. Firstly, we already identified particle trajectories and field lines. Reconnected field lines put in contact regions of space inaccessible for particles in the ideal limit. In this way they alter the particle flows set up by the ideal dynamics. Secondly, the change of the magnetic topology can allow the perturbation to tap energy that was unavailable in the ideal limit.

1.1.3 Singularities in the MHD description

Flux conservation is maintained if any force acting perpendicularly to the field lines is included in Eq. (1.1). Hence, the parallel dynamics is the essential one in the study of magnetic reconnection mechanisms. In the case of violation of flux conservation due to collisions, only the parallel resistivity plays a role.

Magnetic reconnection is a local violation of flux conservation. Generalizing the picture sketched in Section 1.1.2, in arbitrary geometry the violation of flux conservation takes place where the ideal term on the right hand side of Eq. (1.3) becomes small. For an incompressible plasma this happens where $\mathbf{B} \cdot \nabla = 0$. Regions of space where $\mathbf{B} \cdot \nabla = 0$ are locations where small scale terms become important, and magnetic field and fluid motion decouple. These regions are the reconnection layers.

In the ideal limit of Eq. (1.1), an arbitrary function $-\nabla\Phi$ can be added to the electric field $\mathbf{E} = -\mathbf{v} \times \mathbf{B}/c$ without affecting flux conservation. Then, the parallel component of the electric field satisfies $\mathbf{B} \cdot \mathbf{E} = -\mathbf{B} \cdot \nabla\Phi$, which is called [4] magnetic differential equation for the scalar Φ. It is a nonlocal equation for Φ, its solution depending on boundary conditions. For instance, in a closed (toroidal) magnetic configuration, where the field lines are confined to a finite volume, different boundary conditions may apply to field lines which cover a toroidal surface ergodically or which close upon themselves after a finite number of windings around the torus. Closed field lines with the same winding number q form the so-called rational surfaces in tokamaks. In this case the solution to the magnetic differential equation is regular if the integral over the closed field line of the electric field (the “loop voltage”) vanishes. If this happens for all closed field lines then the flux is conserved. However, the loop voltage is in general finite for arbitrary plasma motions. Hence, rational surfaces are locations where violation of flux conservation can take place.

If resistivity is retained, the parallel component of the electric field is given by

$$\mathbf{E}_{\|} = \eta \mathbf{J}_{\|}. \tag{1.7}$$

The smallness of the resistivity coefficient implies that a large current is required in order to keep the loop voltage finite. This current tends to diverge for vanishing resistivity.

The condition $\mathbf{B} \cdot \nabla = 0$ may hold on entire surfaces, called “neutral surfaces”. This can happen for instance if the plasma equilibrium possesses a continuous symmetry, such as the rotational symmetry of a torus. In the case treated in Chapter 3 of this thesis, the equations describing the plasma in the ideal limit allow for discontinuous solutions across neutral surfaces. In the thin reconnection layer around a neutral surface small scale effects become important.

1.1.4 Reconnection in non collisional plasmas

The resistive diffusion rate depends linearly on the resistivity, η, as explained in Eq. (1.4). As we will see in the next section and in Chapter 3, in reconnecting systems the localization of the reconnection process itself can lead to the formation of small scale length structures, depending on η. The net result of such a relation, according to a variety of theoretical models, is the dependence of the reconnection rate on some fractional power of the resistivity, and a much faster process than simple diffusion. Nevertheless, resistivity is a rapidly decreasing function of temperature. It follows that reconnection rates due to resistivity are lower and lower for higher temperature.

For a long time reconnection allowed by resistivity was considered to be the only interesting mechanism for magnetic topology rearrangements. Other mechanisms were known since the first studies on reconnection, see for instance [5], but they were not relevant for the parameters regimes of fusion machines of the time. However, discrepancies between theoretical models and experimental observations became wider and wider with the progress of fusion devices [6]. Inadequacies of the resistive scalings of magnetic reconnection were also coming from studies of the earth magneto-tail [7].

Broadly speaking, the main obstacle that reconnection models had to face was to explain the very high rates of reconnection observed in some hot, diluted plasmas [6] where resistivity was too small to give the correct growth rate. For this reason effects other then resistivity will dominate in Ohm’s law.

For higher and higher temperatures the resistive layer becomes comparable or even smaller than the electron inertial skin depth, $d_e \equiv c/\omega_p$, where ω_p is the electron plasma frequency. The inclusion of inertial terms into the momentum balance equation (generalized Ohm's law) leads to [1]

$$\mathbf{E} + \frac{1}{c}\mathbf{v} \times \mathbf{B} = \eta \mathbf{J} - \frac{m_e}{e}\left(\frac{\partial \mathbf{v}}{\partial t} + \mathbf{v} \cdot \nabla \mathbf{v}\right). \tag{1.8}$$

Here $\mathbf{v}$ is the electron fluid velocity. Discarding η and using Maxwell's equations, instead of Eq. (1.3) we have now the equation

$$\frac{\partial \boldsymbol{\Omega}}{\partial t} = \nabla \times \Big(\mathbf{v} \times \boldsymbol{\Omega}\Big), \qquad \boldsymbol{\Omega} \equiv \mathbf{B} - \frac{c m_e}{e} \nabla \times \mathbf{v}. \tag{1.9}$$

This equation is a frozen-in law for the generalized vorticity $\boldsymbol{\Omega}$. Although the generalized vorticity $\boldsymbol{\Omega}$ is frozen into the flow, the magnetic field is not. Hence, magnetic reconnection is possible via a balance between the modifications of magnetic field and vorticity, $\nabla \times \mathbf{v}$. In Chapter 3 and Chapter 4 it is shown how the inclusion of electron inertia allows to drive the reconnection of magnetic field lines. The drive for reconnection is either an external forcing or an instability.
The reconnection allowed by electron inertia is not a dissipative effect such as resistivity. It is actually important in temperature and density regimes where collisions are negligible. Since the generalized vorticity $\boldsymbol{\Omega}$ must be conserved during the reconnection of magnetic field lines, this influences the possible dynamical evolution of the system. A Hamiltonian formulation of the governing equations is possible in some cases (see Section 2), thus the name ”Hamiltonian reconnection” for the reconnection allowed by the inertial terms in the momentum balance equation. We reserved the broader ”collisionless reconnection” for the reconnection due to kinetic effects, as introduced in Section 1.4.

In order to give a more quantitative comparison between reconnection allowed by resistive and inertial effects we now turn our attention to a model for stationary reconnection.

1.2 Stationary reconnection

A simple example of a reconnection model is that of Sweet-Parker [8]. In the present section this model is extended to include electron inertia, and it is used to compare the time and length scales of reconnection allowed by resistivity and electron inertia.
The model of Sweet-Parker describes a two dimensional, stationary reconnection process. Anti-parallel magnetic field components are carried by the flow (upstream or inflow) toward a neutral surface. This compression increases the field line density at the neutral surface where small scale effects violate flux conservation and allow for reconnection. The flow is then ejected along the neutral line

(downstream or outflow), carrying away field lines that have been reconnected. This model is applicable whenever the time scale in which field lines are compressed towards the neutral line is comparable with the reconnection time scale. Some features of this model are recognized in the nonlinear results presented in Chapter 4.

The geometry of the problem is the following. A neutral line, say along $x = 0$, is surrounded by a reconnection layer of length 2Δ and width 2δ, where the width is measured along x. Outside the reconnection layer ideal conditions hold, so the magnetic field lines are frozen in the fluid. The inflow are streams with constant velocity u parallel to x which carry field lines toward the layer. In the inflow regions the magnetic field, B_0, is in the y direction, constant and it is taken to be anti-parallel and equal in strength on opposite sides of the layer. The geometry is such that the origin is also a stagnation point for the flow. The fluid is then ejected through the sides δ, parallel to the y axis, symmetrically with respect to $y = 0$. These outflow streams have constant velocity v.

The problem can be formulated as follows: given that inside the reconnection layer the small scales effects are resistivity and electron inertia, which are the reconnection rate and dimensions of the reconnection layer?

The answer is found using the conservation of mass and the conservation of energy between inflow and outflow, and the component along z of Eq. (1.8) inside the reconnection layer. Due to the symmetry of the configuration, one may consider one quadrant only.

For an incompressible fluid, the mass entering the layer per unit time, $nm_iu\delta$, must balance the ejected mass by the outflow per unit time, $nm_iv\delta$. Thus, mass conservation yields directly

$$u\Delta = v\delta. \tag{1.10}$$

For the energy conservation three assumptions are made. The first one is that the energy in the outflow and in the inflow are approximately the same. The second assumption is that the velocity in the inflow is smaller than the Alfvén velocity, which can be verified *a posteriori*. The last assumption is that the energy in the outflow close to the layer is mainly kinetic.

The energy entering the layer per unit time is mainly magnetic, so $(B_0^2/8\pi)u\Delta$ has to balance the kinetic energy leaving the layer, $(nm_iv^2/2)v\delta$. Hence, energy conservation yields that the outflow velocity is equal to the Alfvén velocity,

$$v = v_A \tag{1.11}$$

From the the two relations above follows that $\delta/\Delta = u/v_A$.

Finally, consider the component along z of the momentum balance equation, Eq. (1.8). The configuration is stationary, then the z component of the electric field is constant. Outside the layer, where the right hand side of Eq. (1.8) is small, it is $E_z \sim uB_0/c$. The same expression for E_z is taken inside the layer. Inside the layer the $\mathbf{v} \times \mathbf{B}$ term is negligible. The current along z is given by the rotation of the magnetic field, $J_z \sim cB_0/4\pi\delta$. Taking $J_z \sim -env_z$, it follows that $\mathbf{v} \cdot \nabla v_z \sim -cuB_0/4\pi\delta^2 en$. The other inertial term, involving the time derivative of the current, is a factor δ/Δ smaller, and it is neglected. The component along z of Eq. (1.8) reads

$$\delta^2 = d_e^2 + \frac{c^2}{4\pi}\eta\frac{\delta}{u}. \tag{1.12}$$

The three equations above describe the stationary reconnection process. Recalling the definitions of the Alfvén and the resistive times,

$$\tau_A = \frac{\Delta}{v_A}, \quad \tau_\eta = \frac{c^2}{4\pi}\frac{\Delta^2}{\eta} \tag{1.13}$$

Eq. (1.12) gives the aspect ratio of the reconnection layer in the Sweet-Parker model as

$$\frac{\delta}{\Delta} = \Big(\frac{d_e^2}{\Delta^2} + \frac{\tau_A}{\tau_\eta}\Big)^{1/2}. \tag{1.14}$$

Using the relation $\delta/\Delta = \tau_A u/\Delta$, the reconnection time for the Sweet-Parker model $\tau_{SP} \equiv \Delta/u$ is given by

$$\frac{\tau_{SP}}{\tau_A} \sim \left(\frac{\tau_A}{\tau_\eta} + \frac{d_e^2}{\Delta^2}\right)^{-1/2}. \tag{1.15}$$

Using Eq. (1.15) we can address quantitatively the relative importance of electron inertia and resistivity in the reconnection process. For $d_e = 0$, *i.e.* keeping only the resistive term in the left hand side of Eq. (1.12), the aspect ratio of the current sheet is $\delta/\Delta \sim (\tau_A/\tau_\eta)^{1/2}$. For typical parameters of modern fusion machines (JET), this is a rather unphysical 10^{-5}. The opposite limit of negligible resistivity yields $\delta \sim d_e$, which was much closer to observational data. The introduction of the inertial effects in the Kadomstev model it was due to Wesson [6].

Extensive numerical simulation were performed in order to check this model, see for instance [9]. The application of the Sweet-Parker model has been very abundant. The explanation of complex, nonlinear phenomena observed in experiments often relies on the conceptual mainframe of the Sweet-Parker model. The Kadomstev explanation of sawtooth oscillations in tokamaks [10], for instance, is basically the Sweet-Parker model applied to a cylindrical model of toroidal geometry and limited to resistive effects only.

The Sweet-Parker model does not describe how a stationary state is reached, nor does it describe which is the dynamics inside the reconnection layer. To answer these questions a non-stationary model is necessary.

1.3 Reduction to slab geometry

The dynamics related to reconnection is governed by the MHD equations. Solutions of the ideal MHD equations allow for discontinuities across neutral surfaces. In the region around neutral surfaces small scale effects can be important which release the constrains of flux conservation and allow for reconnection. The width of such a reconnection layer is in general very small compared with the scale of the system. For example, in the case of stationary reconnection, the Sweet-Parker model gives a width of the order of the inertia skin depth.

In this thesis magnetic reconnection in a current carrying sheared slab with a single neutral line is studied. This configuration is simpler than many physical systems where reconnection is important, like tokamaks. For instance, effects due to toroidicity such as magnetic curvature and particle trapping are not included. However, results obtained in a slab are of fundamental importance, and can be applied, with due care, to more complicated systems. The reason is that the width of the reconnection layer is extremely small with respect to the global scales, as the example in Section 1.2 of the Sweet-Parker model shows.

Notwithstanding the geometrical simplifications, the study presented in this thesis captures the essential properties of magnetic reconnection in layers.

It must be noted that geometrical effects can be very important, especially in the nonlinear phase of reconnection [11], in determining for instance which is the dominant physical mechanism responsible for the saturation of the magnetic reconnection instability.

1.4 Effects of temperature gradients on reconnection

Magnetic reconnection merges field lines which extend through regions of space that can be far apart and, in the presence of temperature gradients, have different temperatures. Then the topology change due to reconnection will result in a merging of field lines which induces a finite heat flow.

In general, far from the resonant layer the phase velocity of the reconnecting mode is much smaller than the thermal velocity. In this zone the temperature can be assumed to be a flux function and a fluid description of the plasma is possible. Close to the resonant layer the phase velocity exceeds the thermal velocity and the equation of state approaches the adiabatic law. Hence the physics close to the neutral surface can be properly described again by a fluid model. Between these two zones, for each value of the electron parallel velocity, a region exists in which the phase velocity of the reconnecting mode and the parallel electron velocity are comparable. Here wave-particle resonance effects have to be considered. The averaged effect of these spatially distributed resonances in the velocity phase subspace is to form a resonant layer where the mode phase velocity and the electron thermal velocity are comparable. Resonance contributions enter Eq. (1.7) in the form of a position dependent resistivity, effectively breaking the frozen-in law, see [12]. Hence, kinetic resonances can provide a collisionless reconnection mechanism, additionally to electron inertia. In this thesis we will refer to “collisionless reconnection” as the reconnection allowed by wave-particle resonance effects. As it will be shown in Chapter 7, wave-particle effects enter Ohm’s law in the form of an effective resistivity. Contrary to electron inertia, no Hamiltonian formulation is possible in this case.

1.5 This thesis

In this thesis Hamiltonian and collisionless reconnection are investigated. As defined already in previous sections, we call Hamiltonian the reconnection allowed by the inertial terms in the momentum balance equation. We reserved the broader ”collisionless reconnection” for the reconnection allowed by kinetic effects, as explained in the previous section.

The first part of this thesis is devoted to fluid theory. A model for Hamiltonian reconnection is derived and its properties are discussed in Chapter 2. The model is applied to two different physical slab configurations, namely a forced and an unstable one. In the forced case the plasma is embedded by flux conserving walls, with a neutral line parallel to them, and the reconnecting mode is excited by a displacement of the walls that is externally imposed. In the unstable case, an exponentially growing double periodic linear mode exists.

A review of the linear theory is presented in Chapter 3, focused in particular on forced reconnection.

Chapter 4 reports numerical solutions for the Hamiltonian reconnection in a slab for both the forced and unstable cases. In this chapter the focus is on the pronounced nonlinear effects that arise during the long-term evolution of the reconnection process.

The Hamiltonian reconnection process is first described in the cold electron limit for the forced case. The influence of finite electron temperature is then shown, and different forcing configurations are applied. The comparison between the unstable and forced cases is discussed in details. In particular the reconnection process is described [15] in terms of conserved quantities related to the Hamiltonian nature of the system of equations. The dynamical evolution in forced and unstable cases are both included in this interpretation scheme.

A novel feature that emerged only in the past few years from high resolution numerical simulations is the formation in the nonlinear stage of the reconnection process of structures in the current density and the vorticity with scale lengths well below the linear reconnection layer width. These structures are characterized and analyzed in details in both configurations. Their occurrence is explained by the conservation properties of the system.

In the second part of this thesis a kinetic description of collisionless reconnection is exploited using a model which is an extension to non-isothermal plasmas of the fluid model discussed in the first part.

The kinetic model is derived and discussed in Chapter 5. In the presence of a strong and almost constant magnetic field, the particle dynamics in the directions parallel and perpendicular to the magnetic field decouple. The kinetic equation is then written in advective form in a three dimensional phase space.

The process of time-independent reconnection of flux tubes with different temperatures is studied in Chapter 6. The effect of a temperature difference in the inflowing plasma streams in the specific case of a stationarily reconnecting solution is treated. Wave-particle resonances are absent in this time-independent problem.

In Chapter 7 the stability of a finite size magnetic island chain is studied. In contrast with resistive effects, in the reconnection due to Landau damping the mechanism for reconnection takes place away from the X point. In fact, the wave-particle resonance takes place where the phase velocity of the wave is comparable with the electron thermal velocity. If the resonance location is far from the equilibrium island chain then, due to the narrowness of the resonant layer, wave-particle and finite size island effects dominate the mode in separate locations in space. In this case the resonance effects are expected to be homologous to those treated in [12] within the thin island approximation. In this thesis we are interested in the opposite case of a resonant layer that is very close to the separatrix. In this case the presence of the island is expected to modify the resonance effects with respect to the thin island limit.

Finally, in Chapter 8 a summary of the issues covered by this thesis, results, and future research developments is presented.

Part One: Fluid Theory

2. The drift-Alfvén two fluid model

In this chapter a two-fluid model is adopted that includes collisional effects. The 2-D reduced equations for a strongly magnetized plasma are derived from Braginskii's two-fluid model. The gyroviscous cancellation is recovered and expressions for ion viscosity and resistivity are obtained. Neglecting dissipative terms, a formulation in non-canonical Hamiltonian form is possible.

2.1 The two fluid model

We derive the set of reduced equations as in [14], but in addition we take into account dissipative terms. The starting point is the Braginskii two-fluid model [1],

$$\partial_t n + \nabla \cdot (n\mathbf{v}) = 0, \tag{2.1}$$

$$\begin{aligned} nm\left(\partial_t + \mathbf{v}\cdot\nabla\right)\mathbf{v} &= -\nabla(nT) + \\ &+en\sigma(\mathbf{E} + \frac{1}{c}\mathbf{v}\times\mathbf{B}) + (-\sigma\mathbf{R} - \nabla\cdot\mathbf{\Pi}), \end{aligned} \tag{2.2}$$

where $\sigma = +1$ for protons and $\sigma = -1$ for electrons. The other symbols have the usual meaning. Equations (2.1, 2.3) must be written for both electrons and ions, and completed by Maxwell's equations and, in general, suitable equations for temperatures. Subscripts e, i for electron and ions respectively will be added whenever confusion might arise. The magnetic and electric fields are described by the magnetic flux ψ and electric potential ϕ,

$$\mathbf{B} = B_0(\mathbf{e}_z + \mathbf{e}_z \times \nabla\psi), \qquad \mathbf{E} = \frac{B_0}{c}(-\nabla\phi + \partial_t\psi\mathbf{e}_z), \tag{2.3}$$

where $\mathbf{e}_z$ is the unit vector in the z direction. The component of the magnetic field in the z direction is constant and much larger than the transverse component, $B_0\mathbf{e}_z \times \nabla\psi$. This representation of the magnetic field does not allow for the description of compressional Alfvén waves, which are hence not included in the model.

The velocity is written as $\mathbf{v} = v_z\mathbf{e}_z + \mathbf{v}_\perp$. For later use it is opportune to derive the expression for the perpendicular component of the fluid velocity by taking the cross product of Eq. (2.3) with $\mathbf{e}_z$,

$$\begin{aligned} \mathbf{v}_\perp = \mathbf{e}_z \times \Bigg\{ &\nabla\phi + \frac{1}{\sigma}\frac{cT}{eB_0}\nabla\ln nT + v_z\nabla\psi + \\ &\frac{1}{\sigma}\frac{mc}{eB_0}\left(\partial_t + \mathbf{v}\cdot\nabla\right)\mathbf{v} - \frac{c}{\sigma enB_0}(\sigma\mathbf{R} - \nabla\cdot\mathbf{\Pi})\Bigg\} \end{aligned} \tag{2.4}$$

The term $v_z \nabla \psi$ arises from the small misalignment between the total magnetic field and the direction of $\mathbf{e}_z$. In the following, the subscript $\|$ denotes parallel to the magnetic field while z and $\perp$ refer respectively to a component parallel and perpendicular to $\mathbf{e}_z$.

2.1.1 Electron fluid

Consider a plasma that is strongly magnetized, that is the typical frequency ω associated with plasma motion is much smaller than the electron gyrofrequency $\Omega_e \equiv eB_0/m_e c$. The strong and almost constant magnetic field imposes that $\nabla_\| \ll \nabla_\perp$. The inductive term $\partial_t \psi$ in Eq. (2.3) is assumed to be of the same order of $\nabla_\| \phi$. Consistently, the $E \times B$ contribution to Eq. (2.4) is to leading order. The polarization drift is ω/Ω_e times smaller than the $E \times B$ velocity, and can be neglected. Because of the high temperature collisions are infrequent and dissipative terms are negligible. Thus, in Eq. (2.4), only the first three terms have to be retained.

The expression for the perpendicular electron fluid velocity is explicitly given by

$$\mathbf{v}_\perp = \mathbf{e}_z \times \nabla \phi - \frac{c}{enB_0} \mathbf{e}_z \times \nabla (nT) + v_z \mathbf{e}_z \times \nabla \psi. \tag{2.5}$$

In order to solve the equations for the parallel motion we consider the continuity equation and the component of Eq.(2.3) parallel to $\mathbf{e}_z$. Using the expressions

$$\begin{aligned} \nabla \cdot \mathbf{v}_\perp &= -\frac{c}{enB_0}[n, T] + [\psi, v_z] \\ \mathbf{v}_\perp \cdot \nabla A &= [\phi, A] - \frac{c}{enB_0}[nT, A] + v_z [\psi, A] \end{aligned} \tag{2.6}$$

and $[A, B] \equiv \mathbf{e}_z \cdot \nabla A \times \nabla B$, for any arbitrary functions A and B, we obtain

$$\partial_t \ln n + [\phi, \ln n] = -\frac{1}{n} \nabla_\| (n v_z), \tag{2.7}$$

$$\begin{aligned} \partial_t \left(\psi + \frac{v_z}{\Omega_e} \right) + \left[\phi, \psi + \frac{v_z}{\Omega_e} \right] - \frac{cT}{eB_0} \left[\ln(nT), \frac{v_z}{\Omega_e} \right] &= \\ \partial_z \phi - \frac{c}{eB_0} \left\{ T \nabla_\| \ln n + \nabla_\| \Big(\frac{1}{2} m_e v_z^2 + T \Big) \right\} &+ \\ \frac{c}{enB_0} \left(R_z - (\nabla \mathbf{\Pi})_z \right), & \end{aligned} \tag{2.8}$$

$$\nabla_\| T = 0, \tag{2.9}$$

where $\nabla_\| A = \partial_z A + [\psi, A]$. Terms containing v_z/Ω_e are electron inertial terms. The fluid velocity is assumed to be smaller than the thermal velocity. It follows that in Eq. (2.8) the quadratic term in v_z is negligible with respect to T. Note that when these two terms are comparable then wave-particle effects must be included, as explained in Chapter 1. The extension of the model required in order to include wave-particle effects is presented in Chapter 5.

Equation (2.9) models the isothermal behavior of the electrons along the field lines. In Appendix A this equation is derived as a collisionless limit from the energy balance equation for modes with frequency ω and parallel wave vector $k_\parallel$ such that $\omega\nu_c/(k_\parallel v_{th})^2 \ll 1$, where ν_c is the electron-ion collision frequency.

In the next chapters we will study only the two-dimensional problem. A derivation of the three fields electron fluid equations in the three-dimensional case is given in Appendix A. Here we discard any z–dependence. Then the parallel gradient simplifies as $\nabla_\parallel A = [\psi, A]$. Excluding ion sound waves, the current is carried by electrons only, and Ampére's law can be written as $J \equiv -4\pi env_z/cB_0 = \nabla_\perp^2\psi$. In this case, the relation $v_z/\Omega_e = -d_e^2 J$ holds.

As far as the dissipative terms are concerned, the classical collisional theory in [1] is adopted. The ratio between the collision frequency ν_c and the electron gyrofrequency is small. In the strong magnetic field limit $(\omega/\Omega_e \ll 1)$ the components of the resistivity and the divergence of the stress tensor in the z direction to the relevant order are

$$R_z = \frac{neJ}{\sigma_\parallel}, \qquad \nabla\cdot\mathbf{\Pi}|_z = nT\left[\ln nT, \frac{v_z}{\Omega_e}\right],$$

where $\sigma_\parallel = 2.0\ ne^2/(\nu_c m)$. These are the only transport coefficients that are considered here. In Appendix A the complete set of classical transport coefficients in the full three dimensional case are reported. There also the collisonless limit of the electron fluid equations is discussed.

The dissipative terms give two contributions. The first one, R_z, introduces the resistivity $\eta = m_e c\nu_c/2.0e^2B_0 n$. The second one comes from the divergence of the stress tensor $\mathbf{\Pi}$ and exactly cancels the term $\mathbf{v}_D\cdot\nabla(v_z/\Omega_e)$ arising from the nonlinear term in Eq.(2.3) (this is the *gyroviscous cancellation*). Hence we obtain

$$\partial_t \ln n + [\phi, \ln n] - \frac{cB_0}{4\pi en}[\psi, J] = 0, \tag{2.10}$$

$$\partial_t\left(\psi - d_e^2 J\right) + \left[\phi, \psi - d_e^2 J\right] + \frac{cT}{eB_0}[\psi, \ln n] = \eta J. \tag{2.11}$$

Equations (2.10, 2.11) are fully nonlinear. They retain electron parallel compressibility and inertia effects, and resistivity.

2.1.2 Ion fluid

Ion inertia is much larger that the electron one, so that the ion parallel velocity is small. Hence, the ion equation is derived by substituting the perpendicular velocity in the continuity equation, Eq. (2.1). The ion equation is derived for perturbations whose phase velocity, $\omega/k_\parallel$, is much larger than the ion thermal velocity (cold ion limit). In this limit the diamagnetic drift in Eq. (2.4) is negligible. To leading order the ion perpendicular velocity is given by the $E \times B$ velocity, $\mathbf{v}_E \equiv \mathbf{e}_z \times \nabla\phi$. Because it is $\nabla_\perp \cdot \mathbf{v}_E = 0$, then also the next order term is necessary. The next order term in the perpendicular velocity is given by the polarization drift and the stress tensor contributions, and it is important only in the term $\nabla_\perp \cdot \mathbf{v}_\perp$ of the continuity equation. Hence the ion perpendicular velocity is

$$\mathbf{v}_\perp = \mathbf{v}_E - \frac{1}{\Omega_i}(\partial_t + \mathbf{e}_z \times \nabla\phi \cdot \nabla)\nabla_\perp\phi + \mathbf{e}_z \times \Big(\frac{c}{enB_0}\nabla \cdot \mathbf{\Pi}\Big). \tag{2.12}$$

Substituting in the continuity equation we have

$$\begin{aligned} (\partial_t + \mathbf{e}_z \times \nabla\phi \cdot \nabla)\,\Gamma + \eta_1 \frac{c}{en_iB_0}\nabla_\perp^2(\nabla_\perp^2\phi) = 0, \\ \Gamma \equiv \ln n_i - \frac{1}{\Omega_i}\nabla_\perp^2\phi \end{aligned} \tag{2.13}$$

where $\eta_1 = \frac{3}{10} n_i T_i \nu_{c_i}/\Omega_i^2$, and ν_{c_i} is the ion-ion collision frequency. The η_1 viscous term comes from the divergence of the last term on Eq. (2.12). It is the dominant contribution in the divergence of the stress tensor. A lower order term, proportional to η_0 in Braginskii's notation, vanishes under the action of the divergence, see Appendix A.

Equation (2.13) was derived in Ref. [14] in the small ion gyroradius limit. It describes the ions in the cold ion limit, so when the ion temperature vanishes but gyroradius effects as $\rho_s^2 \equiv T_e\rho_i^2/T_i = c^2 T m_i/(eB_0)^2$ are finite; ρ_i and ρ_s are the ion gyroradius and ion sound gyroradius[1], respectively.

2.2 The drift-Alfvén two fluid model

We now actually assume the electron temperature to be constant through the whole plasma. The quasi-neutrality condition, $n_e = n_i$, relates the parallel electron compressibility to the ion dynamics.

Subtracting Eq. (2.10) from Eq. (2.13) we obtain

$$\partial_t \nabla_\perp^2\phi + \left[\phi, \nabla_\perp^2\phi\right] - v_A^2\,[\psi, J] = \nu_i \nabla_\perp^2(\nabla_\perp^2\phi), \tag{2.14}$$

where $\nu_i = \eta_1 c/enB_0$ is the ion viscosity, and $v_A \equiv B_0(4\pi n m_i)^{-1/2}$ is the Alfvèn velocity.

---

[1] Note the definition of v_{th} used here differs for a factor $\sqrt{2}$ from the one in Chapter 7

The above equation, together with Eq. (2.11), (2.13), and the definition of J, constitutes a closed system of equations [13]. We further simplify the system by eliminating drift waves from it. This is done by neglecting ion viscosity and insuring the argument of the time derivative in Eq. (2.13) vanishes at $t = 0$, so that $\ln n_i \simeq \nabla_\perp^2 \phi / \Omega_i$ is a solution at all t. Using this solution in the electron momentum balance equation, Eq. (2.11), we have

$$\partial_t \left(\psi - d_e^2 J \right) + \left[\phi, \psi - d_e^2 J \right] - \rho_s^2 \left[\nabla_\perp^2 \phi, \psi \right] = \eta J. \tag{2.15}$$

Introducing the vorticity $\omega = \nabla_\perp^2 \phi$, the final set of equations is

$$\partial_t \omega + [\phi, \omega] - v_A^2 [\psi, J] = \nu_i \nabla_\perp^2 \omega, \tag{2.16}$$

$$\partial_t \left(\psi - d_e^2 J \right) + \left[\phi, \psi - d_e^2 J \right] - \rho_s^2 [\omega, \psi] = \eta J, \tag{2.17}$$

$$\omega = \nabla_\perp^2 \phi, \qquad J = \nabla_\perp^2 \psi. \tag{2.18}$$

The frequency range in which these equations are applicable is limited from above on one hand by the ordering related to the ion dynamics, *i.e.* frequencies have to be below the ion gyrofrequency. On the other hand frequencies above the magneto sonic frequency would excite longitudinal perturbations of the magnetic field, which we have discarded by taking B_0 constant. The lower frequency limit is set by the cold ion hypothesis: thermal ion modes are excluded, so frequency has to be higher than the ion sound frequency. The spatial range spans from the MHD range down to the electron inertia skin depth.

Equation (2.16) is the vorticity equation. It is basically a continuity equation in an $E \times B$ dominated flow. It relates the density variation in the perpendicular plane to the parallel gradient of the current.

The parallel component of the momentum balance equation, Eq. (2.17), is an equation for the magnetic flux ψ and can be casted as

$$\partial_t \psi + \left[\phi - \rho_s^2 \omega, \psi \right] = d_e^2 (\partial_t J + [\phi, J]) + \eta J. \tag{2.19}$$

In the limit $d_e, \eta \to 0$ Eq. (2.19) expresses a frozen-in law for the magnetic flux, *i.e.* the magnetic field lines are passively advected by the stream function $\phi - \rho_s^2 \omega$ and no magnetic reconnection can possibly take place. In order to change the magnetic field topology two mechanism are available, namely resistivity and electron inertia.

In the competition between the resistive and the inertial terms situations can take place in which the mechanism for reconnection is collisionless rather than collisional. The resistivity coefficient η drops sharply with temperature as $T^{-3/2}$, while the electron inertia skin depth d_e does not depend on the temperature and can be more important than the resistive scale length in high temperature plasmas. Note also that while the resistive term is proportional to the magnitude of the current itself, the inertial one involves the convective derivative of the current, thus the collisionless reconnection allowed by d_e cannot simply be viewed as an extension of the resistive physics. A discussion of the differences between the two reconnection mechanism can be found in Section 3.1.2 and 4.2.1.

2.3 Hamiltonian structure

Omitting the dissipative terms ($\eta = \nu_i = 0$) the system of equation can be casted in Lagrangian form [16]. To show that, multiply Eq. (2.16) by $\pm\rho_s d_e/v_A$, sum to Eq. (2.17), and use $\rho_s/d_e = v_{th}/v_A$ to obtain

$$\partial_t G_\pm + [\Phi_\pm, G_\pm] = 0, \tag{2.20}$$

where

$$G_\pm \equiv \psi - d_e^2 J \pm \frac{\rho_s d_e}{v_A}\omega, \qquad \Phi_\pm \equiv \phi \pm v_{th}\psi, \tag{2.21}$$

which shows that the two generalized fluxes $G_\pm$ are frozen in the flow fields generated by the respective stream functions $\Phi_\pm$.

The Lagrangian form Eq. (2.20) admits two infinite sets of Casimirs[2]

$$C_\pm = \int d^2x \; h_\pm(G_\pm) = \text{const.} \tag{2.22}$$

where $h_\pm(G_\pm)$ are arbitrary functions of $G_\pm$.

Multiplying Eqs. (2.16, 2.17) by $\phi - \rho_s^2\omega$ and J, respectively, and integrating in space assuming vanishing boundary contributions, we find the energy integral

$$W = \frac{1}{2}\int d^2x \left\{ |\nabla\psi|^2 + |\nabla\phi|^2 + d_e^2 J^2 + \rho_s^2\omega^2 \right\}, \tag{2.23}$$

which contains the magnetic energy, the ion kinetic energy, the parallel electron kinetic energy, and the electron internal energy. In terms of the generalized fluxes $G_\pm$, the energy integral W can be expressed as

$$W = \frac{1}{4d_e^2}\int d^2x \Big\{ G_+(G_+ - \frac{\Phi_+}{v_{th}}) + G_-(G_- + \frac{\Phi_-}{v_{th}}) \Big\} \tag{2.24}$$

We seek now the Hamiltonian of the system. Terms quadratic in $G_\pm$ in Eq. (2.24) are Casimirs, thus conserved, and they can be subtracted. The generalized fluxes can be redefined as $G_\pm \longrightarrow \pm 2d_e^2 v_{th} G_\pm$ without affecting Eq. (2.20). Then we can introduce the functional

---

[2] Casimirs are constants of motion in the sense that they commute with all functionals f, *i.e.* with reference to Eq. (2.26) it is $\{f, C_\pm\} = 0$

$$H = -\frac{1}{2}\sum_\alpha \int d^2x\; G_\alpha \Phi_\alpha \tag{2.25}$$

with $\alpha = +,\ -$. Defining the non canonical Poisson bracket [17]

$$\{f, g\} = \sum_\alpha \int d^2x\; G_\alpha \Big[\frac{\delta f}{\delta G_\alpha}, \frac{\delta g}{\delta G_\alpha}\Big] \tag{2.26}$$

where δ indicates the functional derivative, then Eq. (2.20) can be written as

$$\frac{\partial G_\pm}{\partial t} = \{G_\pm, H\} \tag{2.27}$$

and H assumes the meaning of Hamiltonian of the system.

Equation (2.20) expresses a frozen-in law for the generalized fluxes $G_\pm$, which are passively advected by the corresponding velocity fields, $\mathbf{v}_\pm = \mathbf{e}_z \times \nabla\Phi_\pm$. Equation (2.20) or Eq. (2.27) are equivalent to the system of equations Eqs. (2.16, 2.17).

In the cold electron limit, $\rho_s = 0$, we have $G_+ = G_- \equiv F = \psi - d_e^2 J$ and $\Phi_+ = \Phi_- = \phi$. Thus a single generalized flux F is conserved by the flow. In this case the stream function is the electric potential itself. The limiting case of negligible inertia yields the reduced magnetohydrodynamic result. For both the cold electron and the reduced magnetohydrodynamic limits the second equation is given by the evolution equation for $(G_+ - G_-)v_A/2\rho_s d_e = \omega$ which is none but the continuity equation Eq. (2.16).

The form of the Casimirs in the various limits are discussed in [13]. Point vortex solutions to the model reported here have been studied, see [16], [18], [19] and reference therein.

The generalized fluxes $G_\pm$ contain the magnetic flux ψ. Equation (2.20) must conserve the generalized fluxes, but nothing forbids in principle a change in the topology of the magnetic flux. Magnetic reconnection becomes a process "internal" to the dynamics of $G_\pm$. In this sense, an Hamiltonian reconnection process is one in which the topology of the magnetic flux ψ is changed while the one of the generalized fluxes $G_\pm$ is conserved. In general, the reconnection of the magnetic flux is accompanied by a suitable modification of current density and vorticity in order to fulfill the Hamiltonian constrains. Due to the smallness of d_e and ρ_s, modifications in current density and vorticity are larger than those in the magnetic flux.

Indeed, the spatial structures which are formed during the reconnection process have been recognized [15] to be related with the conservative dynamics of the fluxes $G^{\pm}$, and are discussed in Chapter 4.

The nonlinear evolution of the Hamiltonian system tends to form smaller and smaller scales in the generalized fluxes as a result of their inviscid advection. In the context of Hamiltonian reconnection, small scales are scales which are small with respect to the scale lengths in the system, d_e and ρ_s. These small scales are expected to be found in the terms with higher spatial derivatives in $G_{\pm}$, *i.e.* in current density and vorticity.

When smaller and smaller scales are formed, than dissipative terms become important. In particular resistivity and ion viscosity, which affect small scale terms, are expected to play a role. The inclusion of dissipation spoils the Hamiltonian structure of the equation, leading to reconnection of the generalized fluxes $G_{\pm}$ on the relative dissipative scale length.

The small scale formation process and its consequences on the physical quantities are analyzed in Chapter 4.

3. Linear theory of the drift-Alfvén model

In this chapter the linear analysis of the two fluid model derived in Chapter 2 is presented. In the first part the system of equations is linearized and solved in a case in which reconnection is due to a displacement of flux conserving wall embedding the plasma slab. Secondly, the case of reconnection due to unstable perturbations is reported. Finally, non stationary solutions are found in some limits.

The system of equations derived in the previous chapter is

$$\partial_t \omega + [\phi, \omega] - v_A^2 [\psi, J] = 0, \tag{3.1}$$

$$\partial_t \left(\psi - d_e^2 J\right) + \left[\phi, \psi - d_e^2 J\right] - \rho_s^2 [\omega, \psi] = \eta J, \tag{3.2}$$

$$\omega = \Delta\phi, \qquad J = \Delta\psi, \tag{3.3}$$

where $\Delta \equiv \nabla_\perp^2$, and ion viscosity has been discarded.

3.1 Taylor's problem

As discussed in Chapter 1, the fundamental properties of the Hamiltonian reconnection can be studied in a plasma slab embedded between flux conserving walls. We are interested here to present the linear analysis for single mode perturbations. Because the slab is periodic only in one direction it is then better to maintain the linearized equations in real form, taking advantage from the symmetry properties that Eqs. (3.1, 3.2), together with suitable boundary and initial conditions, have. In particular, the electrostatic potential $\phi(x, y)$ and the magnetic flux $\psi(x, y)$ are assumed to be odd and even functions of both x and y, respectively. We then consider a two dimensional equilibrium in $(-L_x, L_x) \times (-L_y, L_y)$ periodic in y, with no electrostatic potential $\phi_0 = \omega_0 = 0$, and a static magnetic flux that is quadratic in x, $\psi_0 = x^2/2L_s$. The resonant surface is at $x = 0$, and the walls are located at $x_{wall} = \pm L_x$. This equilibrium is perturbed by a displacement of the wall as

$$x_{wall} = \pm(L_x - \delta(t)\cos k_y y), \qquad k_y = \pi m / L_y \tag{3.4}$$

which excites Alfvén waves inside the plasma. The wall perturbation wave number is unity, $m = 1$, unless differently stated.

The linear response is governed by the equations

$$\partial_t \left(\partial_x^2 - k_y^2\right) \tilde{\phi} = -v_A^2 k_\parallel \left(\partial_x^2 - k_y^2\right) \tilde{\psi} \tag{3.5}$$

$$\partial_t \left(\tilde{\psi} - d_e^2 \left(\partial_x^2 - k_y^2\right) \tilde{\psi}\right) = k_\parallel \left(\tilde{\phi} - \rho_s^2 \left(\partial_x^2 - k_y^2\right) \tilde{\phi}\right), \tag{3.6}$$

where $k_\| = k_y \partial_x \psi_0 = k_y x/L_s$ is the space dependent wave vector.
The function $\delta(t)$ sets the time scale of the wall displacement τ_{wall}. In particular, $\delta(t)$ vanishes at $t = 0$, and it is of order one for times comparable or larger than τ_{wall}. The time scale of the wall displacement is assumed to be shorter than any reconnection time scale, but much larger than the Alfvén time, so that the plasma can be consider to be in magneto-static equilibria everywhere except in a thin layer around the resonant surface.
As it is shown below, the perturbation generates a magnetic island at the resonant surface position with time scale related to the relevant reconnection mechanism for the given plasma parameters. The analytical method employed to find the reconnection time scale is an asymptotic matching between the ideal magnetohydrodynamic region and the reconnection layer, where electron inertia or resistivity are important.
The model configuration described above is known in the literature as Taylor's problem, and was analytically investigated by Hahm and Kulsrud [20] in relation with resistive reconnection processes. The numerical analysis of nonlinear regimes was done in Ref. [21]. An extension to force-free equilibria and asymmetric forcing relevant in astrophysical studies was presented in [22], [23].
Here the extension of the linear treatment of Ref. [20] to the Hamiltonian reconnection is presented, while the results of the corresponding numerical simulations of nonlinear regimes are included in Chapter 4.

3.1.1 The external solution

Outside the reconnection layer the plasma is in quasi-static equilibrium. Moreover, here the small length scales ρ_s and d_e are negligible, so the linear response reduces to

$$k_\|(\partial_x^2 \tilde{\psi} - k_y^2 \tilde{\psi}) = 0, \qquad \tilde{\phi} = 0, \tag{3.7}$$

which is equivalent [20] to the first order approximation in the wall perturbation parameter δ of the ideal MHD force balance equation, $\mathbf{J} \times \mathbf{B} = \nabla p$. Equation (3.7) expresses the vanishing of the parallel gradient of the current, and it allows for discontinuous solutions at $k_\| \equiv k_y x/L_s = 0$. The solution of the above equation is

$$\tilde{\psi}(x) = A \cosh k_y x + B \sinh k_y x, \qquad x > 0. \tag{3.8}$$

The magnetic flux ψ is an even function of x, so ψ is the mirror image of Eq. (3.8) for negative x; A and B are integration constants to be fixed by the boundary conditions at $x = 0$ and $x = x_{wall}$.
Equation (3.8) is the combination of two types of solutions. The first one, proportional to $\sinh k_y x$, has the same topology as the equilibrium, ψ_0, but with a jump

in the y component of the magnetic field corresponding to a surface current. The second type of solution, proportional to $\cosh k_y x$, has no surface current but the value of the magnetic flux on the neutral line is finite, indicating a change in the original topology. Indeed, this second solution has a magnetic island of—half—width $(2AL_s)^{1/2}$, see Fig. 3.1.

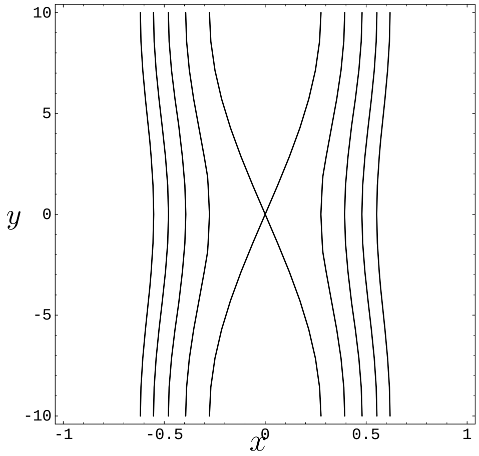

Figure 3.1: The reconnected part of the solution $\tilde{\psi}(x)$, Eq. (3.9).

The original motivation of the work of Hahm and Kulsrud was to determine which of the two possible equilibria will eventually dominate. To answer this question the dynamics inside the reconnection layer was solved for the resistive case and the equilibrium with a changed topology was found to prevail. In the following the same linear theory is extended to Hamiltonian reconnection in its relevant regimes. The inclusion of the effects of electron inertia affects the time scale of the process but not the final outcome of the linear treatment. We will present here the linear analysis for both the resistive and collisionless cases on the same footing. For additional details about the resistive case we refer the reader to the original article [20].

After imposing that the wall is a flux-conserving boundary, $\psi_0(x = L_x) = \psi(x = x_{wall})$, the solution to Eq. (3.7) can be written

$$\tilde{\psi}(x) = A\left(\cosh k_y x - \frac{\sinh k_y x}{\tanh k_y L_x}\right) + \delta \frac{L_x}{L_s}\frac{\sinh k_y x}{\sinh k_y L_x}. \tag{3.9}$$

with $A = \tilde{\psi}(x = 0)$ to be fixed by the solution inside the reconnection layer. In Eq. (3.9) only terms up to the first order in δ/L_x are retained. The reconnected flux $\tilde{\psi}(0)$ can be expressed in terms of the jump of the logarithmic derivative across the reconnection layer, Δ', defined for the external region as

$$\Delta' \equiv \lim_{x\downarrow 0} \frac{1}{\tilde{\psi}} \frac{d\tilde{\psi}}{dx} - \lim_{x\uparrow 0} \frac{1}{\tilde{\psi}} \frac{d\tilde{\psi}}{dx} = 2 \lim_{x\to 0} \frac{1}{\tilde{\psi}} \frac{d\tilde{\psi}}{dx}. \tag{3.10}$$

where the parity of $\tilde{\psi}$ was used. Using the derivative of Eq. (3.9) in Eq. (3.10) and inverting for $\tilde{\psi}(x=0)$ we find

$$\tilde{\psi}(x=0) = \frac{L_x}{L_s} \frac{\delta(t)}{\cosh k_y L_x} \frac{1}{1 + (\Delta'/2k_y) \tanh k_y L_x}. \tag{3.11}$$

The solution for the reconnection layer is now needed only to determine the value of Δ' as a function of time. This procedure is equivalent to the matching technique employed in [5], with the difference that there the solution inside the reconnection layer is needed not to choose between possible solutions in the magnetohydrodynamic region but to fix the dispersion relation.

3.1.2 Solution in the reconnection layer

Inside the reconnection layer $\partial_x^2 \gg k_y^2$ holds so the linearized equations are

$$\partial_t \partial_x^2 \tilde{\phi} = -v_A^2 \frac{k_y x}{L_s} \partial_x^2 \tilde{\psi} \tag{3.12}$$

$$\partial_t \left(\tilde{\psi} - d_e^2 \partial_x^2 \tilde{\psi} \right) = \frac{k_y x}{L_s} \left(\tilde{\phi} - \rho_s^2 \partial_x^2 \tilde{\phi} \right) + \eta \partial_x^2 \tilde{\psi}. \tag{3.13}$$

In order to analyze also the time evolution, the Laplace transform of Eqs. (3.12, 3.13) is employed

$$\tilde{f}(x,s) = \int_0^\infty dt \quad e^{-st} \tilde{f}(x,t),$$

and the system of equations for the reconnection layer reads

$$s\tilde{\phi}'' = -v_A^2 \frac{k_y x}{L_s} \tilde{\psi}'' \tag{3.14}$$

$$\tilde{\psi} = \left(d_e^2 + \frac{\eta}{s} \right) \tilde{\psi}'' + \frac{k_y x}{L_s s} \left(\tilde{\phi} - \rho_s^2 \tilde{\phi}'' \right), \tag{3.15}$$

where the prime indicates derivative with respect to x. The solution to this system of equations will be used to compute the $\Delta'(s)$, which inside the reconnection layer is given for even $\tilde{\psi}$ by

$$\Delta' = 2 \lim_{x\to\infty} \frac{\tilde{\psi}'}{\tilde{\psi}} = \lim_{x\to\infty} \frac{2}{\tilde{\psi}(x)} \int_0^x dx \; \tilde{\psi}''(x). \tag{3.16}$$

This expression shows that Δ' is a measure of the current inside the reconnection layer. The $\Delta'(s)$ computed using the solutions to Eqs. (3.14, 3.15) is then substituted in the Laplace transform of Eq. (3.11),

$$\tilde{\psi}(x=0,s) = \frac{L_x}{L_s}\frac{\delta}{\cosh k_y L_x}\,\frac{1}{s}\frac{1}{1+(\Delta'/2k_y)\tanh k_y L_x}. \tag{3.17}$$

Apart from $\Delta'(s)$, the only time dependence in Eq. (3.17) comes from the wall displacement, $\delta(t)$, due to the fact that the plasma in the external region is in quasi-static equilibrium. The time scale of the walls displacement, τ_{wall}, is assumed to be much shorter then the reconnection time scale. Hence, the time dependence in $\delta(t)$ is approximated by a step function[1]. The Laplace transform of $\delta(t)$ is then δ/s, where δ is a constant amplitude.

Following [25], page 284, or the original article [24], we can write Eqs. (3.14–3.15) as equations for the radial electric field $E(x) \equiv \phi'$. By virtue of the identity $xf'' = [x^2(f/x)']'$, we can integrate Eq. (3.14) as

$$E = -\frac{v_A^2 k_y}{sL_s}x^2\Big(\frac{\tilde{\psi}}{x}\Big)' + C \tag{3.18}$$

where C is an integration constant. Then, dividing by x and differentiating once, Eq. (3.15) reads

$$E\Big(1+\frac{v_A^2k_y^2}{s^2L_s^2}x^2\Big) - \frac{v_A^2k_y^2}{s^2L_s^2}x^2(\rho_s^2E')' - \frac{x^2}{s}\Big[(\eta+sd_e^2)\frac{E'}{x^2}\Big]' = C \tag{3.19}$$

or, assuming no x dependence in η,

$$E\Big(1+\frac{x^2}{x_A^2}\Big) - x_R^2x^2\frac{d}{dx}\Big[\frac{dE}{dx}\Big(\frac{1}{x^2}+\frac{\rho_s^2}{x_R^2x_A^2}\Big)\Big] = C, \tag{3.20}$$

where we have introduced the shear Alfvén length scale, x_A, and the reconnection length scale, x_R,

$$x_A \equiv sL_s/k_yv_A, \qquad x_R^2 \equiv d_e^2 + \eta/s. \tag{3.21}$$

The constant C can be fixed by the asymptotic matching between solutions inside and outside the reconnection layer. Inside the reconnection layer, using Eq. (3.14) in the definition of Δ', Eq. (3.16), we have

$$\lim_{x\to\infty}\tilde{\psi} = -\frac{2}{\Delta'}\frac{x_A}{v_A}\int_0^\infty dx\,\frac{E'}{x}. \tag{3.22}$$

---

[1] The effect of a exponential time dependence of $\delta(t)$ was studied in [20] and found to be just a delay of the dynamics of the time independent case

Now, in the limit of large x the first and third terms on the left hand side of Eq. (3.20) are negligible. The the second derivatives in the fourth term is negligible for algebraically decaying solution, consistent with the fact that at large x the equation has to reproduce the MHD limit, *i.e.* $\rho_s, x_R \rightarrow 0$. The remaining terms give

$$E(x \rightarrow \infty) \simeq C\frac{x_A^2}{x^2} \quad \Longrightarrow \quad \tilde{\phi} \simeq \tilde{\phi}_R - C\frac{x_A^2}{x} \tag{3.23}$$

with $\tilde{\phi}_R =$ constant. In the same limit Eq. (3.15) is

$$\tilde{\psi} \simeq \frac{k_y x}{sL_s}\tilde{\phi} = -C\frac{x_A}{v_A} + \Big(\frac{k_y}{sL_s}\tilde{\phi}_R\Big)x, \tag{3.24}$$

which gives the asymptotic limit for large x of $\tilde{\psi}$ inside the reconnection layer. On the other hand the external solution, Eq. (3.8), for $x \rightarrow 0$ is

$$\tilde{\psi} \simeq A + Bx; \tag{3.25}$$

the matching between the external solution Eq. (3.25) for $x \longrightarrow 0$ and internal solutions for $x \longrightarrow \infty$, Eq. (3.22), gives

$$A = -\frac{2}{\Delta'}\frac{x_A}{v_A}\int_0^\infty dx\,\frac{E'}{x} = -C\frac{x_A}{v_A}, \tag{3.26}$$

where also Eq. (3.24) was used. The integration constant is related to Δ' as

$$C = \frac{2}{\Delta'}\int_0^\infty dx\,\frac{E'}{x}. \tag{3.27}$$

In the same way the matching of the linear term in x gives $B = k_y\tilde{\phi}_R/sL_x$. This does not directly enters the equation for E.

Finally, an equivalent formulation of Eqs. (3.14, 3.15) is given by

$$E + \frac{v_A}{x_A}x^2\Big(\frac{\tilde{\psi}}{x}\Big)' = \frac{1}{\Delta'}\int_{-\infty}^{\infty} dx\,\frac{E'}{x} \tag{3.28}$$

$$E\Big(1 + \frac{x^2}{x_A^2}\Big) - x^2\frac{d}{dx}\Big[\frac{dE}{dx}\Big(\frac{x_R^2}{x^2} + \frac{\rho_s^2}{x_A^2}\Big)\Big] = \frac{1}{\Delta'}\int_{-\infty}^{\infty} dx\,\frac{E'}{x} \tag{3.29}$$

The system Eqs. (3.14, 3.15), or equivalently Eqs. (3.28, 3.29), contains three length scales, x_A, x_R, and ρ_s, and the parameter Δ'. The shear Alfvén scale length x_A can be eliminated by normalization. Nevertheless, with three parameters the equations are still too complicated to be solved in general, and approximations are necessary. In different limits the solution is found to have different typical length scale w, with functional dependence $w = x_A f(\rho_s/x_R, x_R/x_A, x_A\Delta')$. Solutions are known in the two regimes that can be described according to the value of $\Delta' w$:

$\Delta' w \geq 1$: large Δ' regime, in which the right hand sides of Eqs. (3.28–3.29) can be neglected.

$\Delta' w \ll 1$: small Δ' regime. It is equivalent to the so-called "constant ψ approximation", that is $\tilde{\psi}(x) \simeq \tilde{\psi}_\infty =$ const. on the left hand side of Eq. (3.15). The constant ψ approximation is recovered in Eq. (3.29) by neglecting ion inertia.

It has been shown [26] that the constant ψ approximation is inapplicable for toroidal kink-tearing instabilities with poloidal mode number $m = 1$. Moreover, as is shown below, such an approximation leads to an extremely slow mode growth rate, as it turns out to be proportional to the third power of d_e. Hence, the relevant reconnection regime was recognized to be the large Δ' regime. On the other hand, the Taylor problem as treated by Hahm and Kulsrud requires to take the inverse Laplace transform of Eq. (3.17), where the explicit $\Delta'(s)$ is needed. In the solutions for the large Δ' regime presented below, Δ' is, as a matter of fact, taken to be infinity. In this case the Laplace transform cannot be inverted. Expressions for $\Delta'(s)$ which are valid for all values of Δ' are known, see [29] and [33], but they present similar limitations when they are used to invert the Laplace transform involved in the Taylor problem. Instead of reproducing all the analytical solutions we focus on those which give more physical insight in the numerical simulations presented in Chapter 4.

As will be explained in Chapter 4, the analysis of the numerically obtained solutions requires a definition of Δ' that is valid in the nonlinear phase too, and is not asymptotic as the one of linear theory. In Chapter 4 it is shown that the definition used there, denoted by Δ'_{nl}, is a homology of the linear Δ'. In the typical numerical experiment reported there, the reconnection process starts in the large Δ'_{nl} regime. In this stage the process is driven by the electron inertia skin depth, and the ion sound gyroradius term has initially no appreciable effect on the reconnected flux. As reconnection proceeds, the value of Δ'_{nl} decreases. Eventually the saturation of the magnetic island is reached after the small Δ'_{nl} regime takes over. We then order different contribution in time, taking advantage of the correspondent different regimes for Δ'. The dynamical process inside the reconnection layer can be split in two stages:

large Δ' : this corresponds to small values of the reconnected flux and large scale mode structures.

In the large Δ' regime the relevant equations are

$$E + \frac{v_A}{x_A} x^2 \Big(\frac{\tilde{\psi}}{x}\Big)' \simeq 0 \tag{3.30}$$

$$E\Big(1 + \frac{x^2}{x_A^2}\Big) - x_R^2 x^2 \Big(\frac{E'}{x^2}\Big)' - x^2 \frac{\rho_s^2}{x_A^2} E'' \simeq 0. \tag{3.31}$$

These equations formally correspond to infinite Δ'. Because Δ' is out of the theory, the problem is reduced to an eigenvalue problem, and its solution cannot be used in Eq. (3.17).
In the initial phase the ρ_s term can be neglected because no equilibrium vorticity is present. The $\rho_s^2\omega$ term becomes important when the electric potential assumes structures of the order of ρ_s.

small Δ' : for small Δ' the constant ψ approximation is applicable. The relevant equation are Eqs. (3.14, 3.15) with $\tilde{\psi} \simeq \tilde{\psi}_\infty =$ const. on the left hand side of Eq. (3.15). The constant ψ approximation decouples the two equations. Recalling the definition of Δ' we can re-write the relevant equations as

$$\Delta' = -\frac{x_A}{v_A}\frac{1}{\tilde{\psi}_\infty}\int_{-\infty}^{\infty} dx\, \frac{\tilde{\phi}''}{x} \tag{3.32}$$

$$\Big(1 + \frac{\rho_s^2}{x_R^2}\frac{x^2}{x_A^2}\Big)\tilde{\phi}'' - \frac{1}{x_R^2}\frac{x^2}{x_A^2}\tilde{\phi} = -\frac{v_A}{x_R^2}\tilde{\psi}_\infty\frac{x}{x_A} \tag{3.33}$$

These equations can be also derived from Eqs. (3.28–3.29). Equation (3.32) comes directly from Eq. (3.28) for $\tilde{\psi} \simeq \tilde{\psi}_\infty$ and negligible ion inertia. Using Eq. (3.28) in Eq. (3.29) and the constant ψ approximation, Eq. (3.33) follows by integration.

The solutions in the two regimes mentioned above are now derived. As just explained, only in the small Δ' regime it is possible to use the $\Delta'(s)$ obtained by the solutions inside the reconnection layer into Eq. (3.17) and to invert the Laplace transform. In the opposite limit of infinite Δ' only the mode growth rate can be obtained.

Solution for the large Δ' regime

Two limits are discussed. The first one is the cold electron limit, where the ρ_s term vanishes. Then the effects of finite electron temperature are considered.

Cold electron temperature limit

In this paragraph we reproduce the analysis from the book of Hazeltine and Meiss [25] for the case $\eta = 0$, referring the reader to that book for the details concerning the resistive case. Let us consider first the case $\rho_s = 0$. By means of the substitution $E = M(z)\exp -z^2/2$, $z = \alpha x^2$, Eq. (3.31) takes the form

$$zM'' - \frac{1}{2}(2z+1)M' - bM = 0 \tag{3.34}$$

where $\alpha = (x_A x_R)^{-1}$, $b = -(1 - x_A\alpha)/4$, and the prime indicates derivative with respect to z. This is a confluent hypergeometric equation with two independent solutions

$$M(b, -\frac{1}{2}, \alpha x^2), \qquad x^3 M(\frac{3}{2} + b, \frac{5}{2}, \alpha x^2) \tag{3.35}$$

which both grow exponentially for large x unless the first argument is a negative integer, $-n$. Thus the two solutions are

$$E_+^{(n)}(x) = e^{-\frac{\alpha}{2}x^2} M(-n, -\frac{1}{2}, \alpha x^2) \tag{3.36}$$

$$E_-^{(n)}(x) = x^3 e^{-\frac{\alpha}{2}x^2} M(-n, \frac{5}{2}, \alpha x^2) \tag{3.37}$$

and the condition on b give the dispersion relation in the form

$$x_A^2 \alpha = \frac{sL_x}{k_y v_A d_e} = \begin{cases} 1 - 4n & \text{for } E_+^{(n)} \\ -5 - 4n & \text{for } E_-^{(n)} \end{cases} \tag{3.38}$$

Now, in order the mode to be unstable we have to impose $\Re\{s\} > 0$. Thus, E_+^0 is the only unstable mode, and the relevant solution for the unstable mode is

$$E_+^{(0)}(x) = e^{-x^2/2d_e^2} M(0, -\frac{1}{2}, \frac{x^2}{d_e^2}), \qquad \text{with } s = k_y v_A d_e / L_s. \tag{3.39}$$

The growth rate is linear in d_e. The radial electric field is concentrated in a layer of the order of $w \simeq d_e$, which is typical of the large Δ' regime. The mode decays exponentially for large x, so no strong coupling is present with the outside MHD region.

Similarly, for the resistive case the same mode is found [25] to be unstable but the dispersion relation reads $s^3 = (k_y/\tau_A)^2\eta$.

Finite electron temperature effect

The effect of ρ_s in the large Δ' regime has been discussed in relation with the $m = 1$ kink-tearing mode [27], [28]. The solution to Eq. (3.29) with vanishing right hand side is found using the fact that $\rho_s^2/d_e^2 = \beta m_i/m_e \gg 1$. Then a double matching technique can be applied [27], splitting the reconnection layer into two overlapping regions as

$$\frac{x_A^2}{x^2} \gg 1 \quad \Longrightarrow \frac{d}{dx}\Big[\frac{dE}{dx}\Big(\frac{1}{x^2} + \frac{\rho_s^2}{x_R^2 x_A^2}\Big)\Big] - \frac{1}{x_R^2 x^2}E = 0$$

$$\frac{x_A^2}{x^2} \ll \frac{\rho_s^2}{x_R^2} \quad \Longrightarrow \frac{d^2E}{dx^2} - \frac{x_A^2}{\rho_s^2}E\Big(1 + \frac{x^2}{x_A^2}\Big) = 0.$$

The first equation has solution in terms of hypergeometric functions, while the second one in terms of Bessel functions. The matching of the two solutions in the overlap region $(x_R/\rho_s)^2 \ll (x/x_A)^2 \ll 1$ gives the eigenvalue. The growth rate is enhanced with respect to the case $\rho_s = 0$,

$$s \simeq k_y v_A \rho_s \Big(\frac{d_e}{\rho_s}\Big)^{1/3} / L_s, \qquad \rho_s \gg d_e. \tag{3.40}$$

As in the cold electron limit, the mode is not coupled with the external MHD region.

Solution for the small Δ' regime

We can normalize the relevant equations for this case, Eqs. (3.32–3.33), by setting $v = x/(x_R x_A)^{1/2}$ and $y = -\tilde{\phi}(x_R x_A)^{1/2}/v_A\tilde{\psi}_\infty$, obtaining in this way

$$\Delta' = q(\gamma)\sqrt{\frac{x_A}{x_R^3}}, \qquad q(\gamma) \equiv \int_{-\infty}^{\infty} \frac{dv}{v}\,\frac{d^2y}{dv^2} \tag{3.41}$$

$$(1+\gamma^2 v^2)y'' - v^2 y = v. \tag{3.42}$$

Due to the presence of $\gamma^2 \equiv \rho_s^2/x_R x_A$ in Eq. (3.42), the dependence on scale lengths of Δ' can be obtain only after the solution to Eq. (3.42) is known and the integral is performed.

Equation (3.42) belongs to the class of (inhomogeneous) spheroidal wave equations, and has no solutions in closed form for arbitrary values of the parameter γ. The small Δ' regime allows in principle for an explicit computation of $\Delta'(s)$. Then it is not interesting to find here solutions using double matching techniques (as in the previous paragraph), because these will give only an eigenvalue equation for the Laplace frequency, s. Approximate solutions to Eq. (3.42) can be derived if γ is either negligible or dominant with respect to unity. Specifically, for $\rho_s^2 \ll x_R x_A$ the parameter γ tends to zero and the cold electron limit is recovered. The opposite limit of high electron temperature corresponds to $\gamma \gg 1$.

Cold electron temperature limit

Setting $\gamma \simeq 0$ Eqs. (3.42) read

$$\Delta' = q_R\sqrt{\frac{x_A}{x_R^3}} = q_R\begin{cases} (s\tau_A)^{1/2}(k_y d_e^3)^{-1/2}, & \text{for} \quad x_R = d_e \\ (s\tau_A^{2/5}\eta^{-3/5})^{5/4}k_y^{-1/2}, & \text{for} \quad x_R = (\eta/s)^{1/2} \end{cases} \tag{3.43}$$

where q_R is a number defined by

$$y'' - v^2 y = 4v \tag{3.44}$$

$$q_R = \int_{-\infty}^{\infty} \frac{dv}{v}\,\frac{d^2y}{dv^2} \tag{3.45}$$

and $\tau_A \equiv L_s/v_A$. The value q_R is readily obtained by solving the differential equation in Fourier space, according to the method developed in [29] and used in [25] page 290, to obtain $q_R = 2\pi\Gamma(3/4)/\Gamma(1/4) \simeq 2.12$. We are now able to match the two solutions and invert the Laplace transform. Substituting in Eq. (3.17), the magnetic flux in the X-point is given by

$$\tilde{\psi}(0,t) = \frac{L_x}{L_s}\frac{\delta}{\cosh k_y L_x} I_r(t) \tag{3.46}$$

with

$$I_r(t) \equiv \frac{1}{2\pi i}\int \frac{dp}{p}\,\frac{e^{pt/\tau_r}}{1+p^r} \tag{3.47}$$

where r and τ_r are determined by the solution inside the reconnection layer. In particular we have from Eq. (3.43)

$$r = 1/2, \qquad \tau_{1/2} = (\frac{1}{2}q\tanh k_y L_x)^2 \tau_A (k_y d_e)^{-3} \tag{3.48}$$

for the Hamiltonian case, and

$$r = 5/4, \qquad \tau_{5/4} = (\frac{1}{2}q\tanh k_y L_x)^{4/5} \tau_A^{2/5} (k_y^2 \eta)^{-3/5} \tag{3.49}$$

for the resistive one. The integral for the Hamiltonian case, Eq. (3.48), can be solved analytically [30] and leads to

$$I_{1/2}(t) = 1 - e^{t/\tau_{1/2}}\mathrm{Erfc}(\sqrt{t/\tau_{1/2}}). \tag{3.50}$$

In the resistive case, following [20], we can reduce $I_{5/4}(t)$ to the real form

$$\begin{aligned} I_{5/4}(t) = 1 - \frac{8}{5}e^{(t/\tau_{5/4})\cos\frac{4}{5}\pi}\cos\Big[\frac{t}{\tau_{5/4}}\sin\frac{4}{5}\pi\Big] + \\ \frac{1}{\sqrt{2}\pi}\int_0^\infty dv\,\frac{v^{1/4}e^{-vt/\tau_{5/4}}}{1-\sqrt{2}v^{5/4}+v^{5/2}} \end{aligned} \tag{3.51}$$

and evaluate it numerically. In Fig. 3.2 $I_{1/2}(t)$ and $I_{5/4}(t)$ are plotted as a function of $t/\tau_{1/2}$. Note that the time scale of $I_{5/4}(t)$ is shrunk by a factor $\tau_{1/2}/\tau_{5/4}$ with respect to that of $I_{1/2}(t)$. The growth rate in the Hamiltonian case is proportional to the third power of d_e, so much slower than in the large Δ' regime. This is a consequence of the "constant ψ" approximation. We point out that the overshooting of the saturation level in the resistive case has been interpreted by Xiaogang Wang and Bhattacharjee as a feature of the linear approximation [31], in effect removed by nonlinearities.

Finite electron temperature effect

In the opposite limit $\gamma \gg 1$ the inertial term in Eqs. (3.42) is negligible. It is again possible to write the equations in a form such that no parameters appear in the differential equation. In fact, normalizing Eqs. (3.32, 3.33) by $v = x/\rho_s$, $y = -\tilde{\phi}\rho_s/v_A x_A \tilde{\psi}_\infty$, we obtain

$$\Delta' = q_\rho \frac{x_A^2}{\rho_s^3} \tag{3.52}$$

where q_ρ is a *number* defined by

$$y'' - y = \frac{1}{v}, \tag{3.53}$$

$$q_\rho = \int_{-\infty}^{\infty} \frac{dv}{v} \, \frac{d^2y}{dv^2}. \tag{3.54}$$

In this case it is $\Delta' \propto s^2\rho_s^{-3}$. The solution to the differential equation Eq. (3.53) leads to $q_\rho = 0$. This result is not surprising, because we have discarded from the original Eq. (3.42) the inertial term and resistive terms, x_R, and no reconnection is allowed by the equation. This limit corresponds to an ideal phase of drive without reconnection.

However, an approximate result can be obtained for large γ in the following way. For values of v larger than γ^{-1} the differential equation Eq. (3.42) reduces to $y \simeq -v^{-1}$. These large values of v give a contribution to $q(\gamma)$ that is of the order of $\sim \gamma^{-3}$, thus negligible for large γ. The main contribution in $q(\gamma)$ is then for $v \ll \gamma^{-1}$. In that limit Eq. (3.42) reduces to $y'' \simeq v/(1+\gamma^2 v^2)$ and $q(\gamma) \simeq \pi/\gamma$. The corresponding Δ' is given by

$$\Delta' = \pi \frac{x_A}{\rho_s x_R}. \tag{3.55}$$

The time evolution of the reconnected flux is given by Eq. (3.46). In the Hamiltonian case, $x_R = d_e$, we find

$$r = 1, \qquad \tau_1 = \frac{\pi}{2} \tanh(k_y L_x) \tau_A (k_y^2 d_e \rho_s)^{-1} \tag{3.56}$$

which gives $I_1(t) = 1 - \exp -t/\tau_1$. In the resistive case it is

$$r = 3/2, \qquad \tau_{3/2} = \Big(\frac{\pi}{2} \tanh(k_y L_x)\Big)^{2/3} \tau_A^{2/3} (k_y^2 \rho_s \eta^{1/2})^{-2/3} \tag{3.57}$$

These time scales are shorter than in the cold electron limit. In Fig. 3.2 the time evolution of $I_r(t)$ for the four values $r = 1/2, 5/4, 1, 3/2$ here examined is presented. Note that in the graph the time scales are normalized in order to be unity for each value of r.

From Eq. (3.17) it follows also that the time evolution of the Δ' is given by

$$\Delta'(t) = \frac{2k_y}{\tanh k_y L_x} \Big(\frac{1}{I_r(t)} - 1\Big). \tag{3.58}$$

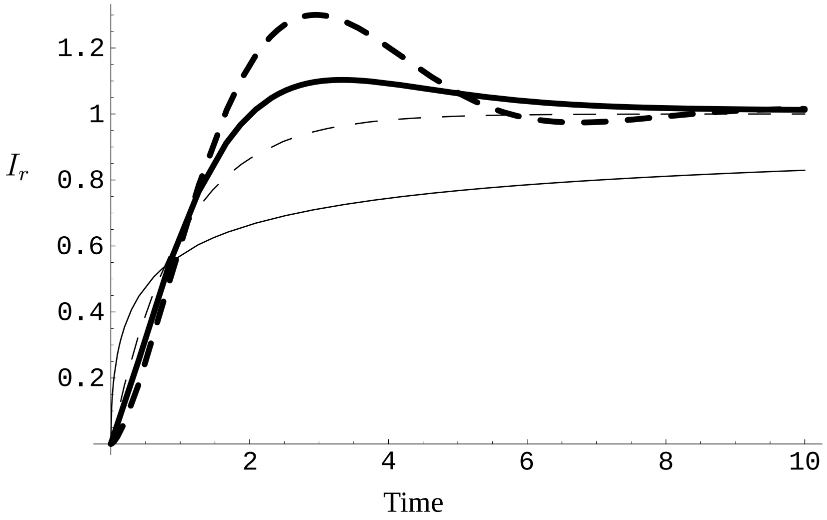

Figure 3.2: Time evolution of $I_r(t/\tau_r)$ for $r = 1/2, 1, 5/4, 3/2$, corresponding to Hamiltonian cases (thin lines), without ($r = 1/2$, continuous) and with ($r = 1$, dashes) electron temperature effects, and resistive cases (thick lines), without ($r = 5/4$, continuous) and with ($r = 3/2$, dashes) electron temperature effects, respectively.

3.1.3 The linear picture of forced reconnection

The picture of forced reconnection that we can expect from linear theory is the following. The forcing generates Alfvén waves which pile up magnetic flux at the neutral line, where island is formed. The island is a reconnecting mode driven by the displacement of the walls.

Several reconnection regimes can be distinguished, related to different relative magnitudes of the length scales x_R, ρ_s, x_A, and Δ'. Besides these plasma parameters, the modes that are actually present in the system depend on the time scale of the wall displacement, τ_{wall}. In the linear theory reported in the present section, τ_{wall} is so short compared with the time scale set by any linear growth rate that, as far as the reconnection process is concerned, the wall displacement follows a step function in time. In this way all the modes are excited, and they dominate the dynamics in different phases, according to their relative growth rates.

Since there is no vorticity in the equilibrium, no ρ_s effect is present initially. The first phase is dominated by the large Δ' in the cold electron regime. The radial electric field has a typical width of the order of x_R. It is localized inside the reconnection layer and its spatial structure is hardly connected with the external MHD solution. Flow cells are macroscopic, corresponding to the spatial structure of the displacement of the walls.

Once a vorticity field is build up, the inflow in the X point is enhanced by the presence of ρ_s and the growth rate increases. The mode continues to be internal,

with typical scale length of the order of ρ_s.
As reconnection proceeds the value of Δ' decreases. When the small Δ' regime is entered the structure of the electric potential changes and shows length scales of the order of $\sqrt{x_R x_A}$, while ψ is approximately constant inside the reconnection layer. At the same time reconnection slows down according to the new regime.
When the energy injected by the wall has been totally converted into magnetic energy (in the form of an island) and electron kinetic energy (in the form of a current sheet) the system approaches a stationary equilibrium. The way in which saturation occurs, with or without overshooting, depends on which is the relevant reconnection mechanism during the approach of saturation. If the dominant effect is resistivity, than the island size is expected to overshoot its saturation value. Otherwise, in the case of Hamiltonian reconnection, the saturation value is monotonically approached from below.
The final value of the reconnected flux is not influenced by x_R, but depends only on the amplitude of the initial perturbation. Using the parameters used for the numerical results of Section 4.2 in Eq. (3.46), the linear estimation of reconnected flux at saturation is $2\delta/\cosh k_y L_x \simeq 0.076$. This corresponds to an island of half width ~ 0.4.

In Chapter 4 this picture of forced reconnection is completed by nonlinear solutions that are obtained numerically.

3.2 Unstable perturbations

We now briefly summarize the linear theory for reconnection processes due to unstable perturbations [32]. Let us consider the equilibrium $\phi_0 = \omega_0 = 0$ and in $\psi_0 = -(L_s/\pi)\cos \pi x/L_s$ in the double periodic domain $(-L_x, L_x) \times (-L_y, L_y)$. For linear perturbations of the magnetic flux and the electric potential of the form $f(x,y,t) = \Re\{\tilde{f}(x)e^{\gamma t + i k_y y}\}$ with $k_y = \pi m/L_y$, Eqs. (3.1, 3.2) become

$$\gamma(\partial_x^2 - k_y^2)\tilde{\phi} = i v_A^2 k_\parallel \Big((\partial_x^2 - k_y^2)\tilde{\psi} + \frac{\pi^2}{L_s^2}\tilde{\psi}\Big) = 0, \tag{3.59}$$

$$\gamma\Big(\tilde{\psi} - d_e^2(\partial_x^2 - k_y^2)\tilde{\psi}\Big) - i k_\parallel \tilde{\phi}(1 + \frac{\pi^2}{L_x^2} d_e^2) + i \rho_s^2 k_\parallel (\partial_x^2 - k_y^2)\tilde{\phi} = 0, \tag{3.60}$$

with $k_\parallel = k_y \partial_x \psi_0 = k_y \sin(\pi x/L_x)$. With respect to the corresponding equations for the forced case, Eqs. (3.5–3.6), the different equilibrium magnetic flux gives a different form of $k_\parallel$, here it is a sine function of x while in the forced case it is linear in x. Moreover the equilibrium flux generates a space dependent equilibrium current, which in turn gives rise to the terms in π/L_s in the above equations. The equilibrium shear length is much larger than the electron inertia skin depth,

$d_e\pi/L_s \ll 1$, so the equilibrium current appears only in Eq. (3.59). Here the complex Fourier transform is employed both in time and in the y direction.

As in the forced case, outside a narrow layer around the neutral lines the corrections due to γ, d_e, and ρ_s can be neglected, thus the first equation reads

$$k_\parallel\Big(\partial_x^2\tilde{\psi} + (\frac{\pi^2}{L_s^2} - k_y^2)\tilde{\psi}\Big) = 0, \tag{3.61}$$

which again allows for discontinuous solutions on the neutral lines where $k_\parallel$ vanishes. The unstable solution to Eq. (3.61) is [32]

$$\tilde{\psi} = A\cos(\kappa|x| - \pi/2) \tag{3.62}$$

where $\kappa = \pi(L_s^{-2} - (m/L_y)^2)^{1/2}$, and A is an integration constant to be fixed by the asymptotic matching with the solution inside the reconnection layer. The solution Eq. (3.62) leads to $\Delta' = 2\kappa\tan(\kappa\pi/2)$. As explained in [32], instability is possible only when the factor in equation Eq. (3.61) is non negative, $\pi^2/L_s^2 - k_y^2 \geq 0$. This fixes the stability criterion that for a given aspect ratio L_s/L_y: the unstable modes are those with wave number, m, such that $0 < m \leq L_y/L_s$. For bigger m the external solutions change character, from sinusoidal to exponential, with negative Δ', and no instability is present [5].

In the inner region we can approximate $k_\parallel \simeq k_y\pi x/L_s$ and $\partial_x^2 \gg \pi^2/L_s^2, k_y^2$, obtaining the equations

$$(i\gamma)\tilde{\phi}'' = -v_A^2\frac{\pi k_y}{L_s}x\tilde{\psi}'' \tag{3.63}$$

$$(i\gamma)(\tilde{\psi} - d_e^2\tilde{\psi}'') = \frac{\pi k_y}{L_s}x(\tilde{\phi} - \rho_s^2\tilde{\phi}'') \tag{3.64}$$

which are the same as Eqs. (3.14, 3.15) with $i\gamma = s$. From this point on the solution inside the reconnection layer are those already presented in Sections 3.1.2 and 3.1.2. Because the mode is linearly unstable by construction, due to the choice of k_y, the analysis cannot give, as in the Taylor problem, any indication about an eventual saturation of the island growth. Extension of this model in the nonlinear regime have been investigated in [33], and a numerical comparison with the forced case is reported in Chapter 4.

3.3 Tokamaks and slabs, kink and tearing modes

The layer equations, Eqs. (3.14–3.15), apply to different modes and physical systems. Due to the narrowness of the resonant layer, and with the limitations already discussed in Section 1.3, the layer equations are the same regardless to the specific structure of the external MHD mode. Instead, the physics of the external region change the boundary conditions at the resonant layer to which the inner solutions are subjected.

The neutral surface is where there is a local minima of the magnetic potential. So close enough to the neutral surface the magnetic potential can be always approximated by a quadratic term (plus a constant). On the other hand, as discussed in Chapter 1, approaching the ideal region from inside the reconnection layer, the parallel electric field must vanish. This gives a relation between the electrostatic potential and the magnetic flux (which is equivalent to put $\rho_s = d_e = \eta = 0$ in Eq. (3.15)). It follows that also the spatial dependence of the electrostatic potential close to the neutral line can be approximately given regardless of the structure of the MHD solution on larger scales. Hence, using the formalism of [29], the external MHD solutions close to the neutral layer can be always written as

$$\tilde{\psi}(x) = g\Big(C_1 - C_2 x \text{ sgn } x\Big) \tag{3.65}$$

$$\tilde{\phi}(x) = \frac{L_s s}{k_y} g\Big(\frac{C_1}{x} - C_2 \text{ sgn } x\Big) \tag{3.66}$$

where the geometrical factor $g = L_s k_\|' / k_y$ is unity for a locally quadratic flux. This solutions holds for magnetospheric and tokamak plasmas, in the large and small Δ' regime, for arbitrary poloidal wave number m, including the $m = 1$ kink mode and reconnecting modes. What does change in all these cases are only the values of the two constants, C_1 and C_2. For instance, Eqs. (3.66) are Eqs. (3.23, 3.24) for $C_1 = A$ and $C_2 = -k_y \tilde{\phi}_R / s L_s$. As explain in detail in [29], the internal kink mode in a tokamak is described by

$$C_1 = C_2 \frac{2}{\pi} \lambda_H, \qquad C_2 = \frac{1}{2} \xi_\infty \tag{3.67}$$

where λ_H is the ideal MHD growth rate normalized to the Alfvén time and ξ_∞ is the value of the displacement at the magnetic axis. For the $m = 1$ reconnecting mode and $m \geq 2$,

$$C_2 = -\frac{1}{2} C_1 \Delta', \qquad C_1 = \frac{A}{g}. \tag{3.68}$$

The large Δ' regime is obtained for small C_1 but C_2 finite, so that in $\tilde{\psi}$ the constant term is negligible. The complete plethora of solutions can be found in [29] and [27].

3.4 Non stationary solution

In this section two non stationary limits of the linearized system of equations Eqs. (3.5–3.6) are discussed.

3.4.1 Ideal, non stationary solution

Setting $d_e = \rho_s = 0$ in the linear Eqs. (3.5–3.6), the system is reduced as

$$\partial_t^2 \Delta_k \Big(\frac{\tilde{\psi}}{x}\Big) + \frac{k_y^2}{L_s^2} x v_A^2 \Delta_k \tilde{\psi} = 0 \tag{3.69}$$

where $\Delta_k = \partial_x^2 - k_y^2$. In the large wavelength limit, $k_y^2 \gg \partial_x^2$, with $k_\parallel = k_y \partial_x \psi_0 = k_y x / L_s$, we get

$$\partial_t^2 \tilde{\psi} + v_A^2 k_\parallel^2 \tilde{\psi} = 0 \tag{3.70}$$

which has solutions in terms of harmonic functions. Introducing the eikonal $\theta(x,t) = k_y x t v_A / L_s$ we find that the waves have a continuous spectrum $\omega = -\partial_t \theta = -v_A k_\parallel$, and that small scales grow linearly in time: $q = \partial_x \theta = k_y t / \tau_A$. In the short wavelength limit, $\partial_x^2 \gg k_y$, and until the wavelength is larger than the ion sound gyroradius and the electron inertia skin depth, the ideal equation reads

$$\partial_t^2 \partial_x^2 \left(\frac{\tilde{\psi}}{x}\right) + \frac{k_y^2}{L_s^2} x \partial_x^2 \tilde{\psi} = 0, \tag{3.71}$$

or, equivalently,

$$\partial_t^2 w + v_A^2 k_\parallel^2 w = F(t), \tag{3.72}$$

where $w = \partial_x(\tilde{\psi}/x)$ and $F(t)$ is a function of time only to be fixed by boundary conditions. As explained in Chapter 2, with $\eta = d_e = \rho_s = 0$ the magnetic field topology is unchanged by the perturbation. Thus $w(0) = w'(0) = 0$ can be used as initial conditions. The above equation can be solved analytically [21] and the resulting magnetic flux is

$$\tilde{\psi}(x,t) = \frac{L_s x}{k_y v_A} \int_0^t d\tau F(\tau) \mathrm{Si}(\frac{k_y v_A}{L_s} x (t - \tau)), \tag{3.73}$$

where $\mathrm{Si}(v)$ is the sine integral function of v.

3.4.2 Small scale, non stationary solution

The case in which the typical perturbation wave length (or the slab width) is smaller than ρ_s, d_e corresponds to the condition $(d_e^2, \rho_s^2)\Big|\partial_x^2 - k_y^2\Big| \gg 1$, and leads to the equation for the perturbed current density $\tilde{J} = \Delta_k \tilde{\psi}$

$$\partial_t^2 \tilde{J} + \Big(k_\parallel^2 v_{th}^2\Big) \tilde{J} = 0, \tag{3.74}$$

with $v_{th} = v_A \rho_s / d_e$ being the thermal velocity. The solution is again a superposition of in harmonic functions with continuous spectrum and linearly growing small scales, where here “small” means small compared with d_e and ρ_s. This linear result has to be compared with the nonlinear results in Chapter 4, where a faster than exponential growth of small scales was found in the vicinity of the X-point.

4. Nonlinear dynamics

In this chapter we report the numerical analysis done on the system of equations derived in Chapter 2. The main characteristics of the reconnection process are analyzed in the general case of a forced system. The reconnection process driven by a displacement of the wall embedding a plasma slab is numerically investigated in the resistive and in the Hamiltonian case.
The model derived in Chapter 2 was studied in the linear approximation in Chapter 3. In the forced case of Hamiltonian reconnection the linear approximation breaks down when the magnetic island reaches a width of the order of the electron inertia skin depth, d_e, or for large value of the forcing wall displacement, δ.

The numerical results presented here extend far into the nonlinear regime. In order to describe these results, an extension to nonlinear regimes of the Δ' defined in Chapter 3 is introduced. This extension is denoted by Δ'_{nl} and is used to describe the reconnection process in all its phases.
In the forced case, the system is strongly driven by the wall displacement into the large Δ'_{nl} regime The drive lasts for a relatively short interval of time but the large Δ'_{nl} regime is sustained well after the walls came to rest. When eventually the value of Δ'_{nl} decreases, reconnection slows down and the island approaches saturation.

Large part of this chapter is devoted to the analysis of sub-layer structures which develop close to the X point in the nonlinear stage of the reconnection process. These structures have length scales much smaller than any other one in the model, and they are found to be created at a faster than exponential rate. The process has the features of a scale collapse.
The connection between the scale collapse close to the X point and the symmetry of the excitation is exploited. In particular, the reconnection process is generally induced by a wall displacement which is a symmetric modulation on the two sides of the neutral line. This highly symmetric configuration can be avoided by asymmetric forcing. In this case small scale close to the X points are not formed.
Part of these results been published in [34] and [35].

The last part of this chapter is devoted to the comparison between the forced and the unstable cases. In the latter, the reconnection drive is a tearing unstable mode, see Section 3.2.
Despite the complete difference in the reconnection drive, the topology of the solutions close to the X point is found to be the same in both the forced and unstable case. This similarity goes as far as including even the formation of sub-layer structures close to the X point, their length scales and their time evolution.
At last it shown that ion viscosity does not appreciably alter the reconnection

process on the d_e scale. On the other hand, the effect of ion viscosity on small scales is important when the island approach saturation in the forced case. Here the combined presence of ion viscosity and saturation stops the scale collapse.
The results presented in this part of the chapter has been published in [40].

4.1 The numerical implementation

In this chapter the results of the numerical solution of Eqs. (2.16–2.18) are reported. The set of employed boundary conditions are specified in details in Section 4.3.3, for both the forced and unstable cases.

Equations (2.16–2.18) are of mixed parabolic-elliptic type. The mixing between the two types limits the applicability of numerical methods which generally can solve either one or the other type of differential equation.
Moreover, Eqs (2.16–2.18) contain several length and time scales. These are the shear length L_s, the electron inertia skin depth d_e, the ion sound gyroradius, ρ_s. The time scales involved are the Alfvén time, $\tau_A \equiv L_x/v_A$ and the linear reconnection time scale, s of Eq. (3.39). Two additional parameters characterize the excitation in the forced case, the amplitude δ and time scale τ_{wall} of the wall displacement. Physical considerations and consistency with the ordering of the model give the inequality chain $L_y \gg L_x \gg \rho_s,\ d_e$ and $\tau_A \ll \tau_{wall} \ll s^{-1}$. Additionally, numerical studies show the formation of very steep gradients in different part of the computational domain. These gradients require to resolve length scales that are 10^{-4} smaller that the large physical scale, L_x. From these considerations it follows that the numerical code must be able resolve a very wide spectrum of time and length scales.
Finally, the implementation of different boundary conditions is needed in order to allow for different excitation schemes of the reconnecting instability.

The mathematical complexity of parabolic-elliptic equations, the wide spectrum of length and time scales, and the required flexibility on boundary conditions make the numerical solution of Eqs. (2.16–2.18) a challenging numerical task.
All numerical results presented here are obtained with the vectorized code *Vlugr2* [36] which employs a 2^{nd} order implicit finite-difference method and uses adaptive, local uniform grid refinement.
While implicit and finite-difference methods are well known, adaptive grid refinement is a relatively new tool and deserves a brief introduction. The grid refinement technique is a sophisticated numerical method which allows to concentrate very high numerical resolution only where and when it is needed. The system of equations is advanced in time by the implicit, finite-difference solver, starting with a given resolution. Each time that gradients of the solutions exceed a user defined

threshold in any node of the grid, that node is flagged, together with its eight first neighboring nodes. As a result a sub-grid of critical nodes is built at each time step. The number of grid points in the sub-grid is then increased by doubling the resolution in the two directions. The sub-grid is then filled with the values of the solutions at a time step preceding the one in which the problem of poor resolution was encountered. The solutions are advanced in time on the refined sub-grid and then checked for high gradients. If the check reveals no new critical nodes, then the solution is finally injected back in the original grid and the code move forward to solve the next time step. If critical nodes are found also in the refined sub-grid then the whole process of refining is repeated to a third grid level. The number of possible grid levels is limited by the available numerical power only.
The adaptive grid refinement has two powerful characteristics. The first one is that higher and higher resolution are employed only in the neighborhood of critical nodes. The second result is that the sub-grids structure can change at each time step, in this way following in time the region where higher resolution is needed. Figure 4.1 shows the grid structure in a case where two grid levels were used in addition to the basic grid. The example reported in figure is the grid scheme corresponding to the results in Fig. 4.13.

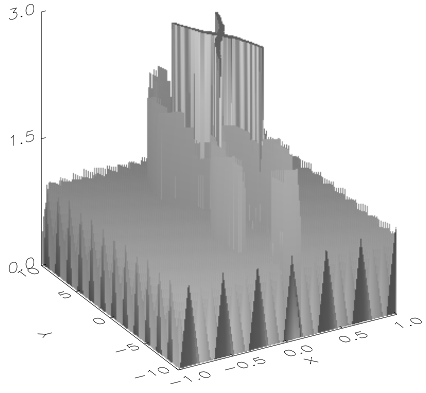

Figure 4.1: Grid structure at $t = 100\ \tau_A$ for the numerical computation of results in Fig. 4.13

The code turned out be prone to numerical instabilities when used to solve the aforementioned set of equations. This was likely due to the strict mathematical requirements that the system of equations has to satisfy in order the grid refinement to be smoothly applicable. As a consequence, the range of parameters that could be scanned was limited, and sometimes ion viscosity was needed to smooth grid size oscillations. Such limitations will be stated whenever relevant.
However, all the results presented here are checked for numerical errors. This is done in three ways. The first check concerns the spatial resolution with which

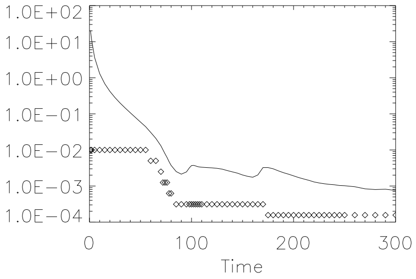

Figure 4.2: Resolution check. Diamonds represents the used resolution in the x direction, the continuous line shows the smallest length scale in the numerical solutions, as a function of time, in a typical case

small scales are resolved. In Fig. 4.2 the minimum employed resolution and the smallest scale are plotted in a typical case. The resolution is always sufficient.
A second test of our numerical scheme makes use of the Lagrangian properties of the studied equations. The formulation in Eq. (2.20) implies that the generalized fluxes $G_\pm$ preserve their initial topology. When ion viscosity is not used, the conservation of the topology of the generalized fluxes is preserved during all the simulation time here presented up to the highest employed resolution.
A last, and most important, test is the direct comparison between the results obtained with our code with those obtained with a totally different code, as explained in Section 4.3 for the unstable case.

It is also verified that the presence of small dissipation does not influence the large scale behavior. More details about the effects of ion viscosity are given in Section 4.3.5.

4.2 The forced case

Equilibrium configuration and forcing scheme of the current carrying slab are analogous to those employed for the analytical studies in Chapter 3. Here the numerical extension to nonlinear regimes is presented.
The initial magnetic configuration is a plasma slab $(-L_x \leq x \leq L_x, -L_y \leq y \leq L_y)$ confined by two flux conserving walls in $x = \pm L_x$ and periodic in the y direction. The equilibrium magnetic flux is quadratic, $\psi(t=0) = x^2/2L_s$, with a neutral line in $x = 0$. The equilibrium current is constant, $J = 1/L_s$. No flow is initially present, $\phi(t=0) = \omega(t=0) = 0$.
The equilibrium configuration is stable, thus reconnection must be imposed from the outside. The system is excited by a displacement of the walls at $x = \pm L_x$,

given by

$$x = \pm L_x \mp \delta(t), \qquad \delta(t) \equiv \delta_{wall} \cos(k_y y) \tanh(t/\tau_{wall}), \tag{4.1}$$

where $k_y = \pi/L_y$, $\delta_{wall} = 0.04$, $\tau_{wall} = 10$, $L_x = 1$, and $L_y = 10$ are the used parameters. The displacement is rendered on the—fixed—computational domain by imposing the value of the fields in $x = \pm L_x$ given by Eq. (3.9) with $\delta(t)$ given by Eq. (4.1). In this way the magnetic flux is conserved by the wall. The drive lasts for a finite interval of time of the order of τ_{wall}.

The system of equations, together with the above boundary and initial conditions, are such that ψ and J (resp. ϕ and ω) are even (resp. odd) functions of x and y. This allows to reduce the computational domain to the first quadrant only. In the following lengths are normalized to the shear length, $L_s = L_x$, and time to the Alfvén time, τ_A.

In Section 3.1.3 the time evolution of forced reconnection according to linear theory is discussed. One of the features that linear theory predicts is that the rate of reconnection is larger for larger Δ'. We are interested in fast reconnection processes, thus simulations should start in this regime. The parameter which drives reconnection is basically the time scale of the wall displacement, τ_{wall}. By choosing τ_{wall} larger then the Alfvén time but smaller than any reconnection time scale, a mode in the large Δ' regime is excited.

The linear theory developed in Chapter 3 predicts the evolution of the reconnection process according to the value of the Δ' as defined in Eqs. (3.10, 3.16). In order to create the interpretation tools for the nonlinear evolution of the reconnection process it is useful to find a homology of the Δ'. The definitions of Δ' in Eqs. (3.10, 3.16) are asymptotic, and cannot be applied directly to numerically obtained solutions which do not have a clear ideal MHD limit. However it is possible to introduce a heuristic measure for Δ' in the following way. The quantity $2\partial_x \tilde{\psi}/\tilde{\psi}|_{y=0}$ computed along $y = 0$ depends on x and on time. Its graph as a function of x is shown in Fig. 4.3 at $t = 20$. At each time the local maximum of that expression

$$\Delta'_{nl}(t) \equiv \max_x 2\partial_x \tilde{\psi}/\tilde{\psi}|_{y=0} \tag{4.2}$$

is assumed to play a role analogous to that of the $\Delta'(s)$ defined in Chapter 3.
By analogy with the language of linear theory, we define large and small Δ'_{nl} regimes as numerical solutions for which the product of Δ'_{nl} times an estimate of the mode width is larger or smaller than unity, respectively.
In the following it is shown that Eq. (4.2) is a proper tool for the description of different phase of the nonlinear evolution of the reconnection process.

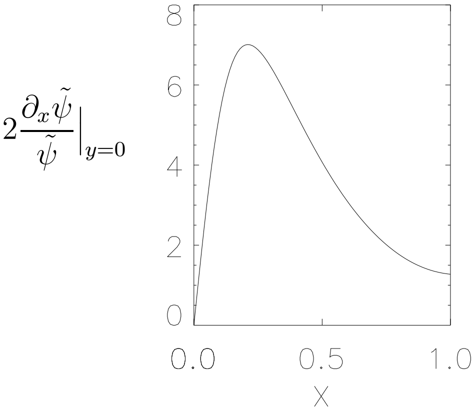

Figure 4.3: Graph of $2\partial_x\tilde{\psi}/\tilde{\psi}|_{y=0}$ as a function of x for $d_e = 0.18$ at t=20

4.2.1 Reconnection on the scale of d_e

The results presented in this subsection are for finite values of d_e, and $\rho_s = 0$, $\eta = 0$. Finite ion viscosity, $\nu_i = 10^{-4}$, was used because of the aforementioned numerical problems.

The walls move for a finite interval of time and excite Alfvén waves inside the system. The Alfvén waves generated by the wall displacement carry flux toward the neutral line. Due to the fluid incompressibility the magnetic flux at the neutral line is instantaneously perturbed, and reconnection lead to the formation of a magnetic island, see Fig. 4.4.

The walls are flux conserving, so the structure of the magnetic flux along y is imposed by the profile of the wall perturbation. The island is a single harmonic

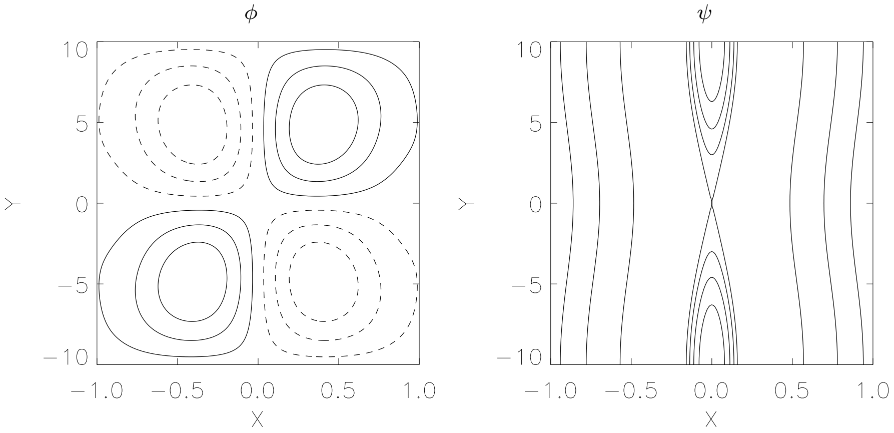

Figure 4.4: Isolines of the electric potential ϕ and of the magnetic flux ψ, for $d_e = 0.18$ at t=20.

mode with period equal to twice the box length, L_y, symmetric with respect to $x = 0$ and $y = 0$. Thus the X point is located at the origin of the coordinate system.
In this initial phase the mode structure is determined by the excitation. The flow cells extend through distances of the order of the box width, and the vorticity takes a quadrupolar structures on similar scales, see Fig. 4.4. The width of the reconnecting mode can be estimated from the isolines of ϕ shown in Fig. 4.4 as $w \sim d_e$. The time evolution of the numerical $\Delta'_{nl}(t)$ is given in Fig. 4.5 for $d_e = 0.1, 0.18$. Indeed, the strong initial drive forces the reconnection process to start in the large $\Delta'_{nl}(t)$ regime, $\Delta'_{nl}(t) w \geq 1$. The large $\Delta'_{nl}(t)$ regime lasts far inside the nonlinear regime. The two curves in Fig. 4.5 show that $\Delta'_{nl}(t)$ is almost proportional to

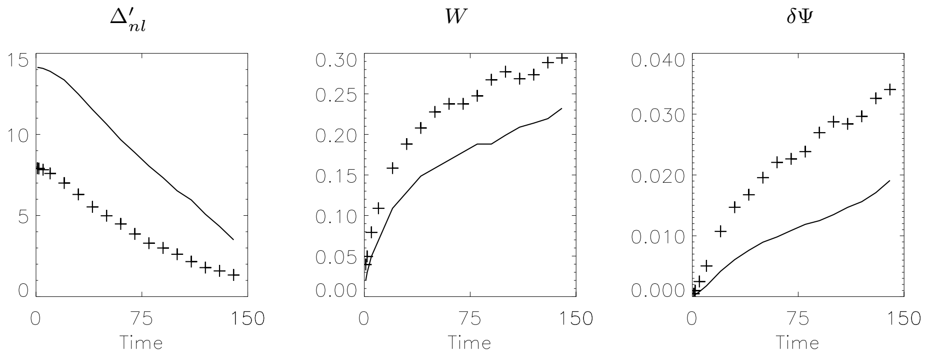

Figure 4.5: Time evolution of $\Delta'_{nl}(t)$, island width W, and the reconnected flux $\delta\Psi$, for $d_e = 0.1,\ 0.18$ (line, crosses, respectively)

d_e^{-1}, and it has an algebraical dependence on time.
Initially the strong drive of the wall displacement corresponds to high values of Δ'_{nl}. Then the walls come to a rest. With the proceeding of reconnection the value of $\Delta'_{nl}(t)$ drops.

The time evolution in the large Δ' regime of a forced system cannot be obtained by linear theory, see discussion in Section 3.1.2. The result for the unstable case Eq. (3.39) cannot be applied to the forced one because the growth rate in the forced case is driven by the wall displacement, and it can be initially even faster than in the unstable one, see Fig. 4.27 and Section 4.3. There this case is analyzed in detail as part of the comparison between forced and unstable cases.

The reconnection process is obviously faster for larger d_e. In Fig. 4.5 are shown the time evolution of the half width of the island measured at $y = L_y$, and of the reconnected flux, $\delta\Psi$, defined as the difference in the magnetic flux between the X and the O points,

$$\delta\Psi \equiv \psi(0,0) - \psi(0,L_y). \tag{4.3}$$

The reconnection scale is set by inertia. The island width quickly reaches dimensions comparable with d_e and keeps growing well beyond it. At this stage the regime is already nonlinear.

The value of the magnetic flux in the X point is that on the separatrix, so it is related to the island width. In the case of a flux perturbation that has a single harmonic in y of period $2L_y$ the island half width is given by $W = \sqrt{2L_s\delta\Psi}$. In Fig. 4.6 W is plotted as a function of $\sqrt{2L_s\delta\Psi}$ and compared with the numerical results for $d_e = 0.1,\ 0.18$. The island width is always larger than what the single mode approximation would predict.

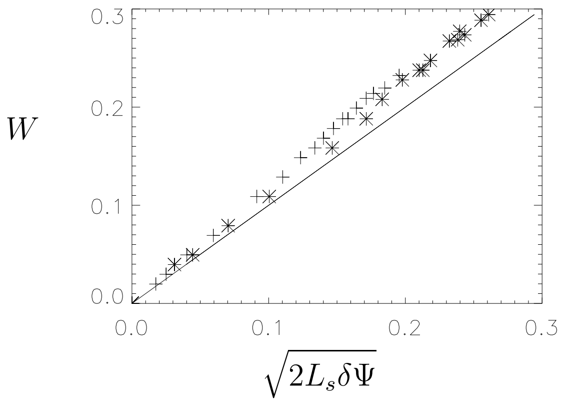

Figure 4.6: Scatter plot of W versus $\sqrt{2L_s\delta\Psi}$, for $d_e = 0.1,\ 0.18$ (resp. crosses, stars); the continuous line represents the single mode approximation

While the island grows, the magnetic flux piles up towards the neutral line and generates a current sheet. This is shown in the surface plot of the current density at $t = 100$ in Fig. 4.7. The current sheet is centered at the X point and extends along the y direction. The Alfvén waves generated by the wall displacement can also be recognized.

The time evolution of the current sheet can be described by means of its width and maximum value. The width of the current sheet is taken to be the half width at half maximum (HWHM) along $y = 0$. The time evolution of this width is shown in Fig. 4.8. Starting from the very initial phase, this width decreases somewhat slower than exponentially in time. It is interesting to note that the time behavior hardly depends on the value of d_e, indicating that the current sheet formation is mainly an ideal MHD process.

The maximum of the current density is located at the X point, due to the symmetry properties of the system, and its time evolution is shown in Fig. 4.8. The

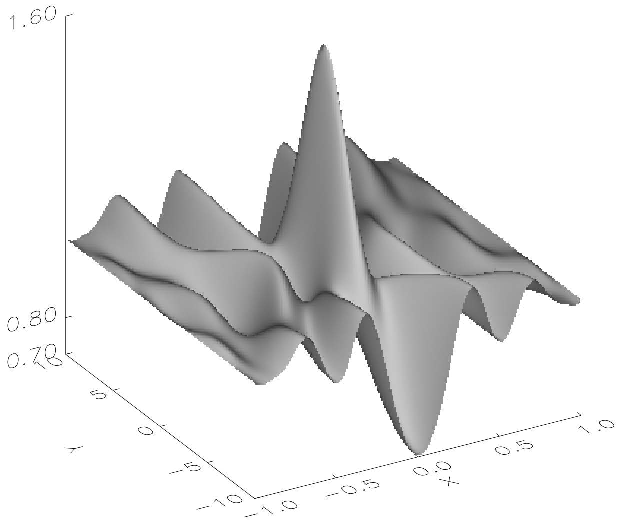

Figure 4.7: Surface plot of the current density at $t = 100$ for $d_e = 0.18$

maximum of the current density is higher for smaller d_e. This is due to the fact that close to the X point $\partial_t(\psi - d_e^2 J) = 0$ holds, all other terms in Eq. (2.17) being zero by parity. Thus the term $d_e^2 \partial_t J$ has to balance the time evolution of ψ,

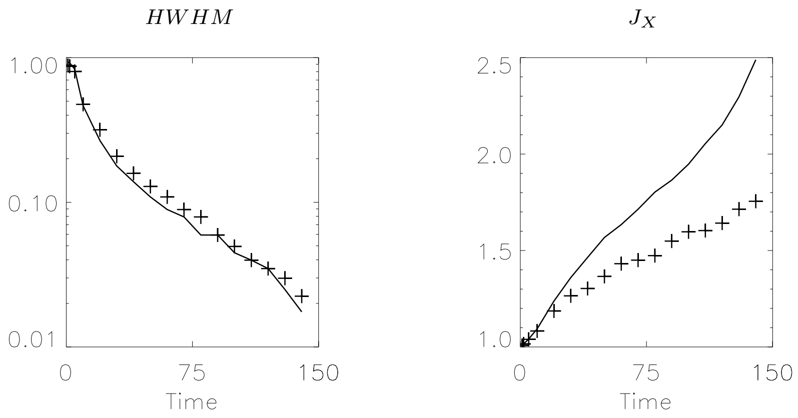

Figure 4.8: Current density HWHM, value of the current density in the X point, for $d_e = 0.1, 0.18$, (line, crosses resp.)

i.e. of the reconnected flux. Integrating in time, from $t = 0$ with initial conditions $\psi(x = 0, y = 0, t = 0) = 0$, $J(x = 0, y = 0, t = 0) = -d_e^2$, the difference in current density between X and O point is given at any t by

$$\delta J(t) = d_e^{-2}\delta\Psi(t). \tag{4.4}$$

This relation implies that the current maximum for comparable values of the reconnected flux (or island widths) is higher the smaller is d_e, as in Fig. (4.8). In the limit $d_e = 0$ the current tends to diverge at the neutral surface as in the ideal MHD case.

Some of the characteristics exposed above are related to the presence of conserved fluxes, as Eq. (4.4). As discussed in Section 2.3, in the cold electron limit only one generalized flux exists, namely $F \equiv \psi - d_e^2 J$. This flux is passively advected by the electrostatic potential ϕ, that plays the role of the stream function. At $t = 0$ the isolines of F are straight lines parallel to the y axis. As the wall perturbation proceeds, the formation of convection cells in the stream function generates a velocity field $\mathbf{e}_z \times \nabla\phi$. The stream function ϕ is odd in x and y. Then the velocity field carries the F isolines toward the X point, while dragging them away from the O point, see Fig. 4.4. This process generates increasing gradients in F in the proximity of the X point. The equation $\partial_t F + [\phi, F] = 0$ implies that the integral of F between two flux surfaces of F is conserved in time. Consider two flux surfaces that enclose the island. Here the contribution to F of the current density has to compensate for the change in the magnetic flux. Thus, as already described above, the current increases in the X point and decreases in the O point, and the larger the reconnected flux, the larger the maximum of the current sheet will be. The increasing density of F isolines in the neighborhood of the neutral line corresponds to the formation of the current sheet.

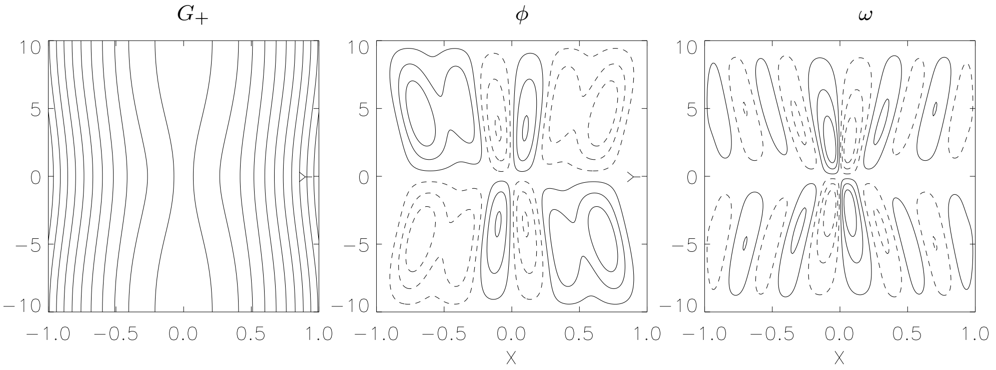

Figure 4.9: Isolines of F, ϕ, and ω at $t = 100$ for $d_e = 0.18$

As it was described before, initially the strong forcing due to the wall displacement drives the system in the large $\Delta'_{nl}(t)$ regime. The large Δ'_{nl} regime lasts well inside the nonlinear phase, long after the wall displacement came to a rest. When eventually the small Δ'_{nl} regime is entered also the field structure changes. The vorticity is for large part inside the island, and scales smaller than d_e start to develop in ϕ, see Fig. 4.9. The very final stage of the reconnection process is the island saturation, which happens for small Δ'_{nl}. Because of Eq. (4.4), both ψ and J in the X point depend on the same way on time, and the saturation of the island implies the saturation of the current growth. In other words, the current density reaches its maximum for the largest value of the island width. Hence, the final configuration is a magnetic island with a current sheet.

The final saturated island stage was not obtained numerically in the present case due to limitations of the numerical code. However, the saturation stage is reached in the case of finite electron temperature, as reported in Section 4.2.2.

Comparison with resistive reconnection

The linear regime of resistive reconnection was studied in Chapter 3. The nonlinear regime was studied in [21]. Here we want to comment upon some of the salient differences between the Hamiltonian and the resistive reconnection in the framework of a forced system.

If the electron inertia skin depth d_e and the ion sound gyroradius ρ_s are smaller than the resistive layer width, then resistivity is responsible for magnetic field line reconnection.

In resistive reconnection the width of the current channel is determined by the ideal dynamics until resistive diffusion becomes important. Subsequently, the width of the current channel is limited by diffusion. Comparing the width of the current channel when the maximum in the X point is reached for different values of η, the current layer width was found [21] to scale with resistivity as $\eta^{1/2}$. The same scaling is found in the Sweet-Parker model, see Section 1.2, suggesting that in the forced case the reconnection process behaves almost as a stationary case. Thus, in the forced case, when $d_e, \rho_s \ll \tau_A^{1/2}\eta^{1/2}$ resistivity is responsible for local violation of the frozen in law for the magnetic potential.

As in the Hamiltonian case for F, the wall displacement generates convection cells which drag ψ isolines toward the neutral line. The reconnection process generates a current sheet along the neutral line whose spatial structure is similar to that of the current sheet generated in the Hamiltonian case, see Fig. 4.10. Indeed, in the initial phase the non ideal effect of resistivity does not influence the dynamics, except for the formation of the island. Figure 4.11 shows the time evolution of the current maximum and width in the Hamiltonian and resistive case. There

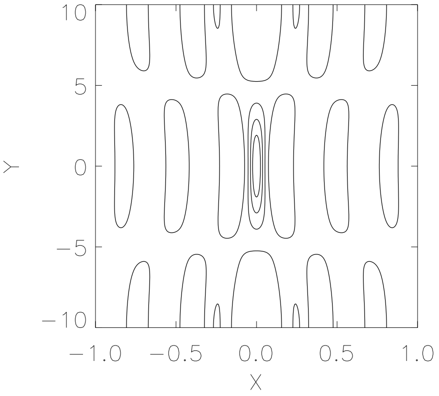

Figure 4.10: Isolines of the current density J for $\eta = 10^{-5}$ at $t = 70$

is no appreciable difference between the two curves until the width of the current becomes approximately one order of magnitude smaller than L_x.

The two curves in Fig. 4.11 start to differ when the current width reaches the scale of the electron inertia skin depth. While in the resistive case the current maximum keeps growing exponentially, in the Hamiltonian case the growth slows down, due to the link between current and reconnected flux, Eq. (4.4).

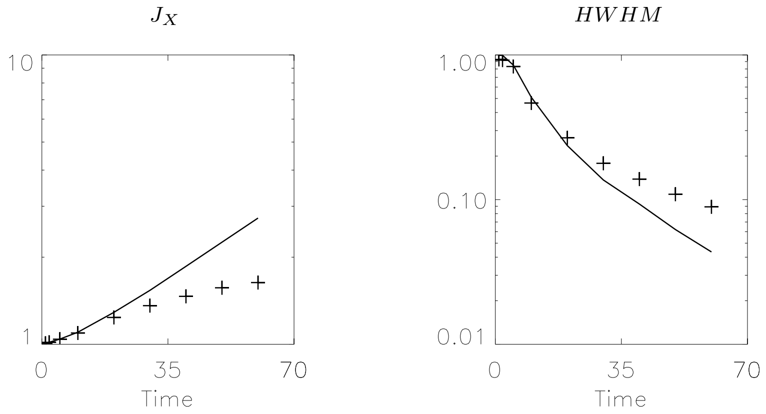

Figure 4.11: Time evolution of the current in the X point, and current density HWHM in the resistive (line, $\eta = 10^{-5}$), and cold electron (crosses, $d_e = 0.18$)

In the resistive case the momentum balance equation Eq. (2.17) in the X point reduces to $\partial_t \psi = \eta J$. Hence, relatively small variations of the reconnected flux correspond to rather large increments of the current maximum. In this case the current difference between X and O point is given by

$$\delta J(t) = \eta^{-1} \partial_t \delta\Psi(t) \tag{4.5}$$

so that the maximum value of the current is for the highest growth rate, and it decreases subsequently as the island approaches saturation, until vanishing when the island saturates. In contrast to the Hamiltonian case, the final configuration is a magnetic island without current sheet close to the X point.

For comparison, we recall that in the Hamiltonian case the width of the current channel is independent on the scale associated with the reconnection mechanism, *i.e.* d_e. In that case the current channel keeps shrinking, at least until the magnetic island saturates.

In the unstable case the resistivity is responsible for the violation of the frozen in law if $d_e,\ \rho_s \ll \tau_A^{1/3} k_y^{-1/3} \eta^{1/3}$ in the large Δ' regime and $d_e,\ \rho_s \ll \tau_A^{1/5} k_y^{-3/5} \eta^{1/5}$ in the small Δ' regime, respectively.

4.2.2 Ion sound gyroradius effects

Ion density perturbations are related to the electric potential by Eq. (2.13). Quasi neutrality, via the coupling with electron pressure, introduces in the system the ion sound gyroradius, ρ_s. This additional scale length modifies the advection of ψ in the momentum balance equation, as explained in Chapter 2.2. Moreover, in this case the equations are expressed in terms of conservations of two generalized fluxes $G_{\pm}$,

$$G_{\pm} = \psi - d_e^2 J \pm (\rho_s d_e / v_A)\omega, \tag{4.6}$$

see Section 2.3.

In the present subsection the numerical simulation for non zero values of d_e and ρ_s are presented. Dissipation is limited to small ion viscosity, $\nu_i = 10^{-5}$, but resistivity is omitted, $\eta = 0$.

The first and most striking difference with the cold electron case is the spatial structure of current density and vorticity. Figure 4.12 shows that two current layer are formed that intersect each other at the X point (compare with the surface plot of the current density in the cold electron temperature limit in Fig. 4.7). The same structure is clearly visible also in the isolines of the current density in Fig 4.13.

This peculiar structure is related to the Hamiltonian character of the system of equations, as has been clarified in [15]. The two generalized fluxes $G_{\pm}$ are advected by the corresponding generalized stream functions $\Phi_{\pm} \equiv \phi \pm v_{th}\psi$. Due to the symmetry properties of ϕ and ψ, the generalized fluxes $G_{\pm}$ and the stream functions $\Phi_{\pm}$ are each other mirror image. The isolines of G_{+} and Φ_{+} are shown in Fig. 4.14 in a typical case (an analytical example of $\Phi_{\pm}$ is reported in Fig. (6.2), where the reader has to change $v_{\parallel}$ into $v_{th} = v_A \rho_s / d_e$).

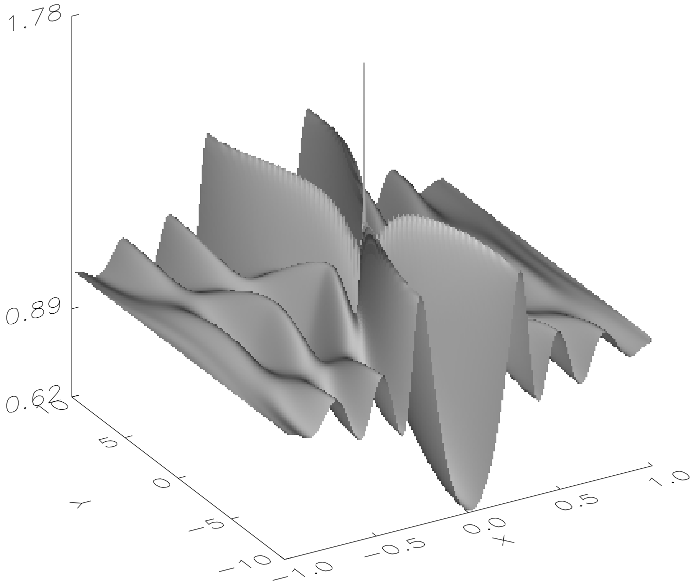

Figure 4.12: Surface plots of the current density at $t = 80$ for $d_e = \rho_s = 0.18$

Besides the $E \times B$ flow, the two velocities $\mathbf{e}_z \times \nabla\Phi_\pm$ contain a component due to the perpendicular magnetic field which has opposite sign. Along the lines $\Phi_\pm = 0$ through the X point the flow velocities vanish. The location of the lines $\Phi_\pm = 0$

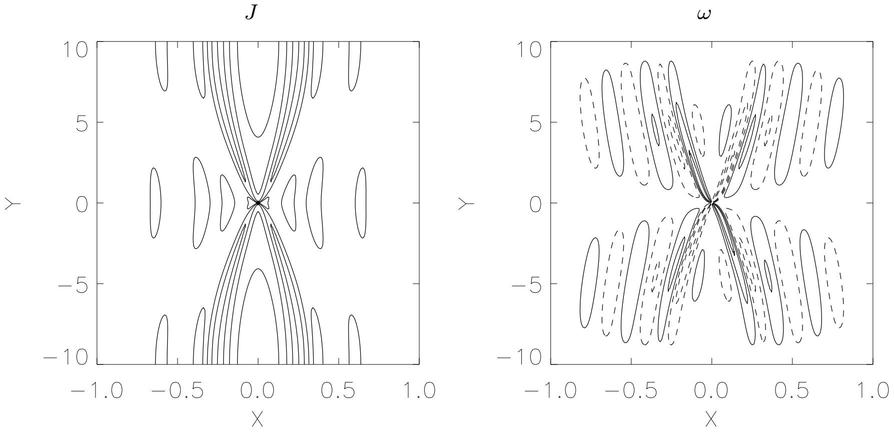

Figure 4.13: Isolines of the current density, and vorticity, at $t = 80$ for $d_e = \rho_s = 0.18$

is a function of ρ_s/d_e, and it is not at $x = 0$ as it was the case of the flow velocity in the cold electron case. Similarly to the cold electron case, the advection causes a piling up of the generalized fluxes along the line $\Phi_\pm = 0$ of the correspondent stream function.

As in the cold electron limit, see Section 4.2.1, the constancy of the integral of a generalized flux between two flux surfaces implies a balance between its components. This balance involves now not only current density and magnetic flux but also the vorticity. The piling up causes strong gradients in current and vorticity. In general, strong gradients are expected to appear similarly in both the fluxes. Then, because the current can be expressed as

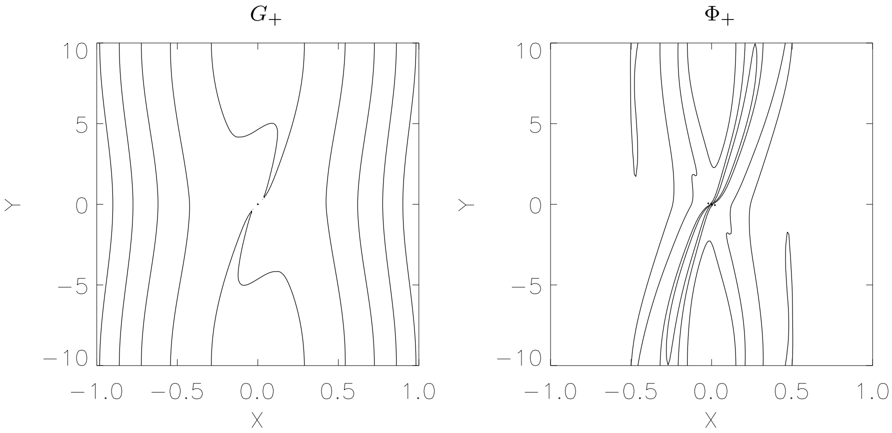

Figure 4.14: Isolines of G_+ and Φ_+ at $t = 80$ for $d_e = \rho_s = 0.18$; G_- and Φ_- are the mirror images with respect to $x = 0$

$$\frac{1}{2}(G_+ + G_-) = \psi - d_e^2 J, \tag{4.7}$$

it follows that $\psi - d_e^2 J$ as a superposition of the two fluxes has strong gradients along the lines $\Phi_\pm = 0$. The gradients in the generalized fluxes are responsible for the cross shaped structure in the current density. According to

$$\frac{1}{2}(G_- - G_+) = \frac{\rho_s d_e}{v_A}\omega, \tag{4.8}$$

similar structures are to be found in the vorticity field. Indeed, the same X shaped structure of the strong gradient regions are found in the vorticity too, as Fig. 4.13 shows.

In Fig. 4.15 the time evolution of the reconnected flux is shown. It is seen that the value of the reconnected flux is not affected by the ρ_s term in the early stage of reconnection. Similarly, also the structure of the magnetic flux and electric potential are largely comparable with those analyzed in the $\rho_s = 0$ case. Indeed, because the equilibrium vorticity vanishes, time is needed by the dynamics to

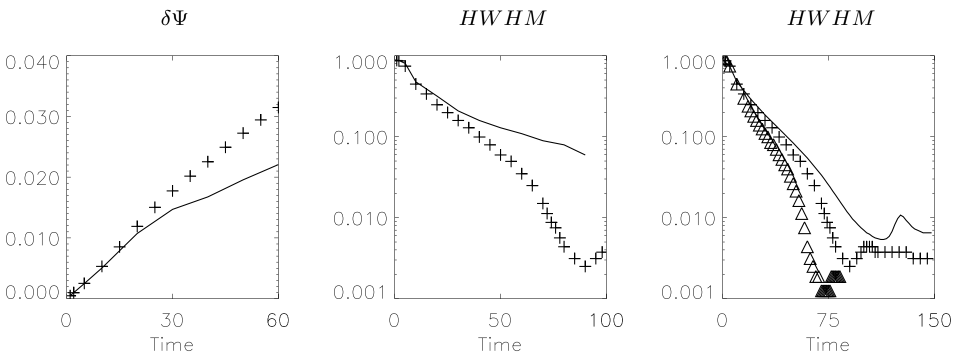

Figure 4.15: The reconnected flux, and current density HWHM for $d_e = 0.18$, for $\rho_s = 0$ (continuous line) and $\rho_s = 0.18$ (crosses); current density HWHM, for $\rho_s = 0.18$, $d_e = 0.1,\ 0.18,\ 0.25$ (resp. line, crosses, triangles)

build up a vorticity field which manifests the presence of ρ_s. However, as soon as the vorticity field becomes larger, the ion sound gyroradius term increases the inflow in the X point, and the reconnected flux rate is enhanced. The evolution of the reconnected flux and the island width are shown in Fig. 4.16 for three values of d_e. For a comparison with the cold electron limit refer to Fig. 4.5. The island

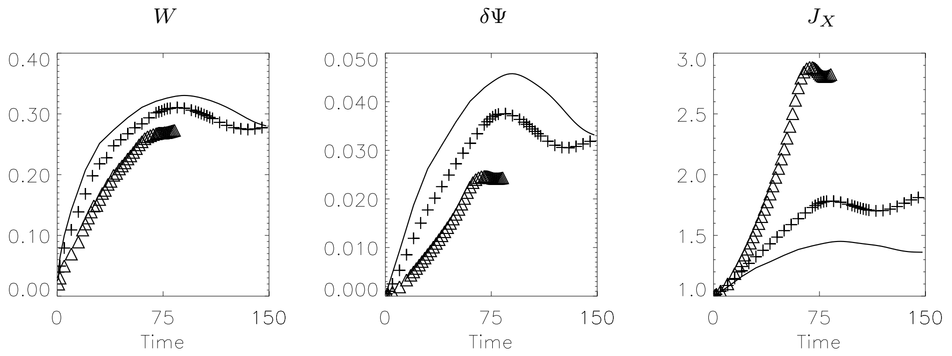

Figure 4.16: The island width, the reconnected flux, and the current density in the X point, for $\rho_s = 0.18$, $d_e = 0.25,\ 0.18,\ 0.1$ (resp. line, crosses, triangles)

reaches quickly the saturation level. An overshoot is clearly visible: the island size grows above the saturation level and then decreases. Note that, due to the parity of the term proportional to ρ_s, also in the case of finite electron temperature the considerations about the relation between the current in the X point and the reconnected flux given in Eq. (4.4) still holds. Thus the current density in the

X point it is higher for smaller d_e and it follows the same temporal law as the reconnected flux, as clearly visible in Fig. 4.16.

It is interesting to note that the width of the current density has a totally different behavior than the one for $\rho_s = 0$. Let us examine Fig. 4.15, where the time evolution of the current density width is shown for $d_e = 0.18$, and for $\rho_s = 0$ and $\rho_s = 0.18$.

In the first place, when the influence of ρ_s start to be felt, the shrinking of the current channel is dramatically accelerated, decreasing in few tens of Alfvén times well below all the length scales in the model. A similar process takes place in the y direction, leading to the formation of a very narrow current spike in the X point. This spike is visible in the surface plot of the current density in Fig. 4.12.

Secondly, in contrast to what is shown in Fig. 4.8, the finiteness of ρ_s introduces a dependence of the width of the current on d_e.

Both these features are to be related with the change that ρ_s introduces in the governing equations. In fact, because of the symmetry of the excitation, the strong gradients of $G_\pm$ overlap close to the X points. Because the current is approximately the overlap of the two fluxes, this results in the formation of the current spike. Indeed it is not possible to talk of a current sheet any more because the collapse happens along both the x and the y direction.

Moreover, the line $\Phi_\pm = 0$ along which the isolines of $G_\pm$ are compressed depends on the ratio ρ_s/d_e in $\Phi_\pm$. Hence the angle at which the overlap of $G_\pm$ take place, and of the resulting width of the current spike, depends on d_e/ρ_s. The width of the spike is larger for larger ρ_s/d_e.

The fact that the strongest gradients in the fluxes happen to be in the same spatial region is an outcome of the highly symmetric configuration employed. This last observation is questioned in Section 4.2.3, where it is shown that when the overlapping is avoided then spikes in the current are absent .

Small scale structures similar to those in the current density are also found in the vorticity. The overlapping of the odd part of the generalized fluxes creates huge gradients close to the X point.

The analysis of these large gradients in current density and vorticity is reported in Section 4.3, for both the forced and the unstable cases. While reconnection proceeds smaller and smaller scales are formed. At the same time $\Delta'_{nl}(t)$ decreases and reconnection slows down, as shown in Fig. 4.17. For small value of Δ'_{nl} different mode structures emerge. Comparing with Fig. 4.4, it can be seen that ϕ shows now length scales smaller than d_e. Note in Fig. 4.13 how most of the vorticity is concentrated in the two layers generated by the superposition of $G_\pm$. The saturation of the island takes place in the small $\Delta'_{nl}(t)$ regime. Form Fig. 4.16 two points can be made which are in contrast with the predictions of linear theory summarized in Section 3.1.3. First, the maximum value reached by the reconnected flux is smaller than linear predictions. This implies that the nonlinear

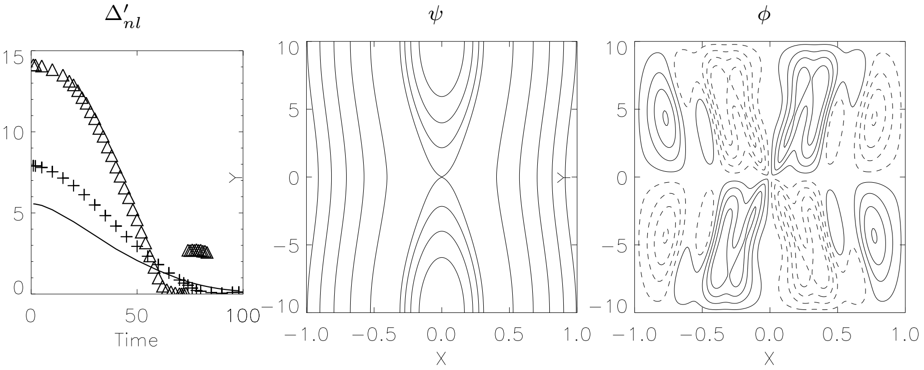

Figure 4.17: Time evolution of the $\Delta'_{nl}(t)$ for $\rho_s = 0.18$ and $d_e = 0.25,\ 0.18,\ 0.1$ (resp. line, crosses, triangles); isolines of ψ and ϕ, at $t = 80$, for $d_e = 0.18$

dynamics results in a saturation at a smaller width. Second, the saturation width does depend on d_e and not only on the perturbation amplitude.
The long time evolution of the island width is shown in Fig. 4.18. After the maximum is reached the system does not approach a static state but enters an oscillatory regime.

The results presented so far show that the $\Delta'_{nl}(t)$ defined in Eq. (4.2) is a proper tool to describe the whole reconnection process, from the forcing to the saturation. The different nonlinear features are connected with different regime in $\Delta'_{nl}(t)$, in the same manner as it is done in linear theory.

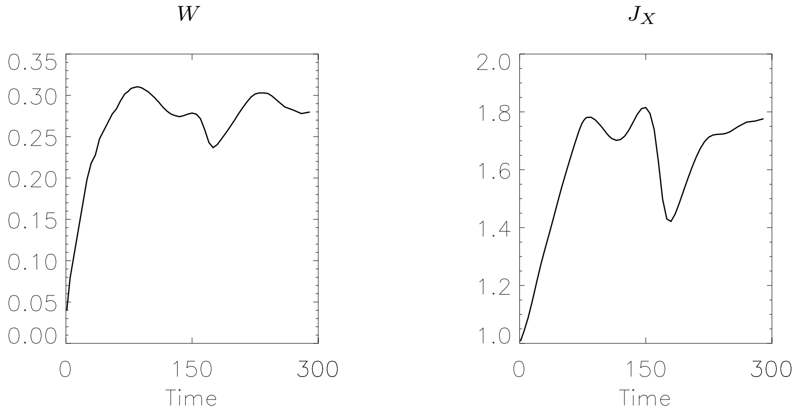

Figure 4.18: Time evolution of the island width W and current density in the X point J_X, for $\rho_s = d_e = 0.18$

Numerical simulations of collisionless reconnection in cylinder geometry reported in Ref. [37] show an explosive growth rate in the nonlinear stage. In that

paper it is reported that a reconnecting mode was started in the semicollisional regime and then entered a collisionless phase. After almost two hundred Alfvén times of practically quiescent evolution the growth rate suddenly jumped to almost five times its previous value. This burst lasted about fifty Alfvén times.
Figure 4.18 shows that in the present case there are rather large oscillations of the current density peak, but not explosive behavior is found.

Time evolution of the energy integral

The total energy is defined in Eq. (2.23). Figure 4.19 shows the time evolution of the energy of the fluctuations. The energy injection due to the walls displacement lasts for interval of time of the order of τ_{wall}. After that the total energy is constant in the dissipationless case, while it is slowly decreasing time in the viscous case.

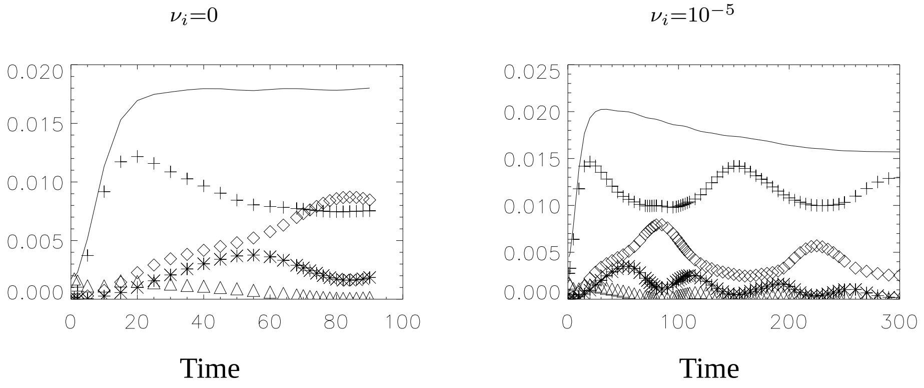

Figure 4.19: Time evolution in the inviscid and viscous cases of total (line), magnetic (crosses), parallel electron kinetic (diamonds), ion kinetic (asterisks) , and internal (triangles) fluctuations' energy, for $\rho_s = d_e = 0.18$

Initially, practically all the energy is converted in magnetic flux which piles up at the neutral line. Once the forcing is stopped the reconnection process decreases the magnetic energy. The magnetic energy is converted into kinetic and ion kinetic energy. This corresponds to the set up of the current sheet and of the $E \times B$ flow, respectively. The maximum of the electron kinetic energy is reached when the magnetic energy has a minimum, so at the saturation of the island.
Afterwards, the oscillating phase is entered. Similarly to what happens locally at the X point, also the contribution to the energy coming from the reconnected flux and from the current density have the same temporal evolution. In particular, when the magnetic energy has a minimum (corresponding to a maximum of the island width) the kinetic energy has a maximum, and *vice versa*.
The energy balance of the Hamiltonian reconnection process in the forced case

is driven essentially by an exchange between magnetic and electron kinetic energy. However, a fraction of the energy is confined in the $E \times B$ flow, and it is not converted in electron kinetic energy. Thus the island width never reaches the maximum value attainable in case of complete conversion of the injected energy into magnetic and kinetic energy.

Because the ion kinetic energy never vanish, not even when the island saturates, a stationary state is never reached, and the island width keeps oscillating. Despite the influence that electron compressibility has on the topology and on the reconnection rate, no much energy is associated with it. Even smaller is the fraction of energy that goes in internal energy.

Ion kinetic and internal energy have also the same temporal evolution, but, in contrast with the other two energy contributions, they oscillates in phase. Moreover, the oscillation period of ion kinetic and internal energy is the half than the one of magnetic and electron kinetic energy. The ion kinetic energy seems to follow the time evolution not of the magnetic energy but of its variation in time. In fact, during the excursion from maximum to minimum, the growth of the island first accelerate and then decelerate, approaching saturation. In this half period of the magnetic energy, the ion kinetic energy rises until the acceleration persists and decreases afterwards. This correspond to an entire period for the ion kinetic energy. In the second half period of the magnetic energy, from minimum to maximum, the ion kinetic energy repeats the same pattern despite the fact that the vorticity must now have reversed its sign inside the island in order to allow for the island contraction.

The reconnection process described in these pages is Hamiltonian. The system is in principle time reversible. As it was shown also in these chapters, the Lagrangian dynamics creates smaller and smaller scales. The corresponding gradients cannot be smoothed away because no dissipative mechanism is present. On the other hand a saturation is attained on large scales. The question is if the small scale creation goes on forever, factually preventing from the time reversal.

The spontaneous time reversal of a Hamiltonian reconnection process has never been observed in our simulations. On the contrary, the island reaches saturation and an oscillatory phase is entered.

In the energy picture above, the saturation of the island growth can have different explanations. The first possibility is that the energy that is injected in the system by the wall displacement and available for reconnection is exhausted. It is shown in Chapter 3 that ideal MHD predicts the existence of a static final state with modified topology and compatible with the increased energy injected by the wall displacement. Nonlinearly this state is not accessible because a finite amount of energy is in the $E \times B$ flow also after saturation.

A second possibility is that the island stops growing because starts to feel the presence of the walls. On the other hand the widths at which the island saturates in

the simulation of forced reconnection presented in this thesis are always smaller than half of the slab width. It is then plausible to exclude any direct influence of the walls in limiting the maximum island size which is dynamically reachable.
Lately [38] phase mixing was proposed as the mechanism for accessing new macroscopic equilibria. The main idea is that part of the total energy is confined in small scale structures, which still count in the energy balance but not in the determination of the large scale dynamics. In this sense it is possible that the large scale dynamics admits a coarse grained equilibrium configuration. To this explanation is essential the presence of small scale structures in the generalized fluxes. As is explained in Section 4.2.3, structures like the current spike in the X point are not necessary present in a forced case and saturation occurs anyhow.

Ion gyroradius effects

The model presented in Chapter 2 can be extended to include finite ion gyroradius effects. When also finite ion temperature is considered, the vorticity equation is modified. The ion dynamics is described in a small-ρ_i expansion of the ion model in Ref. [14], namely $\omega = \nabla_\perp^2(\phi + \rho_i^2\omega)$, where ω is the ion vorticity and ρ_i the ion gyro-radius. This equation take the place of the definition of ω in Eq. (2.18). In the linearized equations, the ion gyro-radius enters only in combination with ρ_s as $(\rho_s^2 + \rho_i^2)^{1/2}$.

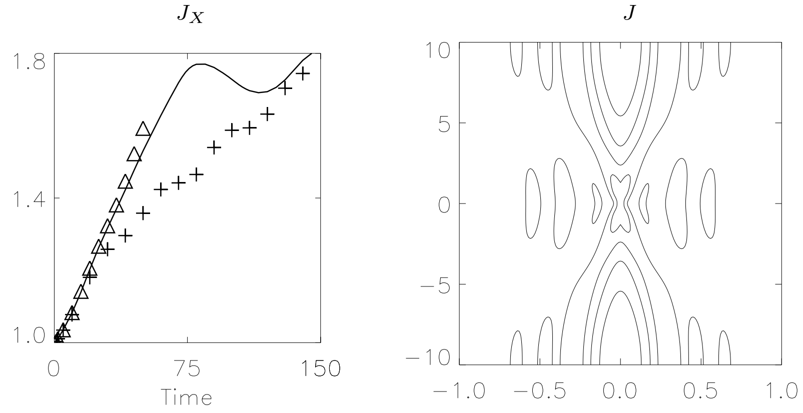

Figure 4.20: Time evolution current maximum for $d_e = 0.18$, $\rho_s^2 = \frac{2}{3}d_e^2$, $\rho_i^2 = \frac{1}{3}d_e^2$, $\nu_i = 10^{-5}$ (triangles). Also the cases $d_e = \rho_s = 0.18$, $\rho_i = 0$ (continuous line) and $d_e = 0.18$, $\rho_s = \rho_i = 0$ (crosses) are shown. Right: isolines of the current density J at $t = 55$

Here the numerical results for $d_e = 0.18$, $\rho_s^2 = \frac{2}{3}d_e^2$, and $\rho_i^2 = \frac{1}{3}d_e^2$ are presented. Again, the only dissipative term included is ion viscosity, $\nu_i = 10^{-5}$ but $\eta = 0$. The values of ρ_s and ρ_i are chosen in order to verify the aforementioned

linear property.
In Fig. 4.20 the time evolution of the current maximum is shown for values of d_e and $(\rho_s^2 + \rho_i^2)^{1/2}$ that are the same as d_e and ρ_s in Fig. 4.16. The current distribution, Fig. 4.20, is rather similar to the case $\rho_i = 0$. In the limited time interval in Fig. 4.20 the evolution of the current maximum cases with and without ρ_i are largely the same.
The term $\rho_i^2 \nabla^2 \omega$ is expected become important when small scales in the vorticity are formed. Numerical instabilities prevented us to reach that point.
Ion gyro-radius effects for an unstable configuration are presented in [39].

4.2.3 Asymmetric forcing

In the cases examined till now the forcing was perfectly symmetric, see Eq. (4.1). The wall modulation on one side of the slab was the mirror image of the modulation on the other side. In order to study the reconnection process under more generic conditions, this symmetry of the boundary conditions is broken. In particular, the question whether structures like the current spike described in Section 4.2.2 (and extensively analyzed in Section 4.3) are intrinsic to Hamiltonian dynamics or just the result of symmetry is of interest.

The result presented in this section have been obtained changing only the forcing. All the other parameters are the same as in the case $\rho_s = d_e = 0.18$ of Section 4.2.2. On the boundary at $x = L_x$ the forcing is the $m = 1$ mode described in Eq. (4.1) with amplitude $\delta_{m=1} = \delta_{wall}$. On the other boundary $x = -L_x$ an $m = 2$ mode (with the same temporal dependence and amplitude) is applied with $\delta_{m=2} = -\delta_{wall}$.

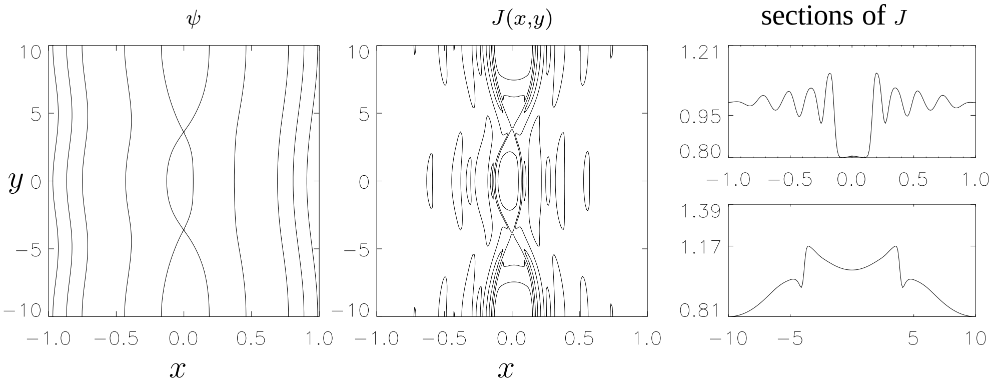

Figure 4.21: Isolines of the magnetic flux ψ, and of the current density $J(x, y)$; top and bottom: current density on sections along $x = 0$ and $y = 0$, at $t = 110$, for $d_e = \rho_s = 0.18$ in the asymmetric case

The difference in the walls modulation is evident in the isolines of ψ shown in

Fig. 4.21. As a consequence of the $m = 2$ modulation, two X points and three O points are formed. This forcing scheme avoids the overlapping of strongly compressed isolines of the generalized fluxes in a same region in space.

In Fig. 4.21 a contour plot and profiles of the current density at $t = 110$ is shown. No current spike with width much smaller than d_e and ρ_s is formed. The current density profiles between the X points shown by the sections of J along $x = 0, y = 0$ presents rather steep gradients, but no scale collapse is taking place.

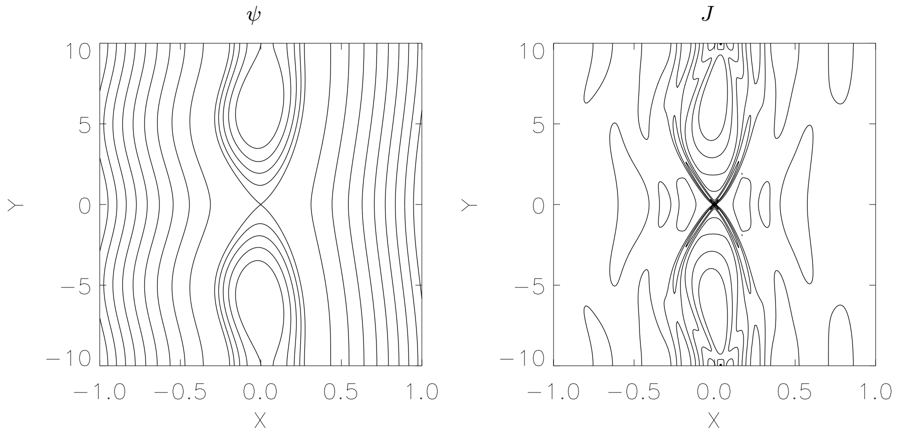

Figure 4.22: Isolines of the magnetic flux ψ, and of the current density J, in a case of symmetric forcing with $\delta_{m=1} = \delta_{m=2}$ at $t = 60$

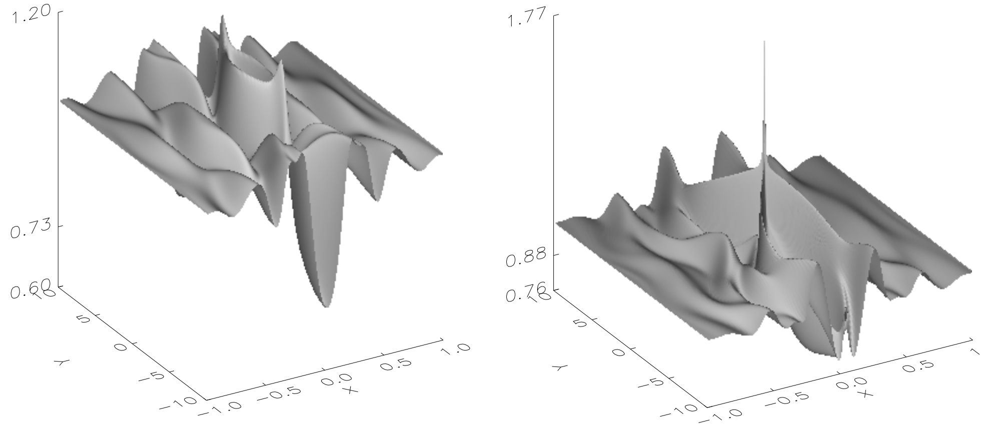

Figure 4.23: Surface plots of J for forcing with unequal m in case of $\delta_{m=1} = -\delta_{m=2}$ (left) and $\delta_{m=1} = \delta_{m=2}$ (right) , at $t = 60$

As a test for the above result the same forcing scheme can be modified in order to restore the overlapping of strong gradients in $G_{\pm}$. Figure 4.22 reports the case of a forcing with the same mode numbers on the two forcing sides as Fig. 4.21 but with $\delta_{m=1} = \delta_{m=2} = \delta_{wall}$. In this case three X points and two O points are formed. Again, the X points in $x = 0$, $y = \pm L_y$ are equivalent due to periodicity. The symmetry restores the overlapping of strong gradients in the generalized fluxes close to $x = y = 0$, and a spike in the current density is again formed.
The surface plots of the current density in the two cases of forcing here exposed is shown in Fig. 4.23. The absence of the current spike in does not prevent the island saturation. As an indication of the time evolution of reconnection Fig. (4.24) reports the flux in the O point, located at $x = 0$, $y = \pm L_y$ of the configuration of Fig. 4.21. This flux is an indicator for the time evolution of reconnected flux. Saturation and subsequent oscillatory phase are evident. Thus the characteristics

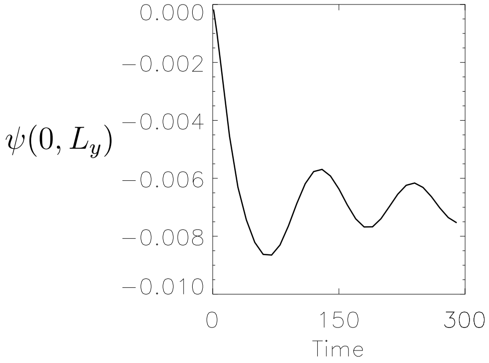

Figure 4.24: Time evolution of the magnetic flux in the O point in $x = 0$, $y = \pm L_y$

of the Hamiltonian reconnection studied in the case of identical forcing on the two sides of the box are found in this case too, but without the formation of thin peaks in correspondence of the X points.

In conclusion the thin current spike formation is a consequence of the superposition of strong gradients in the generalized fluxes in a same region of space, due to symmetry of the excitations. When the superposition is avoided the saturation can be reached without the presence of thin peaks in the current density.

4.3 Collisionless reconnection in instabilities and due to external forcing

Abstract Collisionless magnetic reconnection due to electron inertia is numerically investigated in two-dimensional, externally forced systems and unstable configurations. A common characteristic of reconnection in the two cases, associated with the effects of electron inertia and temperature, is a faster than exponential scale collapse. This collapse creates structures that are much narrower than the inertial reconnection layer, such as a very localized, X-shaped current distribution. The nonlinear evolution at this small scale is largely independent of large scale features such as the initial and boundary conditions which constitute the differences between driven and unstable cases. However, only in forced reconnection cases ion viscosity is found to stop the scale collapse of the current. High numerical resolution made the detailed investigation of small scale structure formation and continued scale collapse possible.

by[1] G. Valori, D. Grasso†, H.J. de Blank

† Energetics Dept., Politecnico di Torino and Istituto Nazionale Fisica della Materia, Italy

---

[1] This section was published as the article [40]. Limited to this section only, the words “Hamiltonian” and “collisionless” are considered as synonymous, contrary to the convention that applies to the rest of the thesis as explained in Section 1

4.3.1 Introduction

Collisionless magnetic reconnection has been studied for many years, starting with investigations into earth magneto-tail dynamics (see for example Ref. [7] and references therein). In the last decade it has been invoked to account for fast magnetic field changes during internal disruptions in high temperature, magnetically confined plasmas [6], [41]. Nowadays, the process of fast magnetic topology rearrangement on scale lengths comparable with the electron inertial skin depth, $d_e = c/\omega_{pe}$, is being interpreted in terms of Hamiltonian reconnection [15]. Indeed, the system of equations, which describes the effect of electron inertia on magnetic flow, has a Hamiltonian structure [14]. The effect of parallel electron compressibility can be included in the Hamiltonian model. The ions respond so as to maintain quasineutrality by moving transversely over a length that represents a new scale in the model: the ion gyroradius at the electron temperature or ”ion sound gyroradius”, $\rho_s = \rho_i\sqrt{T_e/T_i}$. Several studies in the two-dimensional case were focused on unstable systems, see for example [37].

In the Hamiltonian reconnection the decoupling of the plasma motion from the magnetic field lines motion is allowed by the electron skin depth, and the magnetic island has a typical size on scale lengths comparable with d_e. This will be regarded in the following as a large scale. The spatial structure inside the reconnection layer found in these cases is a cross shape in the current and vorticity distributions, with the angle of the cross being determined by the ratio between the two scale lengths in the equations, ρ_s and d_e [42]. These current density and vorticity layers become ever narrower, their length scales become small, dropping well below ρ_s and d_e, and will be regarded as small scales.

In this paper nonlinear regimes in collisionless reconnection are studied in different configurations, using two-dimensional reduced two-fluid equations. First, we analyze reconnection due to external forcing, considering a plasma embedded between flux conserving walls, initially in a stable equilibrium configuration with a constant current density. The neutral line of the magnetic field is centered between the walls. The system is perturbed by means of a brief displacement of the walls that excites Alfvén waves inside the plasma. This configuration is known in the literature as Taylor’s problem, and has been studied, for instance, for the reduced magneto–hydrodynamic (RMHD) [20], [21] and the electron magneto–hydrodynamic [43] models. Second, we analyze reconnection occuring in instabilities, considering an unstable equilibrium and perturbing it with an eigenmode of the linearized set of equations. Hereafter we will refer to these two different configurations as the **forced** and **unstable** cases, respectively.

The analysis we carried out is concerned with the plasma behavior on small and large scales. The comparison between the forced and the unstable configurations shows that the final magnetic topology near the neutral line obtained in the two cases is the same, despite the differences in the initial excitations, but in the forced case, as in the RMHD case, the reconnected flux is found to reach a saturation level. On the contrary, in the unstable case, there is no mechanism which can stop the growth of the magnetic island, and reconnection can proceed till the island size is of the order of the equilibrium magnetic field scale length. In addition the scale collapse occuring in the vorticity and current density layers presents the same behavior over several orders of magnitude, without any substantial dependencies on the way in which the system is initially excited, *i.e.* on the large scale behavior. Only at a later stage the gradients associated with variations of vorticity and current density inside the layers are found to collapse at exponential growth rate in the forced case, and more than exponential in the unstable case.

The effect of ion viscosity is also investigated. In the forced case, ion viscosity connects the large and small scale dynamics, leading to the removal of the collapse.

The paper is organized as follow: in Section 2 the set of equations describing the model are reported; in Section 3 the physical models for the numerical simulations are presented; the global reconnection process is described in Section 4, while the small scale formation process in Section 5; in Section 6 the conclusions are presented.

4.3.2 The model.

The reduced two-fluid model of Ref. [14] is used. Here, its contents is briefly summarized. The RMHD model in Ref. [20], [21] is extended in order to include electron inertia and finite ion sound gyroradius effect in Ohm's law. Electron inertia, instead of resistivity, is responsible for magnetic field topology changes. In all the cases of interest for tokamak plasmas, d_e is much smaller than the minor radius, and smaller than ρ_s. In this limit, where toroidal curvature and compressional Alfvén waves are neglected, a simple representation of the magnetic field can be adopted. Thus, introducing the magnetic flux ψ and electric potential ϕ, the electromagnetic field can be described by

$$\mathbf{B} = B_0(\mathbf{e}_z + \mathbf{e}_z \times \nabla\psi), \qquad \mathbf{E} = \frac{B_0}{c}(-\nabla\phi + \mathbf{e}_z\partial_t\psi),$$

where $\mathbf{e}_z$ is the unit vector in the z direction. Assuming the toroidal coordinate z to be ignorable, the model describes a reduced, 2D, configuration. In a strongly magnetized, low-β plasma, when the perturbation scale-length perpendicular to the magnetic field is much smaller than the parallel one, the electron fluid velocity for small density perturbations is given by

$$\mathbf{v} = \mathbf{e}_z \times \left(\nabla\phi - \frac{c}{enB_0}\nabla(nT)\right) + v_z\mathbf{B}/B_0, \tag{4.9}$$

where the terms in parenthesis are the $E \times B$ and the diamagnetic drifts, and the last term is the velocity parallel to the magnetic field. Dissipative terms and the polarization drift are of higher order here. The cold ion limit is assumed: in this case the density perturbations are related to the electric potential as $\ln n/n_0 = \Omega_i^{-1}\omega$, where Ω_i is the ion gyrofrequency, and $\omega \equiv \nabla_\perp^2\phi$ the ion vorticity. This relation is a solution to the time-dependent ion vorticity equation and it will continue to hold after it has been satisfied by the initial conditions. The quasi-neutrality condition couples the ion density perturbations with the electron compressibility in the parallel motion, leading to the reduced system of equations

$$\partial_t\omega + [\phi,\omega] - v_A^2\,[\psi, J] = \nu_i\nabla_\perp^2\omega, \tag{4.10}$$

$$\partial_t\psi + \left[\phi - \rho_s^2\omega, \psi\right] = d_e^2\left(\partial_t J + [\phi, J]\right), \tag{4.11}$$

$$\omega = \nabla_\perp^2\phi, \qquad J = \nabla_\perp^2\psi, \tag{4.12}$$

where $v_A \equiv B_0(4\pi n m_i)^{-1/2}$ is the Alfvén velocity, ν_i is the ion viscosity, and $[F, G] = \mathbf{e}_z \cdot (\nabla F \times \nabla G)$ is the perpendicular Jacobian. The current density and the magnetic flux are related by the Ampère law $J \equiv -(4\pi e/cB_0)nv_z = \nabla_\perp^2\psi$.
In the limit $d_e \to 0$, Eq. (4.11) expresses a frozen-in law for magnetic flux, *i.e.* the magnetic field lines are passively advected by the stream function $\phi - \rho_s^2\omega$ and no reconnection takes place.
Neglecting ion viscosity, the Hamiltonian structure of Eqs.(4.10–4.12) can be revealed. The two fluxes $G_\pm \equiv \psi - d_e^2 J \pm \rho_s d_e\omega/v_A$ are passively driven by the flow fields of the stream functions $\Phi_\pm \equiv \phi - \rho_s^2\omega \pm v_A\rho_s d_e J$,

$$\partial_t G_\pm + [\Phi_\pm, G_\pm] = 0. \tag{4.13}$$

The reconnection mechanism of the magnetic field lines can be interpreted as an exchange between magnetic and kinetic energy that conserves the generalized fluxes $G_\pm$. Equations (4.13) and their conservation properties [14] are extensively analyzed elsewhere [15], [42], [13] and briefly commented upon in Section 4.
The cold electron limit, obtained from Eqs.(4.10–4.12) for vanishing ρ_s, has been studied in [44]. Moreover, neglecting electron inertia and including resistivity, corresponds to the well known RMHD case, whose linear Taylor's problem was analytically treated in Ref. [20]. The nonlinear regime was investigated numerically in Ref. [21].

4.3.3 Numerical calculations.

The vectorized code [36] used to obtain all the numerical results presented here employs a 2^{nd} order finite-difference method, is implicit in time, and permits adaptive, local uniform grid refinement. The high resolution provided by the adaptive grid refinement technique is needed in order to resolve small scale structures that

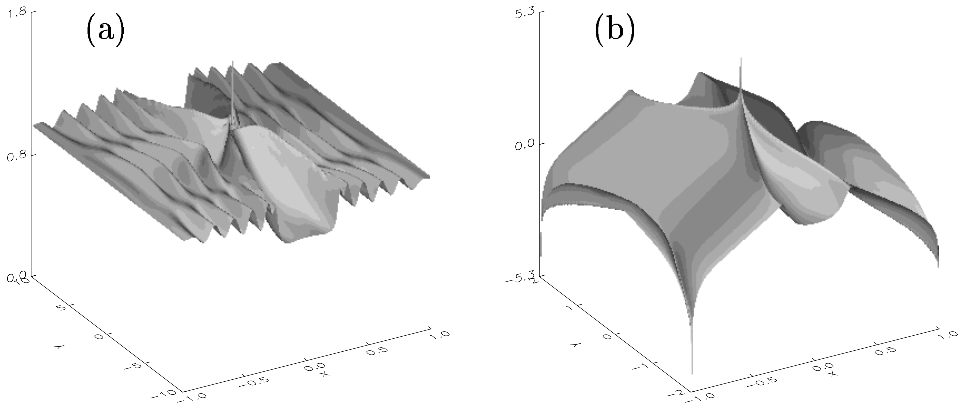

Figure 4.25: Surface plots of the current density in the (a) forced case, at $t = 135\,\tau_A$, with $\nu_i = 10^{-5}$; (b) unstable case, at $t = 78\,\tau_A$, with $\nu_i = 6\,10^{-5}$. The x and y coordinates are normalized to L_x.

appear in the late non-linear stage of the reconnection process. The unstable case as presented below has already been investigated with a 4^{th} order, finite difference, explicit code with nonuniform grid [42], and fully agreement between the two simulation results has been verified.

In both the forced and the unstable cases, ψ and J have even parity, while ϕ and ω are odd, so the numerical simulations are restricted to the first quadrant of the entire visualization domain, defined by $(-L_x \leq x \leq L_x, -L_y \leq y \leq L_y)$. Time is normalized to the Alfvén time. The numerical results presented below are obtained using the following parameters:

forced case: the equilibrium configuration ($\psi_0 = \frac{1}{2}x^2$, $J_0 = 1, \phi_0 = \omega_0 = 0$) is stable with a neutral line in $x = 0$. The system is initially excited via a displacement of a flux conserving wall at $x = \pm L_x$, given by $x = \pm L_x \mp \delta_{wall} \cos(\pi y/L_y) \tanh(t/\tau_{wall})$. The motion $dx/dt = v(y,t)$ of the walls is modeled on a fixed rectangular domain by imposing the boundary condition $\phi(y,t) = \int v(y,t)dy$ at $x = L_x$. On the moving boundary $\omega = 0$, $\partial J/\partial x = 0$ are imposed, while on the remaining three boundaries symmetry constrains are used. The domain is periodic in the y direction, and the adopted physical parameters are $L_x = 1$, $L_y = 10$, $\rho_s = d_e = 0.18\,L_x$, $\delta_{wall} = 0.04$, $\tau_{wall} = 10$. The computational domain is covered with a (100×200) grid; 9 levels of grid refinement are used, so the minimum size of the grid cells is: $\Delta x = 3.9\,10^{-5} = 2.2\,10^{-4}\,d_e$, $\Delta y = 5\,\Delta x$.

unstable case: the equilibrium configuration ($\psi_0 = -\cos x$, $J_0 = \cos x$, $\phi_0 = \omega_0 = 0$), has two neutral lines at $x = 0$ and $x = \pm L_x$. An $m = 1$ tearing unstable mode in the cold electron limit is excited in the system, according to [44]: $\delta J = J_\infty \cos[\sqrt{1-k^2}(|x| - \pi/2)]) \cos ky$ outside the reconnection region, and $\delta J = J_\infty d_e^{-1}\sqrt{2/\pi}\exp(-x^2/2d_e^2)\cos ky$ inside, with J_∞ a constant. The domain is periodic in the x and y directions, and the adopted physical parameters are $L_x = \pi$, $L_y = 2\pi$, $k = \pi/L_y$, $\rho_s = d_e = 0.08 L_x$. The computational domain is covered with a (200×200) grid; 10 levels of grid refinement are used, symmetrically placed around the two opposite X-points, so the area around each of them is covered with cells of minimum grid size $\Delta x = 3.1\,10^{-5} = 1.2\,10^{-4}\,d_e$, $\Delta y = 2\,\Delta x$.

In the first case the drive for the reconnection process is a displacement of the walls that last for a finite period of time of the order of τ_{wall}, after which the walls are fixed in the new position. In the unstable case the reconnection is triggered by a linear mode known to be unstable for the cold electron limit of Eqs.(4.10–4.12). An example of the typical current density configurations in the two cases in a late stage of the reconnection process is given in Fig. 4.25.

4.3.4 Large-scale behavior.

In Fig. 4.26 the iso-lines of the fields ψ, ϕ, ω, J, G_+, and Φ_+ at $t = 70\,\tau_A$ in the forced case are presented. Here the large scale structure of the fields are shown at a time well after the walls have come to a rest. The wall displacement generates Alfvén waves that move towards the neutral line and drive the reconnection process, as shown in Fig. 4.25 (a). The Alfvén wave nature of the initial excitation can be recognized in the vorticity patches of alternate signs, in the stream function ϕ and in the current density shown in Fig. 4.26 (a-c). The current density and the vorticity, that were initially largest in the reconnection layer of width d_e around the X-point, subsequently both concentrate in two narrow layers which intersect each other in the X-point. The current and the vorticity remain localized in the same layers during the simulation.

The Alfvén waves that characterize the first stage consist of convection cells that are larger than d_e and ρ_s, resembling the macroscopic cells of the so-called “large Δ' regime” in linear instabilities corresponding to $\Delta' d_e \gg 1$, Δ' being the jump of the logarithmic x–derivative of ψ across the reconnection layer [5]. On the basis of this behavior of the convection cells, a comparison with the unstable case is possible despite different excitation methods and equilibria. Linear ideal MHD analyses based on the equilibrium parameters given in the previous section provide a measure of tearing mode stability: $\Delta' = 8$ and $\Delta' d_e = 2$ in the unstable case, $\Delta' = -2$ and $\Delta' d_e = -0.4$ for modes on the stable equilibrium of the

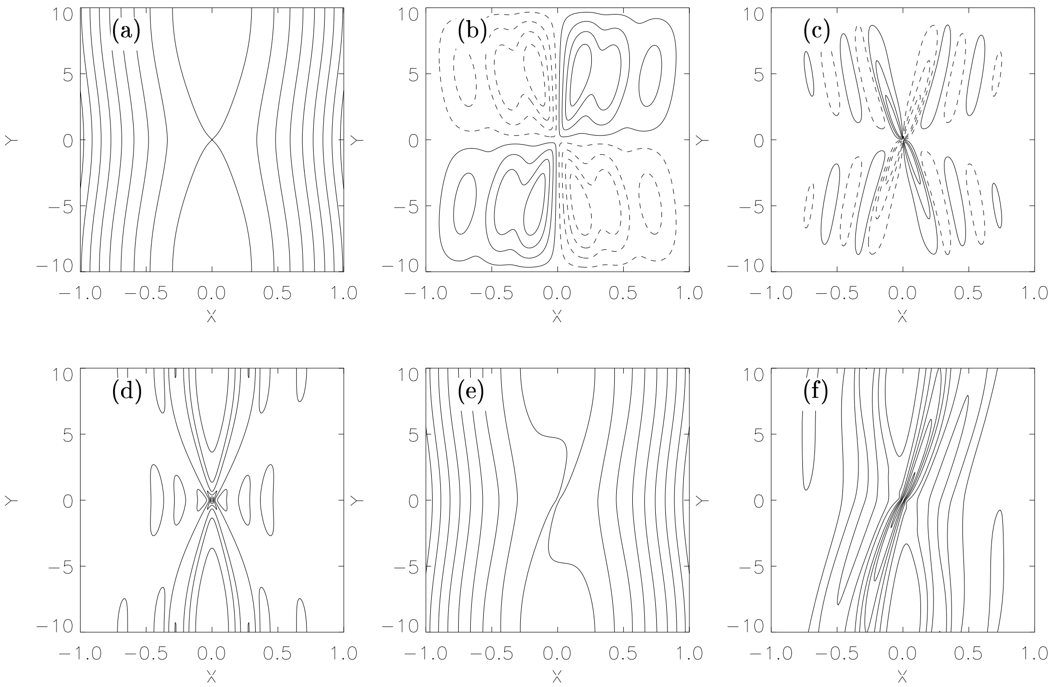

Figure 4.26: Forced case: iso-lines of the fields (a) ψ; (b) ϕ; (c) ω; (d) J; (e) G_+; (f) Φ_+, at $t = 70\,\tau_A$, for $d_e = \rho_s = 0.18$, with $\nu_i = 10^{-5}$.

forced case after the forcing phase. On the other hand the analysis of the early large–scale behaviour of $\psi(x, y, t)$ in the forced case yields an effective $\Delta' = 7.8$. The dynamical evolution of the reconnection process is here described by the growth rate of the magnetic island half width $w(t)$ and by the total reconnected flux $\delta\Psi(t)$, defined as the difference between the magnetic fluxes in the X and O points, $\delta\Psi \equiv \psi(0, 0) - \psi(0, L_y)$. Indeed, the early island growth rates in the forced and unstable cases (Fig. 4.27 (a)) are comparable. It should be noted that $\Delta'(t)$ in the forced case steadily decreases, which reflects the fact that the island size in the forced case grows slower than exponential. The linear analysis also shows that the time scale at which the forcing takes place is much shorter than the period of the eigenmode of the stable equilibrium. However, the linear phase is short-lived, as Fig. 4.27 (a) shows, because the width w quickly exceeds d_e.

At $t = 82\,\tau_A$, a maximum of the island width $w(t)$ is reached in the forced case (Fig. 4.27 (a)). Due to the symmetry properties of the fields, Eq. (4.11) implies that the value of $\psi - d_e^2 J$ in the X-point is constant in time, so when the island size reaches its maximum also the current density in the X-point and $\delta\Psi$ stop growing. The island width saturation is mainly caused by the vicinity of the walls, as energy considerations show. A well–defined amount of energy is added to the system by

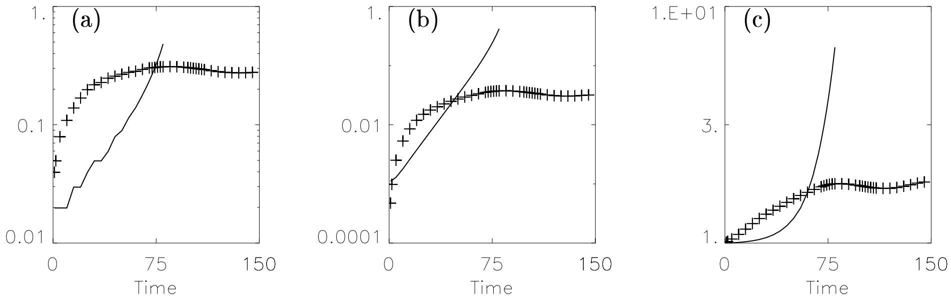

Figure 4.27: Time evolution of (a) the halfwidth of the island w normalized to L_x; (b) the total reconnected flux $\delta\Psi$; (c) the current density J in the X-point $(x = 0, y = 0)$, in the unstable (continuous line) and forced (crosses) cases.

the initial wall perturbations. If we assume that all this energy is converted into the magnetic energy of a single island structure, one finds a maximal half-width $w = 0.44$, which is not much larger than the numerically found maximal value $w = 0.30$. However, in the absence of walls ($\psi_0 = \frac{1}{2}x^2$ on an infinite domain) the same amount of magnetic energy would correspond to an island size $w = 0.85$. The saturation can also be described in terms of the stream function, in our model

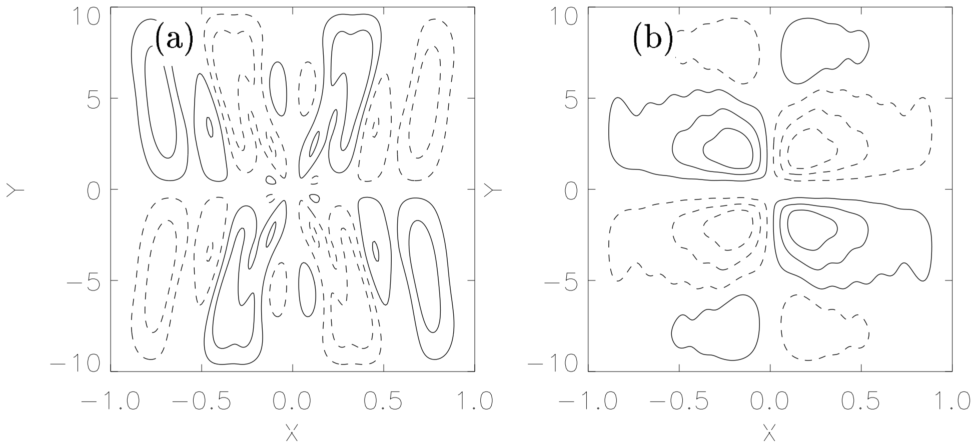

Figure 4.28: Forced case: iso-lines of ϕ at $t = 82\,\tau_A$ and $t = 150\,\tau_A$, with $\nu_i = 10^{-5}$.

proportional to the electric potential [14]. Thus, it is easy to recognize in the macroscopic cell depicted in Fig. 4.26 (b) at $t = 70\,\tau_A$ a monopole structure of the electric potential at $x \geq 0$, $y \geq 0$. In Fig. 4.28 two later time steps ($t = 82\,\tau_A$ and $t = 150\,\tau_A$) of the stream function are shown. When the island approaches saturation, at $t = 82\,\tau_A$ as can be seen in Fig. 4.27 (a), a region of opposite signed vorticity grows inside the island (Fig. 4.28 (a)) until the saturation size is reached. Then the island starts shrinking and, due to the incompressibility of the fluid, a second flow pattern appears inside the separatrix, corresponding to the dipole-like structure of the electric potential shown in Fig. 4.28(b).

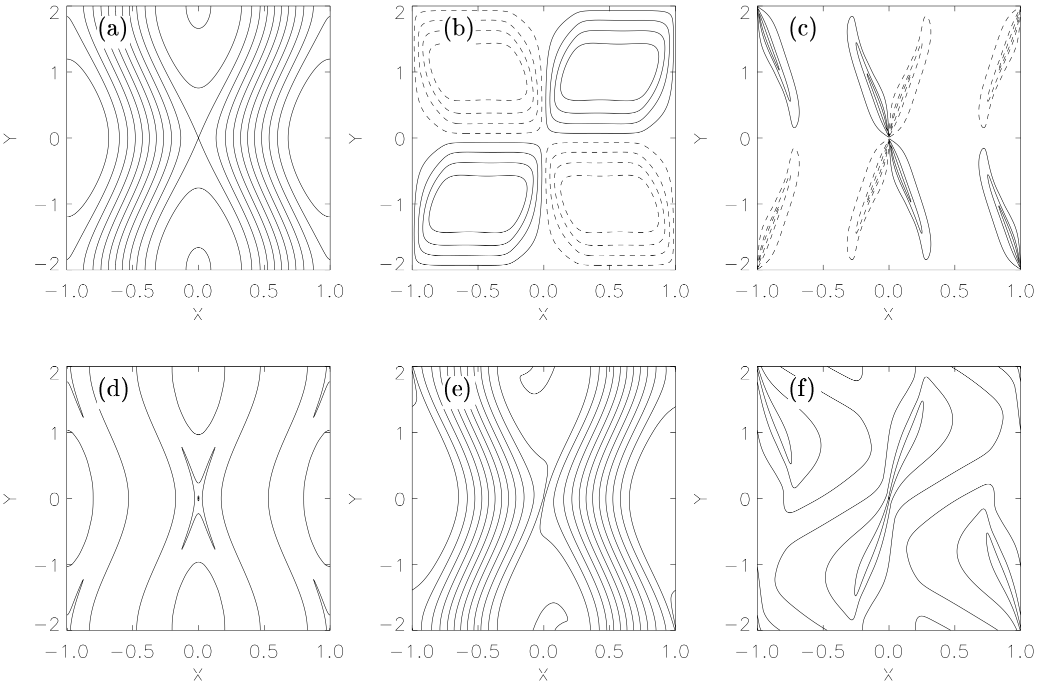

Figure 4.29: Unstable case: iso-lines of the fields (a) ψ; (b) ϕ; (c) ω; (d) J; (e) G_+; (f) Φ_+, at $t = 70\,\tau_A$, for $d_e = \rho_s = 0.08 L_x$, with $\nu_i = 1.6\,10^{-5}$. The x and y coordinates are normalized to L_x.

In Fig. 4.29 the iso-lines of the fields ψ, ϕ, ω, J, G_+, and Φ_+ at $t = 78\,\tau_A$ in the unstable case are presented. The structure of the fields closely resembles the one found in the forced case. These results are in agreement with those obtained with a different code and analyzed in detail in Ref. [42]. We point out that the cross shape structure of both the current density and the vorticity is associated with the conservation properties of the system of equations Eqs (4.10–4.12), as it is shown in Ref. [15], and it constitutes a fingerprint of the inertial reconnection when ion sound gyroradius effects are included. The cross angle is determined by the ratio between the two typical scale lengths into the model equations, ρ_s/d_e.

A difference between the driven and unstable cases can be recognized on the large scale in the dynamical variables w and $\delta\Psi$. As can be seen in Fig. 4.27 (a,b), after an exponential phase in the growth of the magnetic island, a faster than exponential one is entered. Since in the unstable process there is no mechanism that can stop the reconnection process, the magnetic island can growth up to size comparable with the size of the integration domain. Thus, no saturation is present in this case, and no maximum value of the reconnected flux nor of the current density is found.

The large scale behavior is then found to be rather general, leading to the same spatial configurations in both the forced and unstable cases. Nevertheless, the dynamical evolution reflects the characteristics of the different initial configurations.

4.3.5 Scale collapse.

During the reconnection process, small scale structures are formed near the X-point. Here the existing current density peak shrinks with time below any physical scale-length, see Fig. 4.25 (a). Simultaneously, the extrema of the vorticity get closer and closer to the X-point, generating a gradient whose associated scale length get smaller and smaller with time. In this section the investigation of this scale collapse is reported. Ion viscosity effect are also discussed, and some consideration about the regularity of the solution are eventually formulated.
We characterize the scale collapse in the X-point by means of three monitor quantities [34]. The first quantity is the second, mixed, derivative of the vorticity, calculated in the X-point

$$\omega_{11} \equiv \partial_x \partial_y \omega|_X \tag{4.14}$$

which is a measure of the smallest scale length in the vorticity field. The other monitor quantities are the widths of the X-point current peak in the x and y directions,

$$l_x \equiv \sqrt{|J_0/\partial_x^2 J|_X}, \qquad l_y \equiv \sqrt{\left|J_0/\partial_y^2 J\right|_X}. \tag{4.15}$$

In terms of these quantities, a scale collapse means that

$$|\omega_{11}(t)| \longrightarrow \infty, \qquad l_x(t) \longrightarrow 0 \quad or \quad l_y(t) \longrightarrow 0. \tag{4.16}$$

In Fig. 4.30 the time behavior of l_x, l_y, and ω_{11} in the two inviscid cases are shown. In both the forced and the unstable cases a dramatic increase of ω_{11} occurs, its variation spanning several orders of magnitude. Meanwhile, the width of the current peak shrinks well below any physical scale length present in the model, from box-wide down to $10^{-2}\, d_e$. A common behaviour in the driven and unstable cases can be clearly recognized in a range of more than two orders of magnitude for l_x, l_y and eight orders of magnitude for ω_{11}. This correspondence suggests the idea of a scale collapse that does not depend on the way the system is initially excited. The current and the energy contained in the peak are found to be decreasing functions of time in both the forced and unstable cases. In the forced case the monitor quantities in the late stage show an exponential behavior, while in the unstable one a stronger than exponential collapse is found.

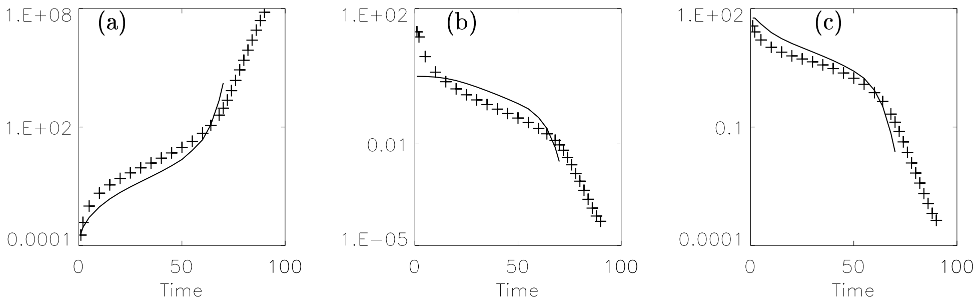

Figure 4.30: Time evolution of (a) ω_{11}; (b) l_x; (c) l_y as defined in Eqs (4.14–4.15), in the unstable (continuous line) and forced (crosses) cases, with $\nu_i = 0$

The questions arise whether the scale collapse will continue forever, and, even more pressing, whether the scale collapse in the X-point can take place in a finite time. It is important to know whether the equations admit finite-time singularities because the existence of such singularities could imply that the conservation properties of $G_\pm$, expressed in Eq. (4.13), do not hold beyond the time of the singularity. In Ref. [35] these questions were addressed, and analytical and numerical indications were presented that finite-time instabilities might indeed be an issue.

Expanding the fields around the X-point in powers of x and y, one can find the general scaling of the fields in the case that a singularity would develop at $t = t_0$. If a finite-time scale collapse would occur,

$$l_x \sim (t_0 - t)^q, \qquad l_y \sim (t_0 - t)^p, \qquad \text{with} \qquad p,\, q < 0, \tag{4.17}$$

then the scalings of the fields and their derivatives are determined by

$$\psi,\, \phi \sim l_x l_y (t_0 - t)^{-1}, \qquad j,\, \omega \sim l_x l_y (t_0 - t)^{-1} \max(l_x^{-2}, l_y^{-2}). \tag{4.18}$$

Hence $\omega_{11} \sim (t_0 - t)^{-1} \max(l_x^{-2}, l_y^{-2})$ monitors the smallest scale length in ω. It is, during a scale collapse, a rapidly increasing function as can be seen in Fig. 4.30 (a).

In order to see if there is numerical evidence for a finite-time singularity, the time-like quantity $\tau_\omega = \omega_{11}^{-1} \max(l_x^{-2}, l_y^{-2})$ was introduced in Ref. [35]. The scaling introduced above gives rise to a linear decrease $\tau_\omega \sim t_0 - t$. Such a decrease was indeed found numerically in Ref. [35]. The numerical results in the present paper follow the scale collapse even further and show that the scaling in Eqs (4.17, 4.18) holds during a hundred-fold shrinking of l_x, but after that a departure from this scaling takes place. Hence there is no compelling numerical evidence for a finite-time singularity.

A closer inspection of Eq. (4.13) and the definitions of $\Phi_\pm$ and $G_\pm$ show that finite time singularities are, in fact, impossible. The proof of this fact, which will be published elsewhere, is based on the proof (reproduced e.g. in Ref. [45]) that the Euler equation of a fluid in two dimensions, $\partial_t \Delta\Phi + [\Phi, \Delta\Phi] = 0$, has no finite time singularities. To prove the regularity of the flow given by Eq. (4.13), the similarity of its form with the 2-D Euler equation is not sufficient. In addition, one needs to show that the Green's functions that express the stream functions $\Phi_\pm$ in terms of the fluxes $G_\pm$ have at most logarithmic singularities, just as in the case of the 2-D Euler equation. This property of the Green's functions can be easily proven. In effect, these Green's functions are given in Ref. [18], where a point-vortex model for Eq. (4.13) is developed. In this paper, the fields $G_\pm$ are sums of δ-functions (the point-vortices), and the corresponding stream functions are precisely the Green's functions mentioned above.

The numerical simulations presented above have been repeated with the addition of ion viscosity ($\nu_i = 10^{-5}$ in the forced case and $\nu_i = 6\,10^{-5}$ in the unstable case). For these cases the scale collapse monitor quantities are presented in Fig. (4.31). The forced case has already been extensively analyzed elsewhere [34]. When ion viscosity is present, the vorticity gradient steepening is much less explosive than in the ideal case: ω_{11} is limited in value and, when the island growth stops (that occurs at $t = 82\,\tau_A$, see Fig. 4.27), its slope is reversed. While this has no effect in the inviscid case, in presence of ion viscosity the island width saturation leads to the scale collapse removal. The oscillatory regime that ω_{11} shows between $t = 98\,\tau_A$ and $t = 106\,\tau_A$ is connected with an interaction between a positive vorticity pattern created inside the island by its saturation, and the vorticity pattern at the separatrix. An analogous behavior can be observed in

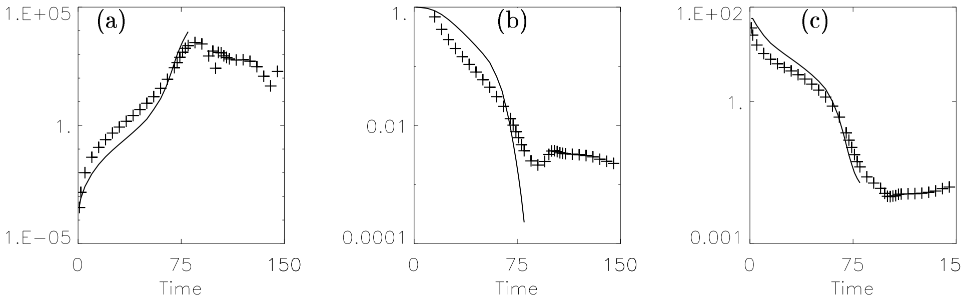

Figure 4.31: Time evolution of (a) ω_{11}; (b) l_x; (c) l_y as defined in Eqs (4.14–4.15), in the unstable (continuous line, $\nu_i = 6\,10^{-5}$) and forced (crosses, $\nu_i = 10^{-5}$) cases.

the current peak, although delayed in time. The collapse of l_x, l_y is stopped around $t = 90\,\tau_A$, as a consequence of the small scale dynamics allowed by ion viscosity and initially generated by the island growth saturation. It has to be remarked again that this does not happen in the absence of ion viscosity: ion viscosity connects small and large scale processes.

In the viscous case, a different behavior of all the monitor quantities is found in the unstable case: the inversion of the ω_{11} slope and the stop of the current scale length collapse is not present, and scale collapse appears in this case to be only slightly slowed down by viscosity. In the cold electron limit it is analytically proved [44] that the time scale associated with the small scale formation is exponentially related with the island width. Numerical simulations [42] show that a similar functional dependence also holds for nonzero electron temperature. Because the island width in the unstable case shows a more than exponential growth which is not affected by ion viscosity, the scale collapse takes place on a time scale that is more and more shorter than the viscous one. Hence, ion viscosity cannot stop the collapse in the unstable case.

The creation of sub-layer scales, below the physical scale lengths present in the model is a characteristic of the analyzed set of equations, and a faster than exponential scale collapse characterized both the forced and unstable cases. Differences in the late behavior, as well as in the ion viscosity effect, can be understood in terms of the way in which the system is initially excited. In particular, in presence of ion viscosity, the late non linear stage of the scale collapse process is dominated by diffusion in the forced case but not in the unstable one.

4.3.6 Discussion and conclusions.

Collisionless reconnection has been numerically investigated using reduced two-fluid equations in two-dimensional domains. In this paper we have presented comparisons between cases where a stable plasma slab between conducting walls is excited by briefly moving those walls, and cases where an instability of the initial configuration occurs. In both cases a magnetic island is formed with the current initially distributed in a layer of width d_e around the X-point, electron inertia being responsible for the reconnection process. The initial rate of island growth is in agreement with linear theory in both situations. Generally the island continues to grow beyond the reconnection layer width. From about 60 Alfvén times onward, both cases enter a strongly nonlinear regime where a further scale length collapse in the vorticity and current density takes place. Due to the coupling between the electron parallel compression and the ion vorticity (associated with the length scale ρ_s), the vorticity and current are concentrated in narrow x-shaped channels around the magnetic X-point [15]. Huge gradients arise, with length scales dropping two orders of magnitude below the smallest characteristic scales of the system (d_e and ρ_s) and below the range of validity of the model. A main result of this paper is that during part (up to two orders of magnitude) of this collapse, the small-scale motion appears to be independent of the large scale differences between the unstable and driven cases. Remarkably, the behaviour of the vorticity, the current density and their derivatives suggest that a self-similar finite-time collapse is taking place. As has been shown in Refs. [34] and [35], the numerically observed scaling agrees, in an expansion of the fields around the X-point, with a finite-time singularity. However, the generalized flux conservation properties of the two-fluid equations are such that on a bounded domain such singularities are prohibited. Indeed, when the scale length collapse is followed even further numerically, deviations from a finite-time collapse become evident. In the forced cases the collapse slows down to a simple exponential time-behaviour. In the unstable cases the scale collapse always continues faster than exponentially in time, even if ion viscosity is added to the model. This reflects what happens at the large scale: the island continues to grow.

In the forced reconnection cases the large-scale situation is different. The system is initially excited by injecting a finite amount of energy into a stable system. Moreover, the motion is restricted by the two flux conserving walls. Hence, in about 80 Alfvén times, the island size reaches a maximum. The final island width saturation is even preceded by a slight decrease. Associated with this reversed motion is the appearance of new vortices of reversed sign near the X-point. In the inviscid model this has no consequence for the small-scale collapse, but in the presence of a small amount of ion viscosity the scale-length collapse is halted and the near-singular vorticity distribution is smoothed out. The sub-scale structure in the current, however, persists indefinitely.

Acknowledgments

The authors are pleased to thank F. Califano, M. Ottaviani, F. Pegoraro, F. Porcelli, J. Rem and T.J. Schep for fruitful discussions.
This work was performed under the Euratom-FOM Association agreement with financial support from NWO and Euratom.

Part Two: Kinetic Theory

5. The kinetic model for drift-Alfvén perturbations

In this section the kinetic extension to the model used in the first part of this thesis is derived. Using the drift-Alfvén ordering employed in Chapter 2 except for the assumption of an isothermal plasma, the kinetic extension is derived from the drift kinetic equation [46]. The fluid model of Section 2.2 is recovered by taking moments of the kinetic equation and assuming an isothermal energy equation.

The kinetic drift-Alfvén equation is simplified by using the conservation of the parallel momentum insured by the strong background magnetic field. In this way the kinetic equation takes a Lagrangian form.

Applications of the kinetic model to steady state reconnection and wave particle effects in the presence of a finite size magnetic island chain are presented in Chapter 6 and 7, respectively.

5.1 Introduction

As discussed in Chapter 1, in strongly magnetized plasmas the electron motion is, to first approximation, a free streaming along field lines which levels off fluctuations in the direction parallel to the magnetic field. Magnetic reconnection merges field lines which extend through regions of space that can be far apart and, in the presence of temperature gradients, have different temperatures. Then the topology change due to reconnection can result in a merging of field lines where streaming electrons have different energies. The relation between such a process and reconnection, and its consequences on particle and energy fluxes are the subject of the second part of this thesis.

If temperature gradients are included in the description of reconnection processes, then kinetic effects must be also considered. In general, far from the resonant layer the phase velocity of the reconnecting mode is much smaller than the thermal velocity. In this zone the temperature is assumed to be a flux function and a fluid description of the plasma is possible. Close to the resonant layer the phase velocity exceeds the thermal velocity and the equation of state approaches the adiabatic law. Hence the physics close to the neutral surface can be properly described again by a fluid model. Between these two zones, for each value of the electron parallel velocity, a region exists in which the phase velocity of the reconnecting mode and the parallel electron velocity are comparable. Here wave-particle resonance effects have to be considered, making a kinetic description necessary. The averaged effect of these spatially distributed resonances is to form a resonant layer where the mode phase velocity and the electron thermal velocity are comparable.

In this section the extension to the fluid model is derived within the validity of the drift ordering.

5.2 The Drift-Alfvén kinetic model

In this section a kinetic extension of the two fluid model presented in Section 2.2 is derived using the very same ordering except for the isothermal hypotheses. In particular, a kinetic equation for the electron distribution function is derived. The ion response is given by the cold ion limit discussed in Section 2.1.2.
The derivation presented in this section is in part an extension of Ref. [47] to finite electron inertia effects.

We repeat briefly the drift-Alfvén ordering of Section 2.2. We consider a strongly magnetized, low-β plasma, where the perturbation scale-length perpendicular to $\mathbf{B}$ is much smaller than the perturbation scale length in the direction parallel to $\mathbf{B}$. Excluding compressional Alfvén waves, the electro-magnetic fields can be described by $\mathbf{B} = B_0(\mathbf{e}_z + \mathbf{e}_z \times \nabla\psi)$, and $\mathbf{E} = (B_0 c^{-1})(-\nabla\phi + \mathbf{e}_z \partial_t \psi)$, where ψ is the magnetic flux, ϕ is the electric potential, and $\mathbf{e}_z$ is the unit vector in the z-direction. The relevant ordering for the Maxwell-Vlasov system is the drift ordering [46].
The guiding center limit of the Vlasov equation for the electron distribution function $\hat{F} = \hat{F}(\mathbf{x}, V_\|, \mu, t)$ is [48]

$$\frac{\partial \hat{F}}{\partial t} + (\mathbf{v}_E + V_\| \mathbf{b}) \cdot \nabla \hat{F} + \Big(-\mathbf{b} \cdot D_t \mathbf{v}_E + \mu \nabla \cdot \mathbf{b} - \frac{e}{m} E_\| \Big) \frac{\partial \hat{F}}{\partial V_\|} = 0 \quad (5.1)$$

where

$$\mathbf{v}_E = \frac{c}{B_0^2} \mathbf{E} \times \mathbf{B}, \qquad D_t \equiv \partial_t + \mathbf{v}_E \cdot \nabla, \qquad \mathbf{b} \equiv \frac{\mathbf{B}}{|\mathbf{B}|}, \qquad \mu = \frac{V_\perp^2}{2\Omega_e} (5.2)$$

Due to the strong ambient magnetic field B_0 and to the fact that length scales are much longer in the direction of the magnetic field than perpendicular to it, curvature and $\nabla\mathbf{B}$ effects are negligible, hence parallel and perpendicular particle dynamics are decoupled. The magnetic moment μ is an ignorable coordinate. Thus, Eq. (5.2) can be integrated over μ to obtain the equation for the electron distribution function $F(\mathbf{x}, V_\|, t) = \int d\mu \hat{F}(\mathbf{x}, V_\|, \mu, t)$ governing the parallel motion. This equation to leading order is

$$\frac{\partial F}{\partial t} + [\phi, F] + V_\| \mathbf{b} \cdot \nabla F - \frac{e}{m_e} E_\| \frac{\partial F}{\partial V_\|} = 0 \quad (5.3)$$

Using the definitions of $\mathbf{E}$ and $\mathbf{B}$ given above, the Maxwell-Vlasov system then reads

$$D_t F + V_\parallel \nabla_\parallel F = \Omega_e (D_t \psi - \partial_z \phi) \frac{\partial F}{\partial V_\parallel}, \tag{5.4}$$

$$D_t \Big(\Delta\phi - \Omega_i \log n/n_b \Big) = 0, \tag{5.5}$$

$$\Delta\psi = -\frac{4\pi e}{B_0 c} \int dV_\parallel \; V_\parallel F, \tag{5.6}$$

where n_b is a reference value for the density. The ion motion is governed by Eq. (5.5), see Section 2.1.2. Equation (5.6) is the Ampère law for the parallel current $J \equiv -e \int dV_\parallel \; V_\parallel F$.

Equations (5.4–5.6) are the sought kinetic extension of Eqs. (2.16–2.18).

The fluid model of the first part of this thesis can be derived from Eqs. (5.4–5.6). Taking the first two moments of Eq. (5.4) yields directly

$$D_t \ln n = \frac{cB_0}{4\pi e n} \nabla_\parallel J$$
$$D_t(\psi - d_e^2 J) + \frac{1}{\Omega_e n} \nabla_\parallel \int dV_\parallel \; V_\parallel^2 F = \partial_z \phi \tag{5.7}$$

the first of which is already Eq. (2.7). The parallel electron temperature is $T = n^{-1} m_e \int dV_\parallel \; (V_\parallel - v_z)^2 F$, where v_z is the averaged velocity, $v_z = n^{-1} \int dV_\parallel \; V_\parallel F$. Then Eq. (5.7) reduces to the Eq. (2.8) without dissipative and gyroviscous terms. While the absence of dissipative terms is obvious as collisions were not included in Eq. (5.6), the absence of the terms involved in the gyroviscous cancellation is more tricky. The fact is that the terms canceled from Eq. (2.8) are proportional to $\mathbf{e}_z \times \nabla(nT) \cdot \nabla J$, thus they involve the diamagnetic drift velocity, which is not a particle velocity. Consequently, it simply does not occur in the kinetic equation. On the other hand, in the fluid equations when the diamagnetic drift is important than it is so also in the stress tensor, and then the gyroviscous cancellation occurs. We can finally states that Eqs. (5.4-5.6) are a kinetic extension of the two fluid model presented in Section 2.2.

5.3 Lagrangian form

In this section an advective form of Eq. (5.4) is derived. The strong magnetic field constrains the dynamic to be almost two-dimensional. It is then justified to ignore the spatial coordinate along the magnetic field. The consequent conservation of the parallel momentum is then used to simplify further the kinetic equation.

Although it is possible to keep the three spatial dimensions [49], in the following we assume z to be an ignorable coordinate. The parallel momentum $v_\parallel(\mathbf{x}, V_\parallel, t) = V_\parallel + \Omega_e\psi$ is then conserved, so if F is a solution of Eq. (5.4), also $G(F, v_\parallel)$ is a solution. The coordinate transformation from $V_\parallel$ to $v_\parallel$, Eq. (5.4) for the distribution function $\overline{F}(\mathbf{x}, v_\parallel, t) \equiv F(\mathbf{x}, V_\parallel, t)$ yields

$$\partial_t \overline{F} + \left[\phi + \psi v_\parallel - \frac{1}{2}\Omega_e\psi^2, \overline{F}\right] = 0. \tag{5.8}$$

Any arbitrary function of $v_\parallel$, independent of time and space is a solution of Eq. (5.8). We can then assume that the total electron distribution function $\overline{F}$ is split into a constant part f_b describing a static plasma with uniform density n_b, and a small perturbation f which yields small space and time dependent contributions to density and temperature, $\overline{F}(\mathbf{x}, v_\parallel, t) = f_b(v_\parallel) + f(\mathbf{x}, v_\parallel, t)$. The bulk of the plasma carries no current, *i.e.* f_b is taken to be an even function of $v_\parallel$. In this approximation Eqs. (5.4-5.6) become

$$\partial_t f + [\phi + v_\parallel\psi - \frac{1}{2}\Omega_e\psi^2, f] = 0, \tag{5.9}$$

$$D_t\Gamma = 0; \qquad \Gamma \equiv \Delta\phi - \frac{\Omega_i}{n_b}\int dv_\parallel\, f \tag{5.10}$$

$$\Delta\psi - d_e^{-2}\psi = -\frac{4\pi e}{B_0 c}\int dv_\parallel\, (v_\parallel - \Omega_e\psi) f, \tag{5.11}$$

The logarithm in Eq. (5.5) for the electrostatic potential was Taylor expanded because density perturbations are small with respect to n_b.

The above system of equations is closed. Once the solution f to Eq. (5.9) is known the sources on the right hand side of Eqs. (5.10, 5.11) can be obtained by integration.

It can be proved that the system Eqs. (5.9–5.11) has Hamiltonian structure and admits solutions in form of drift-Alfvén vortices, see [49].

In this thesis Eqs. (5.9–5.11) are used to study reconnection across a temperature difference, in Chapter 6 , and the linear stability of a finite size islands chain, in Chapter 7.

6. Reconnection of flux tubes with different temperatures

In this chapter the Maxwell-Vlasov system in the drift-Alfvén approximation, Eqs. (5.9, 5.11), is applied to an X-point magnetic configuration with ongoing reconnection. In particular, the effect of a temperature difference in the inflowing plasma streams in the specific case of a stationarily reconnecting solution is treated. Wave-particle resonances are absent in this time-independent problem. These results were published in [50] and [51].

6.1 The governing equations

We exclude ion drift waves by choosing the solution $\Gamma(t=0)=0$ in Eq. (5.10), as in the fluid case, see Section 2.2. In this approximation Eqs. (5.9, 5.11) become

$$\partial_t f + [\phi + v_\parallel \psi, f] = 0, \tag{6.1}$$

$$\Delta\psi - d_e^{-2}\psi = -\frac{4\pi e}{B_0 c}\int dv_\parallel \, v_\parallel f, \tag{6.2}$$

$$\Delta\phi = \frac{\Omega_i}{n_b}\int dv_\parallel \, f, \tag{6.3}$$

where only terms up to the first order in ψ have been retained. The above system of equations is closed. Once the solution f to Eq. (6.1) is known the sources on the right hand side of Eqs. (6.2, 6.3) can be obtained by integration. In this chapter we will restrict to the time-independent problem: $\partial_t f = 0$ in Eq. (6.1).

6.2 Steady state reconnection.

We want to study the effect of spatial temperature and density variations of the inflowing plasma in a stationarily reconnecting solution of Eqs. (6.1–6.3). In order to have explicit expressions we seek an approximate solution in terms of density and temperature differences, although the method presented below can be used for arbitrary distribution functions. First, a reconnecting solution ϕ, ψ to Eqs. (6.2, 6.3) with vanishing sources ($f = 0$) will be considered. The effect of density and temperature differences will be then introduced as a small perturbation in the distribution function ($f \neq 0$). Subsequently, the effects of this perturbation on the solutions ϕ, ψ will be discussed.

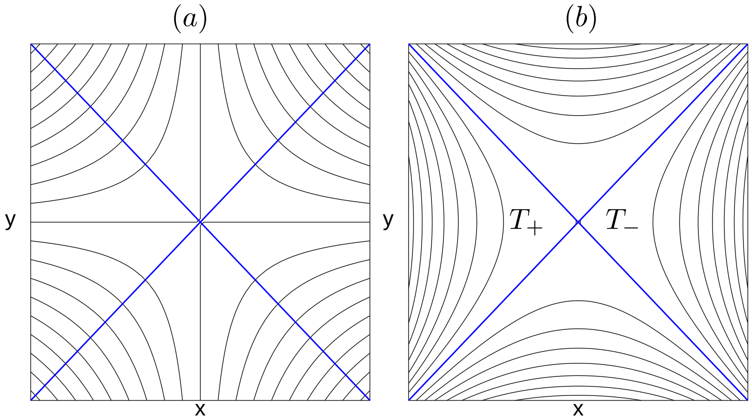

Figure 6.1: Zeroth order fields ϕ (a) and ψ (b) given in Eqs. (6.4)

Taking $f = 0$ to leading order, Eqs. (6.2, 6.3) reduce to $\Delta\phi = 0$ and $\Delta\psi = d_e^{-2}\psi$. A particular solution for the stationary flux and electric potential is given, in polar coordinates $\theta = \arctan(y/x)$, $r = (x^2 + y^2)^{1/2}$, by

$$\psi = J_0 I_2(r/d_e)\cos(2\theta), \qquad \phi = \omega_0 r^2 \sin(2\theta), \tag{6.4}$$

where J_0, ω_0 are arbitrary constants and I_2 is the modified Bessel function of the second order. This solution is shown in Fig. 6.1 for d_e equal to one fifth of the domain, and describes a simple X point configuration with ongoing reconnection.

For the sake of clarity, let us concentrate on temperature perturbations. We consider the inflowing plasma on the left to be described by a constant distribution function f_+ with temperature T_+, and different from the temperature T_- of the inflowing plasma on the right described by a constant distribution function f_-.
The first question we want to answer is: what is the form of the perturbed velocity distribution function in the plasma flowing away from the X point?
The stationary drift kinetic equation has solutions $f = f(\phi + v_\parallel\psi)$. For the most general solutions, the functional dependence $f(\phi + v_\parallel\psi)$ must be allowed to change across separatrices, *i.e.*, contours $\phi + v_\parallel\psi =$ constant through a singular point where $\nabla(\phi + v_\parallel\psi) = 0$. Note that the particle trajectories $\phi + v_\parallel\psi =$ constant, and the separatrices $\phi + v_\parallel\psi = 0$, depend on $v_\parallel$. In Fig. 6.2, particle trajectories for three values of $v_\parallel$ are shown. The particle trajectories coincide with the ψ isolines (Fig. 6.1b) for $v_\parallel = -\infty$. With increasing $v_\parallel$, they shift until they coincide with the isolines of ϕ (Fig. 6.1a) for $v_\parallel = 0$, and again to the ψ isolines but with the other separatrix for $v_\parallel = +\infty$. In Fig. 6.2 it is also shown

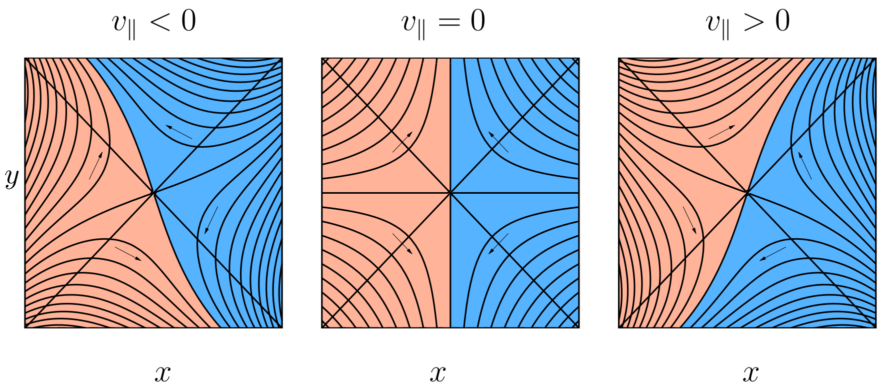

Figure 6.2: Particle trajectories for three values of $v_\parallel$.

that the particles coming from the hot side as well as those coming from the cold side never cross the separatrix $\phi + v_\parallel \psi = 0$. Since the position of this separatrix depends on $v_\parallel$, the distribution function in turn depends on the position: it is a superposition of the hot (T_+) electron distribution function f_+ for $v_\parallel < v_s$ and the cold (T_-) function f_- for $v_\parallel > v_s$, where $f_\pm$ is a correction to the leading order f_0. Because $v_s \equiv -\phi/\psi$ is a function of position, the moments of $f_\pm$ (density, current, and temperature) depend on position in the upper and lower quadrants. More specifically, they are functions of ϕ/ψ only:

$$\int_{-\infty}^{\infty} dv_\parallel \; f v_\parallel^n = \int_{-\infty}^{v_s} dv_\parallel \; f_+ v_\parallel^n + \int_{v_s}^{\infty} dv_\parallel \; f_- v_\parallel^n. \tag{6.5}$$

This general result relies entirely on the fact that the solution to the drift kinetic equation, Eq. (6.1), in stationary cases depends on the stream function only, $f = f(\phi + v_\parallel \psi)$, and it is not restricted to the specific functions chosen in Eqs. (6.4).

As an illustration, we choose Maxwellian distributions for the hot and cold particles,

$$f_0 + f_\pm = \frac{1}{\sqrt{\pi}} \frac{n_\pm}{v_\pm} \exp(-\frac{v_\parallel^2}{v_\pm^2}), \tag{6.6}$$

with thermal velocities $v_\pm = v_{th} \pm \delta v$ corresponding to $T_\pm = T_0 \pm 2 m_e v_{th} \delta v$, and densities $n_0 \pm \delta n$, respectively. To the first approximation in the perturbation amplitudes we have

$$f_\pm = \pm f_0 \left(\frac{\delta n}{n_0} - \frac{\delta v}{v_{th}} + 2 \frac{v_\parallel^2}{v_{th}^2} \frac{\delta v}{v_{th}} \right), \tag{6.7}$$

where $f_0 = (n_0/\sqrt{\pi} v_{th}) \exp(-v_\parallel^2/v_{th}^2)$. By means of Eqs. (6.5–6.7), the first three

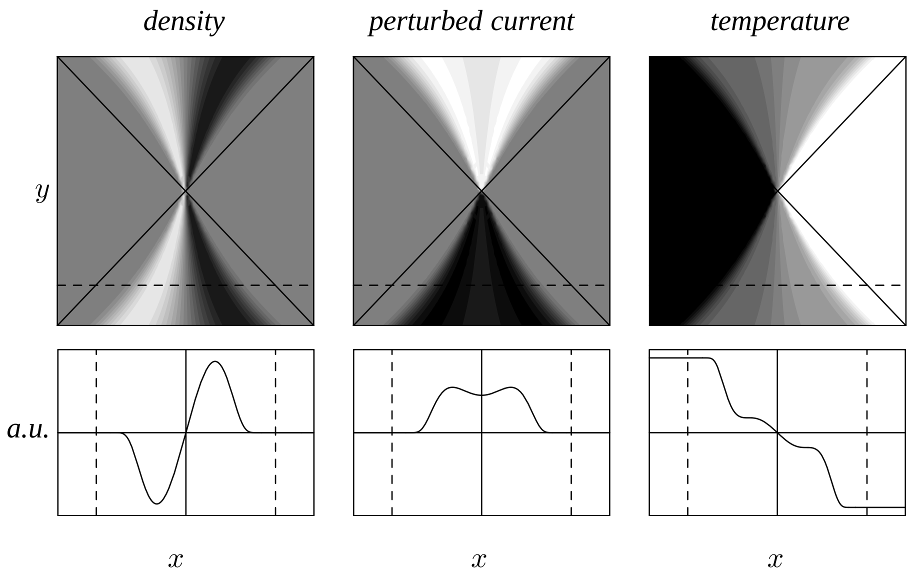

Figure 6.3: Density, perturbed current density, and temperature for $\delta n/n_0 = 0$. First row: contour plots; second row: profiles along the dashed line in the contour plots.

moments n, J, and T of $f_\pm$ in the upper and lower quadrants are obtained

$$\begin{aligned} n &= n_0\Big[\frac{2}{\sqrt{\pi}}\frac{\delta v}{v_{th}}\tilde{\phi}\,\mathrm{e}^{-\tilde{\phi}^2} - \frac{\delta n}{n_0}\mathrm{Erf}(\tilde{\phi})\Big], \\ J &= \frac{e n_0 v_0}{\sqrt{\pi}}\Big[\frac{\delta n}{n_0} + 2\frac{\delta v}{v_{th}}(\frac{1}{2} + \tilde{\phi}^2)\Big]\mathrm{e}^{-\tilde{\phi}^2}, \\ T &= m_e v_{th}^2\Big[\frac{\delta n}{n_0}\Big(\frac{1}{\sqrt{\pi}}\tilde{\phi}\,\mathrm{e}^{-\tilde{\phi}^2}\Big) + \frac{\delta v}{v_{th}}\Big(\frac{2}{\sqrt{\pi}}(\frac{1}{2} + \tilde{\phi}^2)\tilde{\phi}\,\mathrm{e}^{-\tilde{\phi}^2} - \mathrm{Erf}(\tilde{\phi})\Big)\Big]. \end{aligned} \quad (6.8)$$

They are function of $\tilde{\phi} = \phi/v_{th}\psi$ which is known by virtue of Eqs. (6.4), and are shown in Fig. 6.3 for the $\delta n/n_0 = 0$ case.

Figure 6.3 shows how a temperature difference in the inflowing plasma streams is accompanied by perturbation in density and current–and a matching profile in temperature–in the outflow regions. Conversely, a density difference between the inflow regions (at the same temperature, $\delta v = 0$) generates temperature modulations, as it is shown in Fig. 6.4 (first row). The isobaric case presented in Fig. 6.4 (second row), where the inflow regions are kept at the same pressure but different temperature and density, shows even more evident structures in the field profiles in the outflow regions.

Equations (6.8) are the sources in Eqs. (6.2, 6.3). A second question then arises: which are the effects of such perturbations on the electromagnetic potentials? A

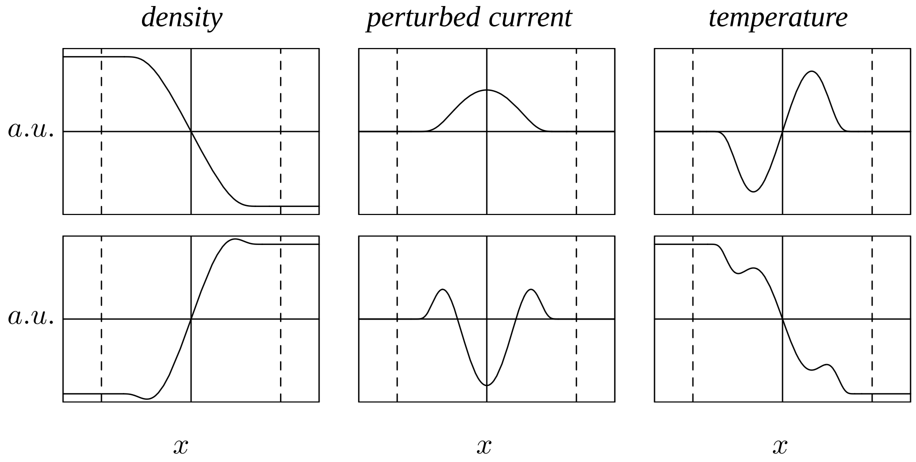

Figure 6.4: Profiles of density, perturbed current density, and temperature as in the 2^{nd} row of Fig. 6.3, 1^{st} row: $\delta v/v_{th} = 0$; 2^{nd} row: isobaric case.

simple solution to the self-consistent problem is found in the proximity of the X point, where the term proportional to d_e^{-2} in Ampère's law can be neglected. Expanding the ψ of Eq. (6.4) to first order in r/d_e, it follows that ϕ and ψ scale as r^2, thus $\tilde{\phi}$ has no radial dependence. Then also the modified electromagnetic potentials depend on the radial coordinate as r^2. In this case both Eqs. (6.2, 6.3) reduce to the form $y''(\theta) + 4y(\theta) = g(\theta)$, for which general solutions are known. Note that $g(\theta)$, here representing the sources, vanishes for $\frac{3}{4}\pi < \theta < \frac{5}{4}\pi$ and $-\frac{\pi}{4} < \theta < \frac{\pi}{4}$, *i.e.*, in the inflow regions. The solution is efficiently expressed in term of rotation angles of the separatrices

$$\theta_\phi = \frac{\Omega_i}{8\omega_0} \int_{\pi/4}^{3\pi/4} d\theta \cos(2\theta) n(\theta);$$

$$\theta_\psi = \frac{1}{8j_0} \int_{\pi/4}^{3\pi/4} d\theta \cos(2\theta) j(\theta),$$

for the electrostatic potential ϕ and the magnetic flux ψ, respectively. The angles of rotation are clockwise for $x > 0$ and anti-clockwise for $x < 0$. They measure the tilting of the separatrices of the fields ϕ and ψ of Eq. (6.4), respectively, due to the imposed temperature and density differences of the incoming plasma. Contour plots of the adjusted fields are shown in Fig. 6.5b. The parameter dependence can be clarified by the limits

$$\frac{\theta_\phi}{\theta_\psi} = \frac{\delta n/n_0 + \delta v/v_{th}}{\delta n/n_0 + 2\delta v/v_{th}} \left(\frac{v_A j_0}{\omega_0}\right)^2 \qquad \text{for } \frac{v_{th} j_0}{\omega_0} \ll 1,$$

$$\frac{\theta_\phi}{\theta_\psi} = \frac{\delta n/n_0}{\delta n/n_0 + \delta v/v_{th}} \frac{v_A^2 j_0}{v_{th}\omega_0} \qquad \text{for } \frac{v_{th} j_0}{\omega_0} \gg 1.$$

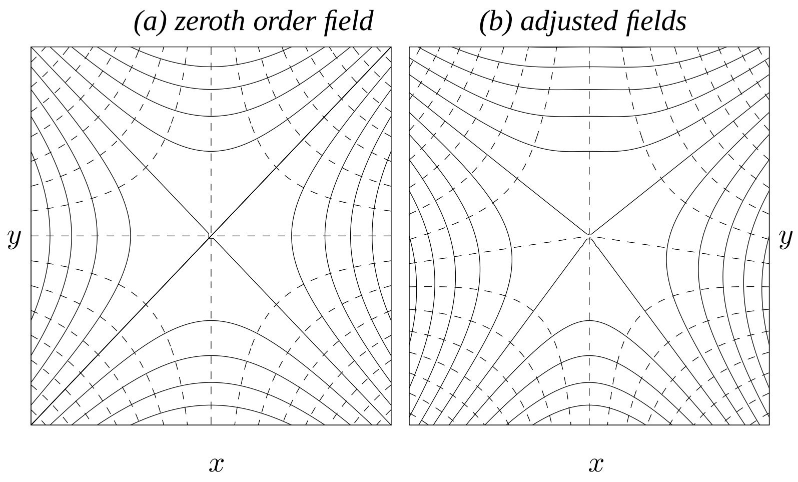

Figure 6.5: 0^{th} order (Eq. 6.4) and adjusted fields ψ (continuous lines) and ϕ (dashes).

6.3 Discussion.

In a simple X point geometry it has been shown how a left-right asymmetric temperature $T(x,y)$ leads to a breaking of the up-down symmetry of the electromagnetic potentials. The process is due to perturbed density and current density in the outflow regions. We point out that the functional dependences of the moments of the distribution function on ϕ/ψ in Eq. (6.8) are general results, not restricted to the specific functions chosen in Eq. (6.4). An open question is how the steady state reconnection process described above is affected by kinetic instabilities, as the perturbed distribution function has multiple maxima in $v_\parallel$ in regions of space where $\partial J/\partial x > 0$.

Landau resonances are absent in the problem treated in this chapter in contrast with what usually occur in time-dependent problems [12]. An example of that is the case of wave-particle effects in a field geometry which contains a finite size magnetic island chain, and it is treated in the next chapter.

7. Finite size island and kinetic effects

In this chapter the Maxwell-Vlasov system in the drift-Alfvén approximation, Eqs. (5.9–5.11), is employed to study the stability of a finite size magnetic island chain.

Equations (5.9–5.11) form the kinetic extension of a fluid model which has a Hamiltonian representation, see Section 2.3. The Hamiltonian character which pertains the fluid model is extended also to the kinetic equation [49] but only until resonant effects are included. The time-irreversible nature of Landau damping actually spoils the Hamiltonian structure.

7.1 Introduction

In order to explore the effects of finite temperature differences on reconnection the stability analysis of an equilibrium containing a finite size magnetic island chain is studied. The two dimensionality of the equilibrium island is treated by introducing a coordinate system in which field lines are straight. Landau resonance effects in a topology with finite size islands are investigated by expanding the governing equations in Fourier series along field lines. The resonant layer acts as an effective, space dependent resistivity in the linearized Ohm's law, at least for Maxwellian equilibria. In contrast with resistive effects, in the reconnection due to Landau damping the mechanism for reconnection takes place away from the X point. In fact, the wave-particle resonance takes place where the phase velocity of the wave is comparable with the electron thermal velocity. Assuming the mode eigenfrequency to be comparable with the electron drift frequency, $\omega^* = -cT_0 k_y/eB_0 L_n$, where L_n is the density gradient scale length and k_y the typical perturbation wave vector, then the location of the resonance is at

$$x_{\text{res}} \simeq \rho_e \frac{L_s}{L_n} \tag{7.1}$$

away from the separatrix of the equilibrium magnetic island. If x_{res} is much larger then the equilibrium island width than, due to the narrowness of the resonant layer, wave-particle and finite size island effects dominate the mode in separate locations in space. In this case the resonance effects are expected to be homologous to those treated in [12] within the thin island approximation. In this thesis we are interested in the opposite case of a resonant layer that is very close to the separatrix. In this case the presence of the island is expected to modify the resonance effects with respect to the thin island limit.

After the linearization, Eqs. (5.9–5.11) are expanded in Fourier series along isolines of constant magnetic flux. Then the solution of the drift kinetic equation is obtained and employed to compute the sources in the equations for the perturbed electrostatic potential and the magnetic flux. Next, an asymptotic method is used to compute the jump of the logarithmic derivative of the magnetic flux across the reconnection layer. The matching with the outer, ideal MHD region yields the dispersion relation.

In the thin island limit, the dispersion relation reproduces the results in [12] for the collisionless tearing mode.

Part of the results presented in this chapter are published in [52].

7.2 Linearized equations

Splitting physical quantities in their equilibrium and perturbed parts as $A = A_0 + \tilde{A}$, and assuming that all equilibrium quantities depend on space only through ψ_0, the linearization of the kinetic equation Eq. (5.9) yields

$$\begin{aligned} -i\omega\tilde{f} + \left(v_\phi + v_\parallel - \Omega_e\psi_0\right)\left[\psi_0, \tilde{f}\right] = \\ \frac{\partial f_0}{\partial\psi_0}\left[\psi_0, \tilde{\phi} + (v_\parallel - \Omega_e\psi_0)\tilde{\psi}\right], \end{aligned} \tag{7.2}$$

where ω is the mode eigenfrequency, and $v_\phi(\psi_0) \equiv d\phi_0/d\psi_0$ stems from the equilibrium $E \times B$ flow. The linearization of Eq. (5.10) leads to

$$-i\omega\tilde{\Gamma} + v_\phi[\psi_0, \tilde{\Gamma}] = [\psi_0, \tilde{\phi}]\Big(\frac{d\Delta\phi_0}{d\psi_0} - \Omega_i\frac{d\ln n_0}{d\psi_0}\Big) \tag{7.3}$$

with

$$\tilde{\Gamma} = \Delta\tilde{\phi} - \frac{\Omega_i}{n_b}\int_{-\infty}^{\infty}\tilde{f}dv_\parallel; \tag{7.4}$$

the linear version of Eq. (5.11) is

$$\tilde{\psi} - d_e^2\Delta\tilde{\psi} = \frac{1}{\Omega_e n_b}\int_{-\infty}^{\infty}(v_\parallel - \Omega_e\psi_0)\tilde{f}dv_\parallel, \tag{7.5}$$

where $n_0 = n_b + \int dv_\parallel f_0$ contains both the constant bulk and the equilibrium space dependent density contributions. A term proportional to $\tilde{\psi}(n_0 - n_b)/n_b$ was neglected in Ampére's law because it is second order in the perturbation. In the source equations Eqs. (7.3–7.5) the solution of the drift kinetic equation must be used, thus Eq. (7.2) must first be inverted. To this aim the equilibrium configuration must be specified. We consider a stationary initial state which contains the finite size magnetic islands chain of width x_0 and period πy_0 given by

$$\psi_0 = 2\psi_r\Big(\frac{x^2}{x_0^2} + \sin^2(y/y_0)\Big), \tag{7.6}$$

where ψ_r is a constant related to the equilibrium magnetic shear L_s as $\psi_r = x_0^2/4L_s$. The O points are located along the y axis at even multiples of $\pi y_0/2$, the X points at odd ones, and the value of the magnetic flux on the separatrix is $2\psi_r$. The ratio x_0/y_0, although finite, is considered to be small. The electrostatic potential ϕ_0 and its Laplacian, the vorticity $\Delta\phi_0$, are assumed to be function of ψ_0 only. The corresponding distribution function is a function of ψ_0 and $v_\|$ only. As equilibrium distribution function let us take the shifted Maxwellian[1]

$$\begin{aligned}\overline{F}_0 &= f_b(v_\|) + f_0(\psi_0, v_\|) = \\ &\frac{n_0}{\sqrt{\pi}v_{th}}\left[1 - 2\frac{V_0}{v_{th}}\frac{v_\| - \Omega_e\psi_0}{v_{th}}\right]\exp\left\{-\frac{(v_\| - \Omega_e\psi_0)^2}{v_{th}^2}\right\},\end{aligned} \tag{7.7}$$

where V_0 is the equilibrium fluid velocity along the z direction, which is taken to be constant in space and much smaller than the thermal velocity, $V_0/v_{th} \ll 1$. This velocity sustains the constant equilibrium current. In fact, the current generated by the magnetic field related to Eq. (7.6) as given by the Ampére law contains a y dependent contribution that is second order in x_0/y_0. Discarding it, also the equilibrium current reduces to a constant.

7.3 Coordinate system with straight field lines

In order to solve the above set of equation a coordinate system which allows for Fourier expansions along field lines will be employed. Here such a coordinate system is defined. Referring to Eq. (7.6), the derivative of a function $A(x, y)$ along a field line is

$$[\psi_0, \tilde{A}] = \partial_x\psi_0(x, y)\,\partial_y\tilde{A}(\psi_0, y). \tag{7.8}$$

Let us define the longitudinal variable $\lambda(x, y)$ as the integral along a contour ψ_0=constant,

$$\lambda \equiv \int_0^y \frac{dy'}{\partial_x\psi_0(x, y')} = \frac{x_0}{4\psi_r}\int_0^y \frac{dy'}{\sqrt{2\psi_0/\psi_r - \sin^2(y'/y_0)}} \tag{7.9}$$

---

[1] The thermal velocity is defined as $v_{th}^2 \equiv 2T_0/m_e$.

which yields $[\psi_0, \lambda] = 1$. Let us define the *parameter* m for elliptic functions and integrals by

$$m \equiv 2\frac{\psi_r}{\psi_0} = \frac{1}{x^2/x_0^2 + \sin^2(y/y_0)};$$

it is $m = 1$ on the separatrix, $0 < m < 1$ for field lines outside the separatrix, and $1 < m < \infty$ for field lines inside the separatrix. Then, on open field lines λ can be expressed as an elliptic integral of the first kind,

$$\lambda = \frac{y_0}{x_0} L_s m^{1/2} F(y/y_0, m).$$

For $y = \frac{1}{2}\pi y_0$ we find the half-period

$$\lambda_m = \frac{y_0}{x_0} L_s m^{1/2} K(m),$$

where $K(m)$ is the complete elliptic integral of the first kind. On closed contours one has the same expression for λ_m, provided that $K(m)$ is replaced by its real part, Re$\{K(m)\} = m^{-1/2} K(m^{-1})$. Retaining only the real parts of elliptic integrals, we define the normalized longitudinal coordinate

$$\hat{\lambda} \equiv \frac{\pi\lambda}{\lambda_m} = \frac{\pi}{K(m)} u, \qquad u \equiv F(y/y_0, m). \tag{7.10}$$

Both on open and closed contours, quantities are periodic in $\hat{\lambda}$ with period 2π. Finally, we introduce a more convenient flux function in terms of the complete elliptic integral of the second kind $E(m)$,

$$\hat{\psi}(\psi_0) \equiv \frac{E(m)}{\pi m^{1/2}}, \qquad \frac{d\hat{\psi}}{dm} = -\frac{K(m)}{2\pi m^{3/2}}, \tag{7.11}$$

with the property that the coordinate transformation to $(\hat{\psi}, \hat{\lambda})$ has a constant Jacobian, $[\hat{\psi}, \hat{\lambda}] = 1/x_0 y_0$. The geodetics of the reference system $\hat{\psi}$, $\hat{\lambda}$ are plotted in Fig. 7.3.

The Laplacian of the generic scalar function $A(x, y)$ transforms as

$$\Delta A = \frac{\partial}{\partial \xi^i}\Big(g^{ij}\frac{\partial A}{\partial \xi^j}\Big), \tag{7.12}$$

where $\xi = (\hat{\psi},\ \hat{\lambda})$ and $g^{ij} = g^{ij}(\hat{\psi},\ \hat{\lambda})$ are the metric tensor coefficients of the coordinate system transformation,

$$g^{\psi\psi} = |\nabla\hat{\psi}|^2, \quad g^{\psi\lambda} = \nabla\hat{\psi} \cdot \nabla\hat{\lambda}, \quad g^{\lambda\lambda} = |\nabla\hat{\lambda}|^2. \tag{7.13}$$

Explicit expressions for g^{ij} are given in the Appendix B.2.

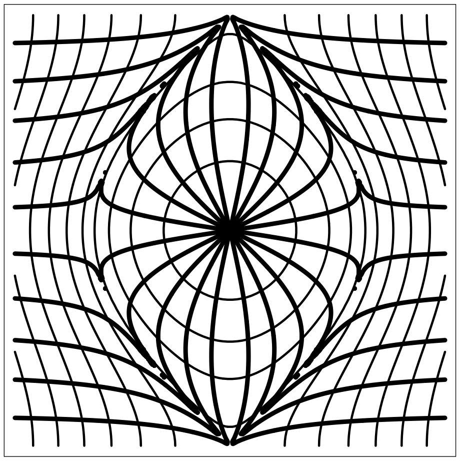

Figure 7.1: Isolines of $\hat{\psi}$ (thin) and $\hat{\lambda}$ (thick)

7.4 Fourier expansion along field lines

Let us now introduce the Fourier expansion along field lines. The variation of $\tilde{A}$ along the magnetic field $\mathbf{B}_0 = B_0(\mathbf{e}_z + \mathbf{e}_z \times \nabla\psi_0)$ is given by $B_0^{-1}\mathbf{B}_0 \cdot \nabla\tilde{A} = [\psi_0, \tilde{A}]$. Expanding $\tilde{A}$ in Fourier harmonics in $\hat{\lambda}$ as

$$\begin{aligned}\tilde{A}(\hat{\psi},\hat{\lambda}) &= \sum_l e^{il\hat{\lambda}}\tilde{A}_l(\hat{\psi}),\\ \tilde{A}_l(\hat{\psi}) &= \frac{1}{2\pi}\oint d\hat{\lambda}\, e^{-il\hat{\lambda}}\tilde{A}(\hat{\psi},\hat{\lambda}),\end{aligned} \tag{7.14}$$

where the integral is taken at constant $\hat{\psi}$. It follows that

$$[\psi_0,\tilde{A}] = [\hat{\psi},\hat{\lambda}]\frac{d\psi_0}{d\hat{\psi}}\frac{\partial\tilde{A}}{\partial\hat{\lambda}} = \frac{1}{x_0y_0}\frac{d\psi_0}{d\hat{\psi}}\sum_l il e^{il\hat{\lambda}}\tilde{A}_l = \sum_l ik_\parallel e^{il\hat{\lambda}}\tilde{A}_l, \tag{7.15}$$

where the parallel wave vector corresponding to the linearized parallel gradient in the straight field line coordinate system is defined as

$$k_\parallel \equiv \frac{l}{x_0y_0}\frac{d\psi_0}{d\hat{\psi}} = \frac{\pi x_0}{L_s y_0}\frac{l}{\sqrt{m}K(m)}. \tag{7.16}$$

Note that far from the equilibrium island chain, *i.e.* for $m \to 0$, $k_\parallel$ is proportional to x. This correspond to the limit in which the field line bending due to the presence of the equilibrium island is negligible. The treatment, and results, of the known thin island approximation (see *e.g.* the cold ion limit of [12]) can be applied in this limit.

7.5 Final set of linearized equations

Applying the straight field line transformation to the linearized kinetic equation, Eq. (7.2), Fourier expanding and using Eq. (7.15), the l-*th* component of the distribution function is

$$\tilde{f}_l = \frac{k_\parallel}{-\omega + k_\parallel\left(v_\phi + v_\parallel - \Omega_e\psi_0\right)}\left(\tilde{\phi}_l + (v_\parallel - \Omega_e\psi_0)\tilde{\psi}_l\right)\frac{\partial f_0}{\partial \psi_0}. \tag{7.17}$$

This solution is now used to compute the moments of the distribution function in the source equations. We write Eqs. (7.3, 7.5) in the variable $\hat{\psi}, \hat{\lambda}$ using the expression for the Laplacian given in the previous section. After the Fourier expansion we use the solution Eq. (7.17) and integrate over $v_\parallel$. To this purpose it is useful to express the derivative of the equilibrium distribution in Eq. (7.17) as

$$\frac{\partial f_0}{\partial \psi_0} = \frac{d\ln n_0}{d\psi_0} f_0 - \Omega_e\frac{\partial f_0}{\partial v_\parallel} + \frac{1}{2m_e}\frac{dT_0}{d\psi_0}\frac{\partial^2 f_0}{\partial v_\parallel^2}. \tag{7.18}$$

In this way Eqs. (7.3-7.5) become

$$\begin{aligned} \frac{\rho_s^2}{2}(\Delta\tilde{\phi})_l &= P_s(\hat{\psi})\left(v_{th}\zeta\tilde{\psi}_l + \tilde{\phi}_l\right) + \eta_\omega\frac{\Omega^*}{\omega - k_\parallel v_\phi}\tilde{\phi}_l, \\ \frac{d_e^2 v_{th}}{2}(\Delta\tilde{\psi})_l &= -P_s(\hat{\psi})\zeta\left(v_{th}\zeta\tilde{\psi}_l + \tilde{\phi}_l\right), \end{aligned} \tag{7.19}$$

where $\zeta(\hat{\psi}) \equiv (\omega - k_\parallel v_\phi)/k_\parallel v_{th}$ is the complex, space-dependent normalized phase velocity which includes the Doppler shift due to the equilibrium electric potential, and $\rho_s \equiv c\sqrt{2T_0 m_i}/eB_0$ is the ion sound gyroradius. The symbol $(\Delta\tilde{A})_l$ stands for the l-*th* Fourier coefficient in $\hat{\lambda}$ of the Laplacian of $\tilde{A}$. Finally, the function

$$\begin{aligned} P_s(\hat{\psi}) \equiv -\frac{1}{2}\frac{\Omega^*}{\omega - k_\parallel v_\phi}\eta_T\frac{d}{d\zeta}[\zeta W(\zeta)] - \\ W(\zeta)\left[1 - \frac{\Omega^*}{\omega - k_\parallel v_\phi}\left(1 + \frac{1}{2}\eta_T\right)\right], \end{aligned} \tag{7.20}$$

contains several effects. First, the resonance effects are described by the plasma response function W,

$$W(\zeta) \equiv -(1 + \zeta\mathcal{Z}), \qquad \mathcal{Z}(\zeta) \equiv \frac{1}{\sqrt{\pi}}\int_{-\infty}^{\infty}\frac{e^{-t^2}}{t - \zeta}dt. \tag{7.21}$$

Second, equilibrium gradients in density, temperature, and vorticity are accounted for by Ω^*, η_T, and η_ω respectively,

$$\Omega^* \equiv -\frac{cT_0}{eB_0}\frac{l}{x_0 y_0}\frac{d\ln n_0}{d\hat{\psi}}, \qquad \eta_T = \frac{d\ln T_0}{d\ln n_0}, \qquad \eta_\omega = \frac{1}{\Omega_i}\frac{d\Delta\phi_0}{d\ln n_0}.$$

Far from the separatrix it is $d\hat{\psi}/dx \simeq 1/2x_0$ so that $\Omega^* \simeq \omega^*$, where $\omega^* \equiv -cT_0k_y/eB_0L_n$ is the drift frequency, $L_n^{-1} \equiv d\ln n_0/dx$, and $k_y \equiv 2l/y_0$.

The interpretation of Eqs. (7.19) is straightforward. For negligible η_ω and v_ϕ, Eqs. (7.19) can be compactly rewritten as

$$\omega(\Delta\tilde{\phi})_l = -k_\parallel v_A^2(\Delta\tilde{\psi})_l, \tag{7.22}$$

$$J_{\parallel,l} = \frac{c^2}{4\pi}\eta_{kin}^{-1}E_{\parallel,l}, \tag{7.23}$$

respectively. The first equation represents charge conservation, and can be directly compared with Eq. (3.5). The second equation is the fundamental equation for reconnection, see Eq. (1.7) and Eq. (3.6), which relates in Fourier space the parallel component of the electric field, $E_\parallel = (B_0/c)(-\nabla_\parallel\tilde{\phi} + \partial_t\tilde{\psi})$, to the parallel current, $J_\parallel = (B_0c/4\pi)\Delta\tilde{\psi}$. Equation (7.23) expresses the violation of flux conservation allowed by the kinetic resistivity

$$\eta_{kin} \equiv i\frac{d_e^2\omega}{2\zeta^2 P_s(\zeta)}, \tag{7.24}$$

which depends on space through $k_\parallel$-dependence on ζ, and on the equilibrium gradients through P_s. It is on the ground of Eq. (7.23) that wave-particle effects are recognized to break the frozen-in law, in this way providing a mechanism for reconnection.

The set of Eqs. (7.19) are coupled second order differential equations for the Fourier components $\tilde{\phi}_l$ and $\tilde{\psi}_l$.
The Fourier expansion of the Laplacian operator is given by $\Delta\tilde{A} = \sum_l(\Delta\tilde{A})_l e^{il\hat{\lambda}}$, where

$$(\Delta\tilde{A})_l \equiv \sum_j \Delta_{lj}(\tilde{A}_j),$$

$$\Delta_{lj} = \frac{d}{d\hat{\psi}}g_{l-j}^{\hat{\psi}\hat{\psi}}\frac{d}{d\hat{\psi}} + ilg_{l-j}^{\hat{\psi}\hat{\lambda}}\frac{d}{d\hat{\psi}} + ij\frac{d}{d\hat{\psi}}g_{l-j}^{\hat{\psi}\hat{\lambda}} - ljg_{l-j}^{\hat{\lambda}\hat{\lambda}}, \tag{7.25}$$

and $g_p^{mn}(\hat{\psi})$ are the Fourier coefficients of the metric tensor elements,

$$g_p^{mn}(\hat{\psi}) = \frac{1}{2\pi}\oint d\hat{\lambda}\, e^{-ip\hat{\lambda}}g^{mn}(\hat{\psi},\hat{\lambda}). \tag{7.26}$$

The reader is referred to the Appendix B.3 for their explicit expressions.
It follows from Eq. (7.25) that each harmonic $\tilde{A}_l$ is coupled by the Laplacian operator to all the other harmonics $\tilde{A}_{j\neq l}$. A study of the matrix tensor coefficients reveals that close to the separatrix the coupling is of comparable order for a wide range of $j - l$ values, so no single harmonic dominates the solution. In order to solve Eqs. (7.19) we have to introduce approximations.

7.6 Dispersion relation

The wave-particle resonance takes place where the phase velocity of the wave is comparable with the electron thermal velocity, *i.e.* when $\zeta \sim 1$. Although an explicit expression for ζ is obtainable only once the eigenfrequency ω is known, we can estimate it by anticipating that ω is comparable with the electron drift frequency ω^*. Then the location of the resonance is approximately at

$$x_{\text{res}} \simeq \rho_e \frac{L_s}{L_n} \tag{7.27}$$

away from the separatrix of the equilibrium magnetic island. If x_{res} is much larger than the equilibrium island width than, due to the narrowness of the resonant layer, wave-particle and finite size island effects dominate the mode in separate locations in space. In this case the resonance effects are expected to be homologous to those treated in [12] within the thin island approximation. Here we treat the opposite limit, where the resonant layer is very close to the separatrix.

7.6.1 The method of asymptotic regions

In this section the dispersion relation is derived from system Eqs. (7.19) in the constant ψ approximation. The dispersion relation is found by matching the jump of the logarithmic derivative across the reconnection layer Δ'_{rl} with the one of the region outside the reconnection layer Δ', *i.e.*,

$$\Delta' = \Delta'_{rl}. \tag{7.28}$$

The outer region is the MHD region, characterized by $E_\parallel = 0$, where the solutions for the electromagnetic potentials are those given in Eqs. (3.66). In the analysis presented here, the value of Δ' determined by the dynamics in the outer region is regarded as a given parameter.

The jump of the logarithmic derivative across the reconnection layer is given by

$$\Delta'_{rl} = \frac{1}{\psi_\infty} \int_{rl} dx \; (\Delta\tilde{\psi})_{k_y}. \tag{7.29}$$

Note that the above is the k_y Fourier coefficient in y of the current density integrated in x. The expression for the current density that contains the resonance effects is given in Eqs. (7.19) as a Fourier coefficient in $\hat{\lambda}$. Hence, the transformation from Fourier in y to Fourier in $\hat{\lambda}$ is needed. Using Eqs. (7.19) in Eq. (7.29) yields

$$\Delta'_{rl} = -\frac{2}{d_e^2 v_{th} \psi_\infty} \int_{rl} dx \left[P_s(\zeta)\zeta \Big(v_{th}\zeta\tilde{\psi}_l + \tilde{\phi}_l \Big) \right]_{k_y} \tag{7.30}$$

where the subscript k_y indicates the k_y Fourier component in y of the expression in brackets. Expressed in $\hat{\lambda}$-Fourier coefficients $A_l(\hat{\psi})$ we can write

$$\begin{aligned} A_{k_y}(x) &= \frac{1}{\pi y_0} \oint dy\, e^{-ik_y y} A(\mathbf{x}) \\ &= \frac{1}{\pi y_0} \sum_l \oint dy\, e^{-ik_y y + il\hat{\lambda}(x,y)} A_l(\hat{\psi}(x,y)). \end{aligned} \tag{7.31}$$

In this way Eq.(7.30) can be written

$$\begin{aligned} \Delta'_{rl}(k_y) = &- \frac{2}{d_e^2 v_{th} \psi_\infty} \oint \frac{dy}{\pi y_0} \times \\ &\sum_l \int_{rl} dx\, e^{-ik_y y + il\hat{\lambda}} P_s(\zeta_l) \zeta_l \Big(v_{th} \zeta_l \tilde{\psi}_l + \tilde{\phi}_l \Big), \end{aligned} \tag{7.32}$$

where the subscript to ζ_l indicates that ζ depends on the index l.
In order to compute the latter integral, two regions are identified inside the reconnection layer in which different orderings apply. These regions are taken to be far apart so that the overlap of solutions of different regions is minimal. In this sense the regions are asymptotic and the integral above can be extended to the whole domain for each contribution separately.
The first region we consider is the fluid-like region, that is between the MHD region and the equilibrium island chain, far away from the resonance. Here the normalized phase velocity is small and the equations become fluid-like, with both the electrostatic potential and the magnetic flux terms contributing to $E_\|$. Moreover, the effects of the curvature of field lines is negligible. The contribution to Δ'_{rl} from the fluid region is indicated with Δ'_s, and its explicit expression is given in Subsection 7.6.3. The problem is homologous to that treated in [53]. In that paper ions have a finite temperature and an additional resonance is present. The cold ion limit of the contribution to the Δ'_{rl} due to ions derived in [53] reduced to the Δ'_s derived in Subsection 7.6.3.
The second region is the electron region, which yields a contribution Δ'_e to Δ'_{rl}. Here the parallel wave vector is small, and the parallel electric field is essentially inductive. In this region two effects are considered. The first is the electron resonance, as it is in [53]. Additionally we consider the effects of the curvature of the field lines. This is the extension with respect to the work presented in [53].
The matching condition is then

$$\Delta' = \Delta'_e + \Delta'_s. \tag{7.33}$$

In order to simplify the analytical treatment we take in Eqs. (7.19) no equilibrium vorticity ($\eta_\omega = 0$), and negligible equilibrium $E \times B$ velocity ($v_\phi \ll \omega/k_\|$). Additionally, let us consider a density profile such that $d \ln n_0 / d\hat{\psi} = 2x_0/L_n =$

constant outside the island, while $n_0 \simeq$ constant inside. This profile becomes linear in x at large x.
In the following we will show that eigenmodes have frequencies comparable with ω^*. Two neighboring modes have very different frequencies if k_y is small. In this case only one mode is resonant and coupling between adjacent modes $k_y \pm 2/y_0$ is small. Hence, we will consider perturbations with small values of k_y, in this way selecting only one harmonic in y and limiting the effects of finite a island chain to the resonance.

7.6.2 Electron region

The function $P_s(\zeta)$ in Eqs. (7.19) contains two contributions, one proportional to $W(\zeta)$ and the other proportional to the derivative of $\zeta W(\zeta)$, respectively. We then split Δ'_e into two terms accordingly

$$\Delta'_e = \Delta'_{e0} + \Delta'_{e1}, \tag{7.34}$$

where

$$\begin{aligned}
\Delta'_{e0} = \frac{2}{d_e^2 v_{th}\tilde{\psi}_\infty} \oint \frac{dy}{\pi y_0} \sum_l \int_{rl} dx \quad & e^{-ik_y y + il\hat{\lambda}}\, \zeta_l^2 W(\zeta_l) \times \\
& \Big(\tilde{\psi}_l v_{th}\zeta_l + \tilde{\phi}_l\Big)\Big(1 - \frac{\Omega_l^*}{\omega}(1 + \frac{\eta_T}{2})\Big), \\
\Delta'_{e1} = -\frac{1}{d_e^2 v_{th}\tilde{\psi}_\infty}\eta_T \oint \frac{dy}{\pi y_0} \sum_l \int_{rl} dx \quad & e^{-ik_y y + il\hat{\lambda}}\, \zeta_l \frac{d}{d\zeta_l}\Big(W(\zeta_l)\zeta_l\Big) \times \\
& \Big(\tilde{\psi}_l v_{th}\zeta_l + \tilde{\phi}_l\Big)\frac{\Omega_l^*}{\omega}
\end{aligned} \tag{7.35}$$

The dependence of the diamagnetic frequency on l is reminded by the subscript on Ω_l^*. In the electron region $k_\parallel$ is small, and the parallel electric field is predominantly inductive. This corresponds to neglecting $\tilde{\phi}_l$ with respect to $\zeta v_{th}\tilde{\psi}_l$ in Eqs. (7.35). In this case, and in combination with the constant ψ approximation, it is shown below that Δ'_{e1} identically vanishes in the thin island limit. Hence, in the thin island limit the electrostatic potential cannot be neglected in Δ'_{e1}. The corresponding different orderings in $k_\parallel$ of $E_\parallel$ is the reason for the subscripts to the two contributions to Δ'_e which is used also in [53]. Although in the more general case of a finite size island case Δ'_{e1} does not vanish as it is shown in the following, the same notation is kept for the sake of comparison.
The constant ψ approximation, $\tilde{\psi}(\mathbf{x}) = \tilde{\psi}_\infty \exp i r_y y$, enable us to write

$$\tilde{\psi}_l(\hat{\psi}) = \tilde{\psi}_\infty \oint \frac{d\hat{\lambda}}{2\pi} e^{i r_y y(\hat{\psi},\hat{\lambda}) - il\hat{\lambda}}. \tag{7.36}$$

In the following it is shown that the eigenfrequency is close to the diamagnetic frequency. In the final dispersion relation the quantity $(1 - \omega^*/\omega)$ appears. This factor is small only for one mode at a time if k_y is small, due to the fact that the relative difference in frequency between adjacent modes is larger for smaller k_y. Hence, we limit the analysis to modes with large k_y, so that only one frequency at a time is resonant, which means to put $r_y = k_y$ in the above expression for $\tilde{\psi}_l$.

The integrals in Eqs. (7.35) can be rewritten in terms of $(\hat{\psi}, \hat{\lambda})$ coordinates as

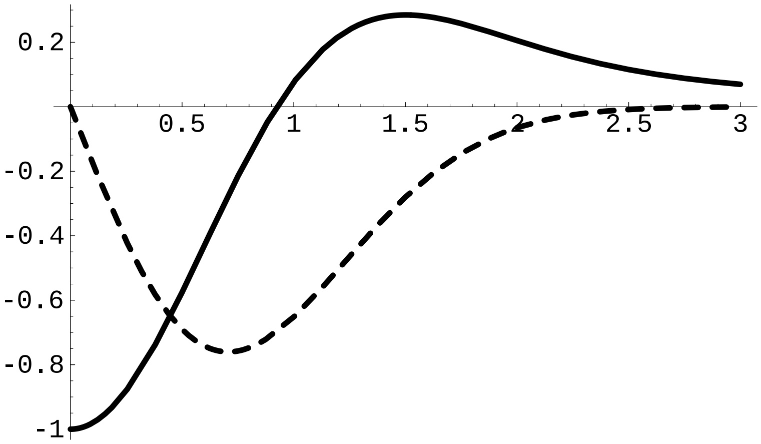

Figure 7.2: The real (continuous) and the imaginary (dashed) parts of the plasma response function $W(\zeta)$, for real ζ

$$\oint dy \int_{rl} dx = x_0 y_0 \oint d\hat{\lambda} \int_{rl} d\hat{\psi}, \tag{7.37}$$

using the Jacobian given in Section 7.3. Using the constant ψ approximation and Eq. (7.36), and changing $(\hat{\psi}, \hat{\lambda})$ coordinates, Eqs. (7.35) become

$$\begin{aligned}
\Delta'_{e0} = \frac{4x_0}{d_e^2} \oint \frac{d\hat{\lambda}}{2\pi} \oint \frac{d\hat{\lambda}'}{2\pi} \quad & e^{-ik_y(y-y')} \sum_l \Big(1 - \frac{\Omega_l^*}{\omega}(1 + \frac{\eta_T}{2})\Big) \times \\
& \int_{rl} d\hat{\psi}\; e^{il(\hat{\lambda}-\hat{\lambda}')}\; \zeta_l^2 W(\zeta_l), \\
\Delta'_{e1} = -\frac{2x_0}{d_e^2}\eta_T \oint \frac{d\hat{\lambda}}{2\pi} \oint \frac{d\hat{\lambda}'}{2\pi} \quad & e^{-ik_y(y-y')} \sum_l \frac{\Omega_l^*}{\omega} \times \\
& \int_{rl} d\hat{\psi}\; e^{il(\hat{\lambda}-\hat{\lambda}')}\; \zeta_l \frac{d}{d\zeta_l}\Big(W(\zeta_l)\zeta_l\Big),
\end{aligned} \tag{7.38}$$

where $y = y(\hat{\psi}_{rl}, \hat{\lambda})$ and $y' = y(\hat{\psi}_{rl}, \hat{\lambda}')$. We now use

$$\frac{d\hat{\psi}}{d\zeta_l} = -l\frac{v_{th}x_0}{\omega L_s y_0}\frac{(1-m)K(m)}{mE(m)}, \tag{7.39}$$

to change variable from $\hat{\psi}$ to ζ. We then integrate in $d\zeta_l$ by assuming that resonances are narrow. The graph of $W(\zeta_l)$ for real ζ_l is plotted in Fig. 7.2. Let us introduce the following relations

$$d\hat{\psi}\,\zeta_l^2 = -\frac{\omega L_s y_0}{l v_{th} x_0}M_0(m)\,d\zeta_l, \qquad -\zeta_l\frac{dM_0}{d\zeta_l} = M_1, \tag{7.40}$$

where

$$\begin{aligned} M_0(m) &\equiv \frac{(1-m)K^3(m)}{\pi^2 E(m)}, \\ M_1(m) &\equiv \Big(2(2-m)\frac{K}{E} - 3 - (1-m)\frac{K^2}{E^2}\Big)M_0. \end{aligned} \tag{7.41}$$

The graphs of $M_{0,1}$ are shown in Fig. 7.3. The $\hat{\psi}$ integrals in Eqs. (7.38) are now

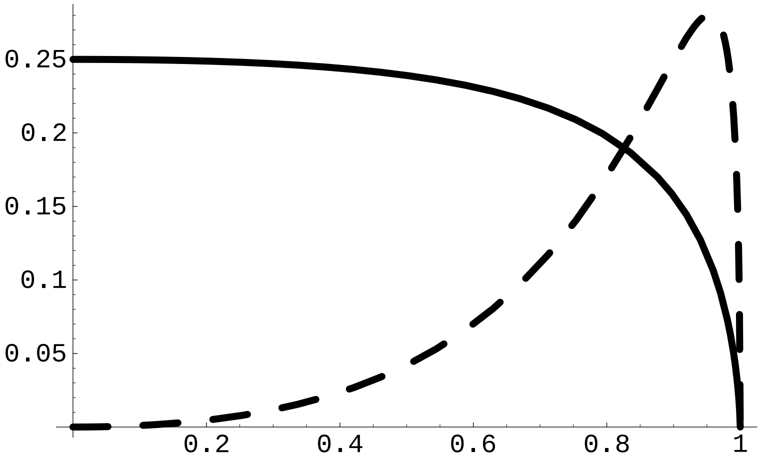

Figure 7.3: Graphs of $M_0(m)$ (continuous line) and $M_1(m)$ (dashes) defined in Eq. (7.41), as a function of m

approximated using

$$\int_{rl} d\zeta_l\, M_{0,1}(m)W(\zeta_l) \simeq M_{0,1}(m_l)\int_{rl} d\zeta_l\, W(\zeta_l) = -\frac{i}{2}\sqrt{\pi}M_{0,1}(m_l), \tag{7.42}$$

where m_l is the value of m at which the resonance is located. Taking for it the value of ζ_l at which the imaginary part of $W(\zeta_l)$ has its minimum, $\zeta_l = 1/\sqrt{2}$, the value of m_l is fixed by the relation $\zeta_l = 1/\sqrt{2}$, *i.e.*,

$$\sqrt{m_l}K(m_l) = \frac{v_{th}\pi x_0}{\sqrt{2}\omega L_s y_0} l. \tag{7.43}$$

The location of the resonance depends in a non trivial way from the index l. To consider the resonance to be very narrow gave the possibility of an explicit computation of the resonance contribution. The approximation on the integral over the reconnection layer allows to rewrite Eqs. (7.38) as

$$\begin{aligned}
\Delta'_{e0} = -2i\sqrt{\pi}\frac{\omega L_s y_0}{v_{th} d_e^2} & \oint \frac{d\hat{\lambda}}{2\pi} \oint \frac{d\hat{\lambda}'}{2\pi} e^{-ik_y(y-y')} \times \\
& \sum_l e^{il(\hat{\lambda}-\hat{\lambda}')} \frac{M_0(m_l)}{l} \Big(1 - \frac{\Omega_l^*}{\omega}(1 + \frac{\eta_T}{2})\Big), \\
\Delta'_{e1} = i\sqrt{\pi}\frac{\omega L_s y_0}{v_{th} d_e^2}\eta_T & \oint \frac{d\hat{\lambda}}{2\pi} \oint \frac{d\hat{\lambda}'}{2\pi} e^{-ik_y(y-y')} \times \\
& \sum_l e^{il(\hat{\lambda}-\hat{\lambda}')} \frac{M_1(m_l)}{l} \frac{\Omega_l^*}{\omega},
\end{aligned} \tag{7.44}$$

Because of the dependence of $M_{0,1}$ on the index l the sum over l cannot be performed. In order to understand the physical implication of the above results it is useful to recognize that the approximation Eq. (7.42) basically extracts from the integral the width of the resonance. The inspection of Eq. (7.44) is clarified by the examination of the thin island limit.

Thin island limit

The thin island limit in [53] is recovered when the resonances are far from the island, *i.e.* for $m \longrightarrow 0$. In this limit the Fourier transform in $\hat{\lambda}$ becomes a Fourier transform in y, $\hat{\lambda} \simeq 2y/y_0$. Far from the island it is

$$M_0(m \longrightarrow 0) \simeq \frac{1}{4}, \qquad M_1(m \longrightarrow 0) \simeq 0. \tag{7.45}$$

Thus in the first place we recover the result that Δ'_{e1} vanishes in the thin island limit. In this case, the hypothesis of inductive parallel electric field cannot be applied in the calculation of this term, and the inclusion of the electrostatic potential is necessary for a correct evaluation. However, it can be shown that the Δ'_{e1} calculated including the electrostatic potential has a stabilizing effects. Because we are interested in the modification of the instability due to the finite size island, we neglect this correction. The reader is referred to [53] for more details on this

point.
Consider now Δ'_{e0}. The double integral with $M_0 = 1/4$ reduces to the Kronecker symbol $\delta_{k,l}$, and we obtain

$$\Delta'_e = \Delta'_{e0} = -i\frac{\sqrt{\pi}}{2}\frac{\omega}{\omega^*}\delta_e\Bigg(1 - \frac{\omega^*}{\omega}(1 + \frac{\eta_T}{2})\Bigg) \tag{7.46}$$

with $\delta_e \equiv \rho_e L_s/L_n$ being the width of the resonance. Writing the real and imaginary part of ω as $\omega = \omega_R + i\omega_I$ and substituting in Eq. (7.33) we have

$$\begin{aligned} \omega_R &= \omega^*(1 + \frac{\eta_T}{2}), \\ -i\frac{\sqrt{\pi}}{2}\frac{\omega_I}{|\omega^*|} &= \frac{d_e^2}{\delta_e}(\Delta' - \Delta'_s), \end{aligned} \tag{7.47}$$

which is the result obtained in [53]. Note that no restriction was imposed on the relative magnitude of the real and imaginary part of the frequency.

Finite size island effects

In this subsection the general results in Eqs. (7.44) is analyzed. One effect of the finite size island is that Δ'_{e1} is in general finite also in the constant ψ approximation. Hence it is appropriate to recombine the two contributions to Δ'_e,

$$\begin{aligned} \Delta'_e = \Delta'_{e0} + \Delta'_{e1} = \\ -2i\frac{\sqrt{\pi}}{d_e^2}\frac{\omega}{\omega^*}\oint\frac{d\hat{\lambda}}{2\pi}\oint\frac{d\hat{\lambda}'}{2\pi}\sum_l \frac{k}{l}\, e^{-ik_y(y-y')+il(\hat{\lambda}-\hat{\lambda}')} \times \\ \Big(\rho_e\frac{L_s}{L_n}M_0(m_l)\Big)\Big[1 - \frac{\Omega_l^*}{\omega}(1 + \frac{\eta_T}{2}) - \frac{1}{2}\eta_T\frac{\Omega_l^*}{\omega}\frac{M_1}{M_0}\Big], \end{aligned} \tag{7.48}$$

In view of Eq. (7.42) the resonance width is generalized to

$$\delta_{e,l} \equiv 4\rho_e\frac{L_s}{L_n}M_0(m_l). \tag{7.49}$$

The resonance width depends on l because different harmonics in $\hat{\lambda}$ are resonant in different locations, as already shown. The above definition of $\delta_{e,l}$ also describes the width of the resonance in the thin island limit, $\delta_{e,l} \simeq \delta_e = \rho_e L_s/L_n$, when $m \longrightarrow 0$. In the case of a finite size island, when the resonance is very close to the separatrix, $\delta_{e,l}$ must be computed for m close to unity. In this case the function $M_0(m \longrightarrow 1) \simeq -(2/\pi^2)(\log 2)^2\,(1-m)\log(1-m)$ strongly depends on position and it vanishes for $m = 1$. Because the resonances are close to the separatrix, a finite size island has the effect of drastically contracting each of the resonance widths into an extremely thin layer close to the island separatrix.

Another effect of the presence of a finite size island is the mode coupling. The sum over the l-harmonics of the double integral in $d\hat{\lambda}$ indicates that the mode k_y couples with several harmonics in $\hat{\lambda}$. The number of relevant $\hat{\lambda}$-harmonics is determined by the width of each resonance $\delta_{e,l}$ and by the couplings.
Close to the island the ratio $M_1/M_0 \simeq 2K(m)$. Equation (7.43) for $m \longrightarrow 1$ yields

$$\frac{M_1}{M_0} \simeq -\sqrt{2}\pi \frac{\omega^*}{\omega} \frac{x_0 L_n}{\rho_e L_s} \frac{l}{k}, \tag{7.50}$$

which can be used to rewrite Eq. (7.48) as

$$\Delta_e' = -i\frac{\sqrt{\pi}}{2d_e^2}\frac{\omega}{\omega^*} \oint \frac{d\hat{\lambda}}{2\pi} \oint \frac{d\hat{\lambda}'}{2\pi} \sum_l e^{-ik_y(y-y')+il(\hat{\lambda}-\hat{\lambda}')} \times$$
$$\delta_{e,l}\Big[\frac{k}{l} - \frac{\omega^*}{\omega}(1+\frac{\eta_T}{2}) + \frac{\pi}{\sqrt{2}}\eta_T\left(\frac{\omega^*}{\omega}\right)^2 \frac{x_0 L_n}{\rho_e L_s}\frac{l}{k}\Big]. \tag{7.51}$$

The above equation generalizes the collisionless tearing mode dispersion relation Eq. (7.46) to finite size island geometry. Three major effects are introduced. The first one is the drastic reduction of the resonance widths due narrowing of the resonance layers. The second effect is the mode coupling: a single Fourier harmonic in y couples with several field line harmonics. Finally, the contribution Δ_{e1}', which vanishes in the thin island limit, is finite in the presence of a finite size island.

7.6.3 Fluid-like region

The contribution Δ_s' to the dispersion relation Eq. (7.33) is determined by the fluid-like response in the region between the MHD region and the equilibrium island chain, far away from the resonance. In order to proceed in the solution we now have to make assumption about the imaginary part of the mode frequency. If $\omega_I \ll \omega_R$ then the normalized phase velocity is essentially real. In this case the response function $W(\zeta)$ can be expanded for small ζ, leading to the approximate expression for P_s

$$P_s(\zeta) \simeq 1 - \frac{\Omega^*}{\omega}. \tag{7.52}$$

The graph of $W(\zeta)$ for real ζ is plotted in Fig. 7.2.
Far away from the equilibrium island chain the effect of the curvature of field lines is negligible. As already stated earlier, in the limit $m \longrightarrow 0$ the Fourier expansion in $\hat{\lambda}$ harmonics reduces to the Fourier expansion in y harmonics. The normalized phase velocity is $\zeta \simeq \omega L_s/v_{th}k_y x$. Finally, we neglect k_y^2 with respect to ∂_x^2 in the Laplacian.

Both the electrostatic potential and the magnetic flux terms contribute to $E_{\|}$. The relevant equations for this region become

$$\begin{aligned} x\tilde{\psi}_k'' + \frac{\omega L_s}{v_A^2 k_y}\tilde{\phi}_k'' &= 0, \\ \delta_s^2\tilde{\phi}_k'' - \tilde{\phi}_k &= \frac{\omega L_s}{k_y}\frac{1}{x}\tilde{\psi}_k, \end{aligned} \tag{7.53}$$

where

$$\delta_s^2 \equiv \frac{\rho_s^2/2}{1-\omega^*/\omega}. \tag{7.54}$$

The constant ψ approximation amounts to taking $\tilde{\psi}_k \simeq \tilde{\psi}_\infty =$ constant on the right hand side of Eq.(7.53) (see also Chapter 3). Using the normalization $v = x\delta_s$, $y = \tilde{\phi}_k \omega L_s \tilde{\psi}_\infty / k_y \delta_s$, the contribution to the fluid-like region to the jump of the logarithmic derivative is written as

$$\Delta_s' = -\frac{x_A^2}{\delta_s^3}\int_0^\infty dv\,\frac{y''}{v} \tag{7.55}$$

where $x_A = \omega L_s / k_y v_A$, and $y(v)$ is determined by

$$y'' - y = \frac{1}{v} \tag{7.56}$$

with the boundary conditions $y(0) = y(\infty) = 0$. We have already met the same limit in Chapter 3.1.2 for the constant ψ approximation of the linear fluid equations in the case of small phase velocity. In particular, the limit $\gamma^2 v^2 \gg 1$ in Eq. (3.42) is equivalent to $\zeta \ll 1$, here. In this limit no reconnection mechanism is available—remember that there are no kinetic resonances in this region because of the cold ion limit—and the value of Δ_s' is zero. Thus, no contribution to the jump of the logarithmic derivative across the layer comes from the fluid-like region.

The same result is included, even if not stated, in [53]. In that paper ions have a finite temperature and an additional resonance is present. One of the cases treated in that paper is the cold ion limit. In this case the contribution to the Δ_{rl}' is treated analytically, except for the computation of the integral. Because the above equation has solution in terms of exponential integral functions, the computation of the integral can be performed. The result is that, also using the expressions given in [53], the contribution Δ_s' in fact vanishes.

As a possible extension to the present treatment we can recall the analysis done in Chapter 3.1.2. An approximate value for the Δ_s' in the case of large electron temperature is

$$\Delta_s' = -i\pi\frac{x_A}{\delta_s d_e}, \tag{7.57}$$

where ρ_s of Eq. (3.55) is replaced by δ_s. The factor $\sqrt{2}$ which divides ρ_s in δ_s is due to a different definition of the thermal velocity, while the factor $-i$ arises from the transformation from a Laplace transform to a Fourier transform in time, $s = -i\omega$. The contribution Δ'_s should be added to the electron contribution Eq. (7.51), and the full dispersion relation is

$$\begin{aligned} \frac{d_e^2}{\delta_e}\Delta' = -i\frac{\omega}{\omega^*} \quad & \Bigg\{ \frac{\pi}{\sqrt{2}}\sqrt{1-\frac{\omega^*}{\omega}} + \\ & \frac{\sqrt{\pi}}{2}\oint\frac{d\hat{\lambda}}{2\pi}\oint\frac{d\hat{\lambda}'}{2\pi}\sum_l e^{-ik_y(y-y')+il(\hat{\lambda}-\hat{\lambda}')} \times \\ & \frac{\delta_{e,l}}{\delta_e}\Big[\frac{k}{l} - \frac{\omega^*}{\omega}(1+\frac{\eta_T}{2}) + \frac{\pi}{\sqrt{2}}\eta_T\left(\frac{\omega^*}{\omega}\right)^2\frac{x_0}{\delta_e}\frac{l}{k}\Big]\Bigg\}, \end{aligned} \tag{7.58}$$

where $\delta_e = \lim_{m\to 0}\delta_{e,l} = \rho_e L_s/L_n$.

7.7 Discussion

The kinetic model derived in Chapter 5 is used to study reconnection in non-isothermal plasmas. The stability of a finite size island chain is addressed using a method that is an extension of the approach in [12]. The employment of a reference system in which field lines are straight allows for a Fourier expansion along field line of the governing kinetic equations. The effects of the finite island equilibrium are then described via a generalized parallel wave number that is a flux function. The resulting system of equations is solved using an asymptotic method, similar to the method employed in [53]. With respect to that paper, the inclusion of the two dimensional equilibrium is the relevant extension.

The presence of the finite size island chain induces a mode coupling between Fourier harmonics along field lines. The extension of the coupling is basically determined by the widths of the resonances $\delta_{e,l}$. These widths vary strongly with position (and hence with l) close to the island and vanishes at the separatrix. Compared to the resonance width in the limit of a thin island, these widths are drastically reduced. This is a consequence of a factual narrowing of the resonant region induced by the presence of the equilibrium island.

An additional effect of the more general equilibrium is that a contribution proportional to the temperature gradient is included which vanishes in the thin island limit.

Concrete calculation of ω from the dispersion relation Eq. (7.58) are not given here. Hence, this chapter does not offer a conclusive statement concerning the overall stability of the island chain, mainly due to the non trivial way in which

$\delta_{e,l}$ depends on the Fourier index l. Nevertheless it can be concluded that the narrowing of the resonance widths induced by the island chain tends to enhance the growth rate of the collisionless tearing mode.

8. Conclusions

8.1 Fluid and kinetic descriptions

Magnetic reconnection has been widely invoked to account for fast release of energy accompanied by magnetic topology rearrangements. Solar flares, earth magneto-tail activity, and tokamak disruptions are but three most notorious and spectacular examples. Magnetic reconnection is a local violation of flux conservation which binds together the dynamical evolution of field lines and plasma. Depending on local temperature and density values, magnetic reconnection can be allowed by altogether different mechanisms, leading to peculiar structure formations and time scales. It was the quest for understanding of rapid phenomena as flares or disruptions which forced to abandon explanations based on resistive effects and to turn toward collisionless mechanisms. The possible mechanism examined in this thesis are electron inertia in the parallel motion, resistivity (mainly as a comparative case), and wave particle effects. Accordingly, the reconnection is said to be Hamiltonian, resistive or collisionless, respectively.
In the first part of the thesis a two fluid model has been employed to study Hamiltonian reconnection in isothermal plasmas, where the physical mechanism is provided by electron inertia while the drive is either an external forcing or an instability. The governing equations can be written in Lagrangian form, where two generalized fluxes are passively advected by the velocity fields generated by the corresponding streaming potentials. Both fluxes and potentials are combinations of the magnetic flux and the electrostatic potential and their Laplacian's, the current and the vorticity. The reconnection process violates flux conservation on scale lengths of the order of the electron inertia skin depth, in this way affecting the topology of the magnetic field. The time scales of the process depend on the ratio between the electron inertia skin depth and the ion sound Larmor radius. At the same time, the conservative dynamical evolution of the generalized fluxes shapes the structures of current density and vorticity. Peculiar cross shaped structure are formed in the proximity of the X point where most of the energy is concentrated in the form of electron kinetic energy, *i.e.* carried by the current. A novel feature extensively analyzed in this thesis is the formation of sub-layer structures whose dimensions can drop well below the electron inertia scale length. These structures, present in both forced and unstable cases, are also related with the advection of the generalized fluxes, and can lead to a faster than exponential scale collapse.

Plasmas in tokamaks or in the chromosphere of the sun cannot be realistically considered to have a distribution of temperature that is independent of space. However, the presence of a strong magnetic field introduces spatial anisotropy, in particular hindering the perpendicular energy transport, while the temperature along each field line is almost constant. But reconnection merges field lines extending into distant plasma regions, thus with possibly finite temperature differences. If the isothermal constrain is released, then a collisionless description of the plasma requires the use of kinetic equations. The kinetic equations cover all the range of possible phase velocity of the fluctuations, while fluid models are confined to either isothermal or adiabatic limits. In between the two fluid regimes lie wave-particle resonance effects. It is shown in the second part of this thesis that wave particle effects are responsible for violation of flux conservation.

The reconnection due to kinetic effects is referred to with the more general name of collisionless reconnection. Wave-particle effects cannot be included in conservative form. Hence, the system of equations describing collisionless reconnection, in contrast with the Hamiltonian one, it is not time reversible.

8.2 Results presented in this thesis

In the first part of this thesis the reconnection process in isothermal, collisionless plasmas has been described. A heuristic measure for the jump of the logarithmic derivative of the magnetic flux across the reconnection layer analogous to the linear Δ' has been introduced. This nonlinear Δ', denoted by $\Delta'_{nl}(t)$, has been shown to be a proper tool for the description of different phases of the nonlinear evolution of the reconnection process, from the forcing phase, through the island saturation, and until a quasi-stationary oscillatory regime is attained. Moreover, different values of Δ'_{nl} have been related to different mode structures and reconnection rates.

The dynamics of the reconnection process has been explained in terms of generalized fluxes. In the forced case, the walls displacement drives the advection of the fluxes by the corresponding stream velocities. As a consequence the generalized fluxes pile up along the symmetry line of the correspondent stream functions. The gradients in the generalized fluxes overlap to form the cross shaped structures which are observed in the numerically obtained current density and vorticity.

From the point of view of the energy balance, the Hamiltonian reconnection process in the forced case is driven essentially by an exchange between magnetic and electron kinetic energy. Despite the fact that the forcing lasts for a finite interval of time, a static state is not reached. On the contrary, an apparently periodic $E \times B$ flow sustains the oscillation of the island width around a finite value.

A novelty of Hamiltonian reconnection are sub-layer structures which develop close to the X point in the nonlinear stage of the reconnection process. These structures have length scales much smaller than any other one in the model, and they have been found to evolve at a faster than exponential rate. The process has the features of a scale collapse. An example of these structures is a current spike located at the X point. This scale collapse close to the X point has been shown to be a consequence of the superposition of strong gradients in the generalized fluxes in a same region of space, due to symmetry of the excitations. When the superposition is avoided the island saturation can be reached without the presence of spikes in the current density.

The characteristics of Hamiltonian reconnection has been proved to be largely independent from the drive of reconnection in the comparison between the forced and the unstable cases. Despite the difference in the reconnection drive, the topology of the solutions close to the X point is found to be the same in both cases. This similarity goes as far as including even the formation of sub-layer structures close to the X point, their length scales and their time evolution.

The kinetic model that has been used in the second part of this thesis is a generalization of the fluid model used in the first part. Taking moments of the kinetic equation and restricting to the isothermal limit yields the fluid model.

The kinetic model has been applied to steady state reconnection in an X point configuration, where it has been shown how a space-dependent temperature $T(x, y)$ in the inflowing plasma leads to a perturbation of the electromagnetic potentials in the outflow regions.

Wave-particle effects in the reconnection process have been studied in the linear limit. In contrast with Hamiltonian or resistive reconnection processes, wave-particle resonance effects take place in locations where the parallel wave vector is small but non-vanishing. Wave-particle resonance effects violate the frozen in law for the magnetic flux, and they allow reconnection to occur. The location in space of the resonances depends on the mode wave vector. When the resonance layer is located far from the island chain a single harmonic treatment of the resonance is possible. In this case the results of the well known ”thin island” approximation are recovered: an unstable mode exists which has frequency close to the diamagnetic frequency and growth rate proportional to the square of the electron inertia skin depth. In the opposite case of a large equilibrium island chain, or when the resonance layer is close to the island separatrix, modes becomes strongly coupled over a wide range of wave numbers.

In this thesis a model is used which includes the effects of the two-dimensionality of the equilibrium and keeps the resonance effects. It is found that the real part of the mode frequency is basically determined by diamagnetic effects, while the imaginary part is strongly affected by the coupling between different harmonics along field lines due to the presence of the finite size island chain. For perturbations with wavelength comparable with the island dimensions, those terms in the dispersion relation which are responsible for the instability in the thin island approximation are enhanced by the narrowing of the resonance of each coupled mode due to the presence of the finite size island chain.

8.3 Outlook

The kinetic model employed in this thesis keeps the compactness of its fluid counterpart, including some of the geometrical properties. The same compactness is kept by including the third spatial dimension. This allows for straightforward extensions of the work presented here, also due to the fact that numerical experiments are easily implementable.

By the large, fluid models are derived from kinetic models by taking moments over velocity space. An infinite hierarchy of coupled equations is then obtained. The hierarchy is broken by specifying the highest moment as a function of the lower ones. It is still a matter of discussion why exactly wave-particle effects are lost in these manipulations [54]. One opinion is that wave-particle effects are lost in a fluid closure because the number of moments that are used to approximate the distribution function—generally three—are too few. A different opinion is that the operation of taking moments is basically an average over the fluid velocity which intrinsically eliminate the resonances, no matter how many moments are kept. From this point of view the resonance is lost because only the principal value of the resonance integral is reproduced by the moments. Attempts to verify these statements reached the considerable number of thirty moments without solving the issue.

The question is most striking for collisionless system. Indeed, if collisions are important one can make the key assumption that the distribution function will never be too far from a Maxwellian, and than use this information in order to break the fluid hierarchy. This is the core of the derivation of the celebrated Braginskii two fluid model [1], used also in the first part of this thesis. But in a collisionless case the information about the actual form of the distribution function is not enough to determine which is the nonlinear response to arbitrary perturbations. That is why it is interesting and useful to have two descriptions, one fluid and one kinetic, of the same physical systems, as it is the case of the drift-Alfvén models used in this thesis.

Our two models can be used, among other things, as a playground for testing different fluid closures which include wave-particle resonance effects in some form. Attempts of repairing the deficiency of fluid models are many. Examples are the inclusion in the fluid equations of dissipative-like terms which approximately reproduce wave-particle effects, see [55] and reference therein; or the phase-velocity transform developed in Ref. [56], where instead of the two independent Fourier

transforms (in time and in space) which together build the mode phase velocity, the perturbation is directly transformed in harmonics of the phase velocity itself. The kinetic and fluid equations used in this thesis give ideal instruments for checking these models and techniques.
Last but not least, first experimental results [57] of collisionless reconnection in under dense plasmas with a magnetic cusp open the question about which one of the collisionless mechanism is dominant, whether the Hamiltonian or the wave-particle resonance one. The fluid and kinetic models here analyzed are the basis to develop the instruments to discriminate between the two mechanisms.

Appendices

A. Collisional fluid model

In this appendix a derivation of a model for the electron fluid is presented which includes the energy equation, the dependence on the z coordinate, and collisions. The starting point is the collisional fluid model derived by Braginskii [1]. The adopted ordering is the same of Chapter 2. Additionally, the limit of low collisionality of the fluid model is studied and discussed.

A derivation of the fluid equations of Chapter 2 from a kinetic equation is presented in Chapter 5.

A.1 Transport coefficients

The set of equations is given by the continuity and the momentum balance equations, Eqs. (2.1, 2.3), together with the energy balance equation

$$\frac{3}{2}n\left(\partial_t + \mathbf{v}\cdot\nabla\right)T + nT\nabla\cdot\mathbf{v} = -\nabla\cdot\mathbf{q} - Q - \mathbf{\Pi}\cdot\nabla\mathbf{v}.$$

The expression for the transport coefficients in the strong magnetic field limit are [1]

$$\begin{aligned}
\Pi_{xx} &= -\frac{\eta_0}{2}W_+ - \frac{\eta_1}{2}W_- - \eta_3 W_{xy}\\
\Pi_{yy} &= -\frac{\eta_0}{2}W_+ + \frac{\eta_1}{2}W_- + \eta_3 W_{xy}\\
\Pi_{zz} &= -\eta_0 W_{zz}\\
\Pi_{xy} &= \Pi_{yx} = -\eta_1 W_{x,y} + \frac{\eta_3}{2}W_-\\
\Pi_{xz} &= \Pi_{zx} = -\eta_2 W_{xz} - \eta_4 W_{yz}\\
\Pi_{yz} &= \Pi_{zy} = -\eta_2 W_{yz} + \eta_4 W_{xz},
\end{aligned} \tag{A.1}$$

in which

$$\begin{aligned}
W_{ij} &= \partial_i v_j + \partial_j v_i - \delta_{ij}\frac{2}{3}\nabla\cdot\mathbf{v},\\
W_+ &= W_{xx} + W_{yy} = -W_{zz} = 2\left[(\nabla_\perp\cdot\mathbf{v}) - \frac{2}{3}\nabla\cdot\mathbf{v}\right],\\
W_- &= W_{xx} - W_{yy} = 2\left[(\partial_x v_x - \partial_y v_y)\right],
\end{aligned} \tag{A.2}$$

and

$$\mathbf{R} = ne\left(\frac{\mathbf{J}_\parallel}{\sigma_\parallel} + \frac{\mathbf{J}_\perp}{\sigma_\perp}\right) - c_{T0}nT\nabla_\parallel \ln T - c_{T1}nT\varepsilon_f\frac{\mathbf{B}}{B}\times\nabla\ln T$$

$$\begin{aligned}\mathbf{q} &= c_{T0}nT\mathbf{v}_\parallel + c_{T1}nT\varepsilon_f\frac{\mathbf{B}}{B}\times\mathbf{v}_\perp - \kappa_\parallel\nabla_\parallel T - \kappa_\perp\nabla_\perp T - \\ &\qquad\qquad \kappa_\times(\frac{\mathbf{B}}{B}\times\nabla_\perp T) \\ Q &= -3nT\Omega\frac{m_e}{m_i}\varepsilon_f(1-\frac{T_i}{T}) - \mathbf{R}\cdot\mathbf{v}\end{aligned} \tag{A.3}$$

where

$$\begin{array}{llll} \eta_0 = c_0 nT/\varepsilon_f\Omega & c_0 = 0.73 & & c_{T0} = 0.71 \\ \eta_1 = c_1 nT\varepsilon_f/\Omega & c_1 = 0.51 & & c_{T1} = 3/2 \\ \eta_2 = c_2 nT\varepsilon_f/\Omega & c_2 = 4c_1 & \kappa_\parallel = c_\parallel nT/\varepsilon_f m\Omega & c_\parallel = 3.16 \\ \eta_3 = -c_3 nT/\Omega & c_3 = 1/2 & \kappa_\perp = c_\perp nT\varepsilon_f/m\Omega & c_\perp = 4.66 \\ \eta_4 = c_4 nT/\Omega & c_4 = -2c_3 & \kappa_\times = c_\times nT/m\Omega & c_\times = 5/2, \end{array}$$

and $\sigma_\parallel = \sigma_\perp/c_1$, $\sigma_\perp = ne^2/m\nu_c$.

Three aspects must be noted. First and most important, the collisional closure by Braginskii introduces three different types of terms in the equations. Terms of the first type are proportional to the collision frequency, terms of the second type to the collision time, and those of the third type contain none of the two. In the limit of rare collisions that we want to address here, the latter are unaffected, while the terms containing the collision frequency vanish. Terms proportional to the collision frequency diverge in the low collisionality limit, and have to be discussed. These are terms contains η_0 and to $\kappa_\parallel$. Note that terms proportional to η_0 appears in all the three diagonal component of the stress tensor. Hence, terms that grows arbitrarily large in the collisionless limit can potentially appear in the equations for both the parallel and the perpendicular dynamics.

Second, the collision frequency that often appears in the formulae is not a constant but it is a function of local temperature and density. In order to keep track of that dependence the electron collision frequency is written as

$$\nu_c = \tilde{\nu_c} nT^{-\frac{3}{2}},$$

where $\tilde{\nu_c} = \lambda/3.44\ 10^5$ contains the Coulomb logarithm λ, and it is practically a constant. Because the density and temperature dependence of the transport coefficients will be accounted for explicitly, we find more practical to abandon the notation of Braginskii with η_i's, and to use the c_i's instead.

Third, the elements of the stress tensor as derived in [1] are written in a reference system whose z-axis is parallel to the direction of the local magnetic field. In our case z axis and direction of magnetic field do not coincide. Hence, after the simplifications allowed by our ordering, a change of reference system is needed.

In the next section the final equations are presented. The discussion on the colisionless limit is presented in Section A.3

A.2 Collisional electron equations

In order to give proper account of the collision terms it is opportune to introduce an explicit ordering for the collision frequency. The ratio between perpendicular and parallel length scales is small, $L_\perp/L_\parallel \sim \varepsilon \ll 1$. We order the collision electron frequency ν_c to be of second order with respect to the electron gyrofrequency,

$$\varepsilon_f \equiv \frac{\nu_c}{\Omega_e} \sim \varepsilon^2. \tag{A.4}$$

In a reference system whose z-axis is parallel to the local magnetic field, the expressions for the transport coefficients to leading order in ε are

$$\begin{aligned}
R_z &= -c_1 m\tilde{\nu}_c \frac{n^2}{T^{3/2}} v_z - c_{T0} n(\partial_z T)\\
(\nabla\cdot\Pi)_z &= -\frac{p}{\Omega}\left\{\frac{c_0}{T^{5/2}\varepsilon_f}\partial_z(T^{5/2}W_+) + c_4[\ln p, v_z]\right\},\\
(\nabla\cdot\Pi)_\perp &= -\frac{p}{\Omega}\frac{c_0}{\varepsilon_f}\frac{1}{2T^{5/2}}\nabla_\perp(T^{5/2}W_+)\\
\mathbf{\Pi}\cdot\nabla\mathbf{v} &= -\frac{p}{\Omega}\frac{c_0}{\varepsilon_f}\frac{3}{4}T^{5/2}W_+^2\\
\nabla\cdot\mathbf{q} &= c_{T0}\partial_z(pv_z) - \frac{p}{m\Omega}\left\{\frac{c_\parallel}{\varepsilon_f}\frac{2}{7}\partial_z^2 T^{7/2} + c_\times[T, \ln p]\right\}\\
Q &= c_1 m\tilde{\nu}_c \frac{n^2}{T^{3/2}} v_z^2 + c_{T0} n v_z \partial_z T.
\end{aligned}$$

The above quantities can be rewritten in the laboratory reference system using the following transformation

$$\begin{aligned}
\partial_z &\longrightarrow \partial_z + (\mathbf{e}_z\times\nabla\psi)\cdot\nabla_\perp + \mathcal{O}(\varepsilon^2)\\
\nabla_\perp &\longrightarrow \nabla_\perp + \mathcal{O}(\varepsilon^2)
\end{aligned}$$

for the derivation operators, and

$$(\nabla\cdot\mathbf{\Pi})_z \longrightarrow (\nabla\cdot\mathbf{\Pi})_z + (\mathbf{e}_z\times\nabla\psi)\cdot(\nabla\cdot\mathbf{\Pi})_\perp + \mathcal{O}(\varepsilon^2)$$

for the parallel component of the divergence of the stress tensor.
The perpendicular component of the velocity is given by

$$\mathbf{v}_\perp = \mathbf{e}_z\times\nabla\phi - \frac{c}{enB_0}\mathbf{e}_z\times\nabla(p - \frac{1}{2}\frac{c_0}{\tilde{\nu}_c}T^{5/2}W_+) + v_z\mathbf{e}_z\times\nabla\psi. \tag{A.5}$$

This equation contains the viscous contribution as it arises formally by applying the ordering to the model of Braginskii. However, this equation is physically

inconsistent in the low collisionality limit. The viscous contribution in the perpendicular motion grows arbitrarily large for smaller and smaller ν_c. There is no term that can possibly balance such an explosive contribution to Eq. (A.5). Eventually, this term will become even larger than the $E \times B$ term, factually violating the hypothesis of magnetized plasma. No sensible interpretation can be given of such a behaviour of the perpendicular dynamics in the collisionless limit. Hence, on physical basis, we must discard the viscous term and take for $\mathbf{v}_\perp$ the expression in Eq. (2.5). The inconsistency we are facing here is to be related to the collisional nature of the transport coefficient derived in [1], as explained in details below.
The ratio between the $\mathbf{\Pi} \cdot \nabla \mathbf{v}$ and the parallel conductivity term in $\nabla \cdot \mathbf{q}$ is independent of collision frequency, and it is of the order of

$$\frac{c_0}{c_\parallel} \frac{W_+ T^{7/2}}{v_{th}^2 \nabla_\parallel^2 T^{7/2}} \sim \left(\frac{v_z}{v_{th}}\right)^2 \ll 1. \tag{A.6}$$

Hence we neglect the contribution coming from $\mathbf{\Pi} \cdot \nabla \mathbf{v}$ with respect to the parallel conductivity term in the energy balance equation.

The derivation of the system of equations for the electron fluid follows the same procedure as in Section 2.1.1. The equations governing the electron fluid in the collisional limit are

$$D_t n + \nabla_\parallel (n v_z) = 0, \tag{A.7}$$

$$\begin{aligned} D_t(\psi + \frac{v_z}{\Omega}) + \frac{1}{mn\Omega} \nabla_\parallel p - \partial_z \phi = \\ -\frac{c_0}{m\Omega^2 T^{3/2}} \frac{1}{\varepsilon_f} \nabla_\parallel (T^{5/2} W_{zz}) - c_1 \varepsilon_f v_z - c_{T0} \frac{cT}{eB_0} \nabla_\parallel T, \end{aligned} \tag{A.8}$$

$$\begin{aligned} \frac{3}{2} D_t T + \frac{3}{2} v_z \nabla_\parallel T + T \nabla_\parallel v_z = \\ -c_{T0} \frac{T}{n} \nabla_\parallel (n v_z) + \frac{2 c_\parallel}{7 m\Omega T^{3/2}} \frac{1}{\varepsilon_f} \nabla_\parallel^2 T^{7/2} + c_1 \Omega m \varepsilon_f v_z^2. \end{aligned} \tag{A.9}$$

These equations are written in the same laboratory reference system used in Chapter 2, *i.e.* the subscript $\|$ is referred to the magnetic field and z to the direction of the vector $\mathbf{e}_z$. In particular, the parallel gradient is given by $\nabla_\parallel \; = \partial_z \; + [\psi, \quad]$, and $W_{zz} = -(2/3)(\nabla \cdot \mathbf{v} - 3 \nabla_\parallel v_z)$.
The gyroviscous cancellation in the momentum balance equation is correctly recovered. An additional cancellation occurs in the energy balance equation and it involves the term proportional to $c_\times$ in $\nabla \cdot \mathbf{q}$.

A.3 Formal limit of low collisionality

We now discuss the above model in the limit of rare collisions. As anticipated above, attention must be paid to those terms that grows arbitrarily large for smaller and smaller values of the collision frequency.

The continuity equation does not include any collisional term and it remains unchanged in the collisionless limit. Consider the energy balance equation. The only term left which diverges for $\varepsilon_f \longrightarrow 0$ leads to the relation

$$\nabla_{\|}^2 T^{7/2} = 0, \tag{A.10}$$

which comes from the parallel conductivity term, and it is satisfied for modes with phase velocity $\omega/k_{\|}$ such that $(k_{\|} v_{th})^2 \gg \omega\nu_c$. Equation (A.10) can be integrated. If the boundary conditions contains no heat sources or sinks it is $\nabla_{\|} T = 0$. This equation is used instead of the energy balance equation in Chapter 2. As a consequence, also the term proportional to c_{T_0} and independent of collisions in the momentum balance equation vanishes. The isothermal motion of electrons along field lines is expected to occur in the collisionless regime, as electrons have no constrains to the parallel streaming.

The momentum balance equation contains also a viscous term. The conditions on the mode phase velocity which simplifies the energy balance equation implies that the viscous contribution in the momentum balance equation is large compared with electron inertia. Hence, the very same condition on the phase velocity of the mode that leads to a correct physical picture in the energy balance equation gives at the same time an unphysical divergent term in the momentum balance equation.

The limit of low collisionality of the equations as derived from the Braginskii model presents some difficulties. These are related to the fact that high collisionality is a crucial hypothesis in that model. In particular, for short time scales it is not possible to consider the pressure to be isotropic, and separate equations of state for parallel and perpendicular temperature must be given. In the model by Braginskii the time scale of the phenomena of interest is longer than the collision time scale, and length scales are larger than the mean free path. This is the reason why the collisionless limit can be taken only formally.

Alternatively, one can formally eliminate all the terms coming from the Braginskii collisional closure but at the same time retain the gyroviscous cancellation. This is done by setting $c_0 \longrightarrow 0$. The set of equations for the electron fluid reads

$$\begin{aligned} D_t n + \nabla_{\|}(n v_z) &= 0 \\ D_t(\psi + \frac{v_z}{\Omega}) - \partial_z \phi - \frac{\nabla_{\|} p}{m n \Omega} &= 0 \\ \nabla_{\|} T &= 0 \end{aligned}$$

which are the equations for the electron fluid used in Chapter 2 in the limit of negligible resistivity.

However, the isothermal model used in the first part of this thesis can be derived from the kinetic equation, as it is shown in Chapter 5. A formal connection between derivations from the fluid and kinetic theories is made.

B. The metric tensor $\mathbf{g}(\hat{\psi}, \hat{\lambda})$

In this appendix the Fourier coefficients in $\hat{\lambda}$ of the metric tensor for the straight field line coordinate system transformation are derived.

B.1 Notation

In the following, the parameter m defined in Eq. (7.3) is not written explicitly in elliptic functions and integrals, ***e.g.***, $\mathrm{dn}\, u \equiv \mathrm{dn}(u|m)$, $E \equiv E(m)$, and $K \equiv K(m)$. Furthermore we define $m_1 \equiv 1 - m$ and introduce the nome

$$q \equiv e^{-\pi K(m_1)/K(m)}.$$

For later use we need the derivatives

$$\frac{dq}{dm} = \frac{\pi^2 q}{4K^2 m m_1}, \quad \frac{dK}{dm} = \frac{E - m_1 K}{2 m m_1}, \quad \frac{dE}{dm} = \frac{E - K}{2m},$$

for later use. Although we use the coordinate $\hat{\lambda}$, and seek Fourier series in terms of this variable, we will continue to use the argument u defined in Eq. (7.10) in elliptic functions and integrals. A prime denotes the derivative with respect to u. Thus we can use the standard formulas for elliptic functions, ***e.g.***, $\mathrm{dn}' u = -m\ \mathrm{sn}\, u\ \mathrm{cn}\, u$. Note that

$$\sin(y/y_0) = \mathrm{sn}(u|m), \tag{B.1}$$

$$\cos(y/y_0) = \mathrm{cn}(u|m), \tag{B.2}$$

$$x/x_0 = m^{-1/2}\ \mathrm{dn}(u|m). \tag{B.3}$$

B.2 The metric coefficients

In order to solve Poisson's equation in the $(\hat{\psi}, \hat{\lambda})$ coordinate system, we set out to find explicit expressions for the metric tensor coefficients for these coordinates,

$$g^{\psi\psi} = |\nabla\hat{\psi}|^2, \quad g^{\psi\lambda} = \nabla\hat{\psi} \cdot \nabla\hat{\lambda}, \quad g^{\lambda\lambda} = |\nabla\hat{\lambda}|^2, \tag{B.4}$$

as Fourier series in $\hat{\lambda}$ with coefficients depending on ψ:

$$g^{ij}(\psi, \hat{\lambda}) = \sum_n g_n^{ij}(\psi) e^{in\hat{\lambda}}, \qquad i, j = \psi, \lambda. \tag{B.5}$$

The first coefficient, $g^{\psi\psi}$, poses no difficulty. Using the explicit expression for $\psi(x, y)$ in Eq. (7.6) and Eq. (B.3) one finds

$$\nabla\psi = 4\psi_r\Big(m^{-1/2}\,\mathrm{dn}\,u\frac{\nabla x}{x_0} - m^{-1}\,\mathrm{dn}'u\frac{\nabla y}{y_0}\Big), \tag{B.6}$$

and

$$\nabla\hat{\psi} = \frac{K}{\pi}\Big(\,\mathrm{dn}\,u\frac{\nabla x}{x_0} - m^{-1/2}\,\mathrm{dn}'u\frac{\nabla y}{y_0}\Big). \tag{B.7}$$

Next, $\nabla\hat{\lambda}$ must be determined from the expression (7.10) for $\hat{\lambda}(y, m)$. To this end, we need the derivative of the elliptic integral of the first kind with respect to the parameter m,

$$\partial_m F(y/y_0, m) = \frac{1}{2mm_1}\Big(Z(u) + (\frac{E}{K} - m_1)u + \frac{\mathrm{dn}'u}{\mathrm{dn}\,u}\Big), \tag{B.8}$$

where $Z(u)$ is Jacobi's Zeta-function. From Eq. (7.10) one can thus derive

$$\partial_y\hat{\lambda}(y, m) = \frac{\pi}{y_0 K}\mathrm{nd}\,u, \tag{B.9}$$

$$\partial_m\hat{\lambda}(y, m) = \frac{\pi}{2mm_1K}\Big(Z(u) + \frac{\mathrm{dn}'u}{\mathrm{dn}\,u}\Big). \tag{B.10}$$

From these two expressions we obtain

$$\begin{aligned}\nabla\hat{\lambda} &= (\partial_y\hat{\lambda})\nabla y + (\partial_m\hat{\lambda})\frac{dm}{d\hat{\psi}}\nabla\hat{\psi}\\ &= \frac{\pi\,\mathrm{nd}\,u}{K}\frac{\nabla y}{y_0} - \frac{\pi^2 m^{1/2}}{m_1K^2}\Big(Z(u) + \frac{\mathrm{dn}'u}{\mathrm{dn}\,u}\Big)\frac{\nabla\hat{\psi}}{x_0}\\ &= -\frac{\pi m^{1/2}}{m_1K}(Z(u)\ \mathrm{dn}\,u + \ \mathrm{dn}'u)\frac{\nabla x}{x_0}\\ &\quad + \frac{\pi}{m_1K}(Z(u)\ \mathrm{dn}'u + (2-m)\,\mathrm{dn}\,u - \ \mathrm{dn}^3u)\frac{\nabla y}{y_0}.\end{aligned} \tag{B.11}$$

In the metric tensor coefficients we distinguish terms according to their scaling with the island aspect ratio and define

$$g^{\psi\psi} = \frac{g_x^{\psi\psi}}{x_0^2} + \frac{g_y^{\psi\psi}}{y_0^2}. \tag{B.12}$$

$$g^{\psi\lambda} = \frac{g_x^{\psi\lambda}}{x_0^2} + \frac{g_y^{\psi\lambda}}{y_0^2}. \tag{B.13}$$

$$g^{\lambda\lambda} = \frac{g_x^{\lambda\lambda}}{x_0^2} + \frac{g_y^{\lambda\lambda}}{y_0^2}. \tag{B.14}$$

These terms are given by

$$
\begin{aligned}
g_x^{\psi\psi} &= \frac{K^2}{\pi^2}\,\mathrm{dn}^2 u, && \text{(B.15)}\\
g_y^{\psi\psi} &= \frac{K^2}{\pi^2 m}(\,\mathrm{dn}' u)^2, && \text{(B.16)}\\
g_x^{\psi\lambda} &= \frac{m^{1/2}}{m_1}(Z(u)\,\mathrm{dn}\,u + \,\mathrm{dn}' u)\,\mathrm{dn}\,u, && \text{(B.17)}\\
g_y^{\psi\lambda} &= \frac{\mathrm{dn}' u}{m_1 m^{1/2}}(Z(u)\,\mathrm{dn}' u + (2-m)\,\mathrm{dn}\,u - \,\mathrm{dn}^3 u), && \text{(B.18)}\\
g_x^{\lambda\lambda} &= \frac{\pi^2 m}{m_1^2 K^2}(Z(u)\,\mathrm{dn}\,u + \,\mathrm{dn}' u)^2, && \text{(B.19)}\\
g_y^{\lambda\lambda} &= \frac{\pi^2}{m_1^2 K^2}(Z(u)\,\mathrm{dn}' u + (2-m)\,\mathrm{dn}\,u - \,\mathrm{dn}^3 u)^2. && \text{(B.20)}
\end{aligned}
$$

B.3 Fourier series

We seek Fourier series in $\hat{\lambda}$ for these six terms. For the elliptic functions such as $\mathrm{dn}\,u$ and also for $Z(u)$, the Fourier series are the so-called q-series. The metric tensor coefficients, however, contain powers and products of elliptic functions. These must be expressed in terms of basic elliptic functions and their derivatives with respect to u and m (for which the q-series are known). Starting point is the q-series for the logarithm of Jacobi's ϑ-function,

$$
\ln\Big(\frac{\vartheta_4(\frac{1}{2}\hat{\lambda}, q)}{\vartheta_4(0,q)}\Big) = \sum_{n\neq 0} \frac{1}{n}\frac{1-e^{in\hat{\lambda}}}{q^{-n}-q^{n}} \tag{B.21}
$$

where the sum is over all non-zero integers. Differentiation with respect to u yields the q-series for Jacobi's Zeta-function,

$$
\begin{aligned}
Z(u) &= \partial_u \ln \vartheta_4\\
&= \frac{\pi}{iK}\sum_{n\neq 0}\frac{e^{in\hat{\lambda}}}{q^{-n}-q^{n}},
\end{aligned} \tag{B.22}
$$

Differentiating once more with respect to u yields

$$
\begin{aligned}
\mathrm{dn}^2 u &= \frac{E}{K} + Z'(u)\\
&= \frac{E}{K} + \frac{\pi^2}{K^2}\sum_{n\neq 0}\frac{n e^{in\hat{\lambda}}}{q^{-n}-q^{n}},
\end{aligned} \tag{B.23}
$$

The derivative of this expression is

$$\begin{aligned}2\,\mathrm{dn}\,u\;\mathrm{dn}'u &= (\,\mathrm{dn}^2u)'\\ &= i\frac{\pi^3}{K^3}\sum_{n\neq 0}\frac{n^2e^{in\hat{\lambda}}}{q^{-n}-q^n}.\end{aligned}\tag{B.24}$$

The q-series for $(\,\mathrm{dn}'u)^2$ can be derived as follows. The elliptic function $\mathrm{sn}\,u$ satisfies the differential equation

$$(\,\mathrm{sn}'u)^2 = (1-\,\mathrm{sn}^2u)(1-m\;\mathrm{sn}^2u).$$

Differentiating this expression once more and using the relation $\mathrm{dn}^2u = 1 - m\;\mathrm{sn}^2u$, one arrives at

$$\begin{aligned}(\,\mathrm{dn}'u)^2 &= (2-m)\,\mathrm{dn}^2u-\,\mathrm{dn}^4u-m_1\\ &= \frac{1}{6}(\,\mathrm{dn}^2u)''+\frac{1}{3}(2-m)\,\mathrm{dn}^2u-\frac{2}{3}(1-m)\\ &= \frac{1}{3}(2-m)\frac{E}{K}+\frac{1}{3}(2-m)\frac{\pi^2}{K^2}\sum_{n\neq 0}\frac{ne^{in\hat{\lambda}}}{q^{-n}-q^n}\\ &\quad -\frac{2}{3}(1-m)-\frac{1}{6}\frac{\pi^4}{K^4}\sum_{n\neq 0}\frac{n^3e^{in\hat{\lambda}}}{q^{-n}-q^n}.\end{aligned}\tag{B.25}$$

In order to find Fourier series for the products of $Z(u)$ and $Z^2(u)$ with elliptic functions, we define the partial derivative with respect to m at constant $\hat{\lambda}$,

$$D_m = \frac{\partial}{\partial m}\Big|_{\hat{\lambda}},$$

which does not commute with the u-derivative,

$$[D_m,\partial_u] = \frac{m_1-E/K}{2mm_1}\partial_u.$$

Using the partial differential equation for ϑ-functions,

$$D_m\vartheta_4 = -\frac{1}{4mm_1}\partial_u^2\vartheta_4,$$

we can take the D_m-derivative of Eq. (B.21),

$$D_m\ln\Big(\frac{\vartheta_4(\frac{1}{2}\hat{\lambda},q)}{\vartheta_4(0,q)}\Big) = -\frac{1}{4mm_1}(Z^2(u)+\,\mathrm{dn}^2u-1).\tag{B.26}$$

The correctness of the constant term -1 in this expression is seen by noting that both sides of the equation vanish for $\hat{\lambda} = 0$. Equation (B.26) provides the q-series for $Z^2(u)$,

$$\begin{aligned} Z^2(u) = &- \mathrm{dn}^2 u - \frac{m-2}{3} \\ &+ \frac{\pi^2}{K^2}\Big(\frac{1}{12} + \sum_{n\neq 0} \frac{q^{-n}+q^n}{(q^{-n}-q^n)^2} e^{in\hat{\lambda}}\Big). \end{aligned} \tag{B.27}$$

In establishing the terms constant in u in this result, we have used the identity

$$\sum_{n\neq 0} \frac{q^{-n}+q^n}{(q^{-n}-q^n)^2} = \frac{1}{3}(1+m)\frac{K^2}{\pi^2} - \frac{1}{12},$$

which can be obtained as the D_m derivative of the equation

$$\sum_{n=1}^{\infty} \frac{1/n}{q^{-n}-q^n} = \sum_{n=1}^{\infty} \ln(1+q^n) = \frac{1}{24}\ln\Big(\frac{m}{16 m_1^2 q}\Big).$$

Here, the equality of the first two expressions follows by considering their Taylor-series in q^n and interchanging the double summations. The second equality follows from the infinite product representation of ϑ_4, equating it to 1 at $u = 0$. Differentiating Eq. (B.26) with respect to u one obtains

$$\begin{aligned} D_m Z(u) &= \frac{1}{2mm_1}\Big((m_1 - \frac{E}{K} - Z'(u))Z(u) - \frac{1}{2}Z''(u)\Big) \\ &= -\frac{1}{2mm_1}\Big((\mathrm{dn}^2 u - m_1)Z(u) + \mathrm{dn}\, u\ \mathrm{dn}' u\Big). \end{aligned} \tag{B.28}$$

Differentiating with respect to u, one obtains

$$D_m\, \mathrm{dn}\, u = -\frac{1}{2mm_1}(Z(u)\, \mathrm{dn}' u + \mathrm{dn}\, u - \mathrm{dn}^3 u). \tag{B.29}$$

Differentiating once more yields

$$D_m\, \mathrm{dn}' u = -\frac{1}{2mm_1}(Z(u)\, \mathrm{dn}'' u + (m - 2\,\mathrm{dn}^2 u)\, \mathrm{dn}\, u). \tag{B.30}$$

In order to reduce the $Z^2(u)\, \mathrm{dn}^2 u$ term in $g_x^{\lambda\lambda}$, we need

$$\begin{aligned} D_m(Z^2(u) + \mathrm{dn}^2 u) &= \\ -\frac{1}{mm_1}\Big(& (\mathrm{dn}^2 u - m_1)Z^2(u) + \mathrm{dn}^2 u \\ & +2\ \mathrm{dn}\, u\ \mathrm{dn}' u\, Z(u) - \mathrm{dn}^4 u\Big), \end{aligned} \tag{B.31}$$

and in order to reduce the $Z^2(u)(\,\mathrm{dn}'u)^2$ term in $g_y^{\lambda\lambda}$, we need the expression

$$\begin{aligned} D_m(Z(u)\ \mathrm{dn}\,u\ \mathrm{dn}'u) &= \\ &-\frac{1}{2mm_1}\Big(\ (Z^2(u)+\ \mathrm{dn}^2u)(\,\mathrm{dn}'u)^2 \\ &\qquad +2(m-\ \mathrm{dn}^2u)\,\mathrm{dn}\,u\ \mathrm{dn}'u\,Z(u)\Big), \end{aligned} \tag{B.32}$$

One obtains the metric coefficients

$$g_x^{\psi\psi} = \frac{EK}{\pi^2}+\sum_{n\neq 0}\frac{ne^{in\hat{\lambda}}}{q^{-n}-q^n}, \tag{B.33}$$

$$\begin{aligned} g_y^{\psi\psi} &= \frac{m_1}{3\pi^2}\frac{d}{dm}((2-m)K^2) \\ &\quad +\frac{1}{3m}(2-m+\frac{1}{2}\partial_u^2)\sum_{n\neq 0}\frac{ne^{in\hat{\lambda}}}{q^{-n}-q^n}, \end{aligned} \tag{B.34}$$

$$g_x^{\psi\lambda} = 2m^2D_m\frac{i\pi}{m^{1/2}K}\sum_{n\neq 0}\frac{e^{in\hat{\lambda}}}{q^{-n}-q^n}, \tag{B.35}$$

$$\begin{aligned} g_y^{\psi\lambda} &= \frac{1}{3}\Big(2+m^2D_mm^{-1}\partial_u^2-2m(2-m)D_m\Big)\circ \\ &\qquad \frac{\pi}{iKm^{1/2}}\sum_{n\neq 0}\frac{e^{in\hat{\lambda}}}{q^{-n}-q^n}, \end{aligned} \tag{B.36}$$

$$g_x^{\lambda\lambda} = 4\frac{\pi^2m^3}{m_1K^2}D_mm_1D_m\sum_{n\neq 0}\frac{1}{n}\frac{1-e^{in\hat{\lambda}}}{q^{-n}-q^n} \tag{B.37}$$

$$\begin{aligned} g_y^{\lambda\lambda} &= \frac{\pi^2}{K^2}\Big(\frac{2}{3}m^2D_m^2(\,\mathrm{dn}^2u)+\ \mathrm{dn}^2u-\frac{1}{3}\frac{m}{m_1}Z^2(u), \\ &\qquad -\frac{2-m}{m_1}mD_m(\frac{1}{3}Z^2(u)+\ \mathrm{dn}^2u)\Big) \\ &= \frac{2}{3}\frac{\pi^2}{m_1K^2}\Big(mm_1(mD_m-2+m)D_m\ \mathrm{dn}^2u \\ &\qquad +(\frac{3}{2}-m)\ \mathrm{dn}^2u-\frac{1}{2}m \\ &\qquad +2m(1+(2-m)D_m)mm_1D_m\circ \\ &\qquad\quad \sum_{n\neq 0}\frac{1}{n}\frac{1-e^{in\hat{\lambda}}}{q^{-n}-q^n}\Big). \end{aligned} \tag{B.38}$$

which can be rewritten as explicit Fourier coefficients as

$$g_{l\neq 0}^{\hat{\psi}\hat{\psi}} = \frac{l}{q^{-l}-q^l}\left\{\frac{1}{x_0^2}+\frac{1}{3y_0^2m}\Big(2-m-\frac{\pi^2}{K^2}\frac{l^2}{2}\Big)\right\}$$

$$
\begin{aligned}
g^{\hat\psi\hat\psi}_{l=0} &= \frac{K^2}{\pi^2}\left\{\frac{1}{x_0^2}\frac{E}{K} + \frac{1}{3y_0^2 m}\Big((2-m)\frac{E}{K} - 2(1-m)\Big)\right\} \\
g^{\hat\lambda\hat\psi}_{l\neq 0} &= i\frac{\pi}{K}\frac{\sqrt{m}}{1-m}\frac{1}{q^{-l}-q^{l}} \times \\
&\quad \left\{\frac{1}{x_0^2}\Big[\frac{E}{K} - \frac{\pi^2}{2K^2} l T_l\Big] + \right. \\
&\quad \frac{1}{3y_0^2 m}\Big[(2-m)\frac{E}{K} - 2(1-m) - \frac{3}{2}\frac{\pi^2}{K^2}\frac{E}{K}l^2 - \\
&\quad \left. \frac{\pi^2}{2K^2} l T_l\Big(2-m-\frac{\pi^2}{2K^2}l^2\Big)\Big]\right\} \\
g^{\hat\lambda\hat\psi}_{l=0} &= 0 \\
g^{\hat\lambda\hat\lambda}_{l\neq 0} &= \frac{\pi^4}{K^4}\frac{m}{(1-m)^2}\frac{1}{q^{-l}-q^{l}} \times \\
&\quad \left\{\frac{1}{x_0^2}\Big[\frac{E}{K}T_l - \frac{\pi^2}{4K^2} l\Big(2T_l^2 - 1\Big)\Big] + \right. \\
&\quad \frac{1}{3y_0^2 m}\Big[-\frac{\pi^2}{K^2}\frac{l}{4}\Big(2-m-\frac{\pi^2}{2K^2}l^2\Big)\Big(2T_l^2-1\Big) + \\
&\qquad \left. 3\frac{E}{K}l + T_l\Big((2-m)\frac{E}{K} - 2(1-m) - \frac{3}{2}\frac{\pi^2}{K^2}\frac{E}{K}l^2\Big)\Big]\right\} \\
g^{\hat\lambda\hat\lambda}_{l=0} &= \frac{\pi^2}{3K^2}\frac{m}{(1-m)^2}\left\{\frac{1}{x_0^2}\Big[\frac{\pi^2}{4K^2}\frac{E}{K} - (1-m)\Big] + \right. \\
&\quad \frac{1}{m y_0^2}\Big[\frac{E^3}{K^3} + (1-m)(2-m) + \\
&\qquad \left. \frac{\pi^2}{12K^2}\Big((2-m)\frac{E}{K} - 2(1-m)\Big)\Big]\right\}. \qquad \text{(B.39)}
\end{aligned}
$$

where $q = \exp(-\pi K'/K)$, and $T_l(q) = (q^{-l} + q^{l})/(q^{-l} - q^{l})$. Note that

$$g^{\hat\psi\hat\psi}_{l} = g^{\hat\psi\hat\psi}_{-l}, \qquad g^{\hat\lambda\hat\psi}_{l} = -g^{\hat\lambda\hat\psi}_{-l}, \qquad g^{\hat\lambda\hat\lambda}_{l} = g^{\hat\lambda\hat\lambda}_{-l}. \qquad \text{(B.40)}$$

References

[1] S.I. Braginskii,*Transport processes in a plasma*, Review of Plasma Physics, vol. 1, M.A. Leontovich, Consultants Bureau, New York (1965) 205.

[2] H. Alfvén, C.G. Fälthammar *Cosmical electrodynamics* Oxford University Press (Great Britain 1963).

[3] R.B. White, *Theory of tokamak plasmas* North-Holland Physics (Amsterdam, 1989).

[4] T.J., Schep, Transaction of Fusion Technology **33**, vol. 2T, 39 (1998).

[5] H.P.Furth, J. Killeen, M.N. Rosenbluth, Phys. Fluids **6** 459 (1963).

[6] J. Wesson, Nucl. Fusion **30** 2545 (1990).

[7] V.M. Vasyliunas, Rev. Geophys. Space Phys. **13** 303 (1975).

[8] E.N. Parker, Astrophys. J. Suppl. **8** 177 (1963).

[9] D. Biskamp, *Nonlinear Magnetohydrodynamics*, Cambridge University Press (Great Britain 1993).

[10] B.B. Kadomstev, Sov. J. Plasma Phys., **1** 389 (1975).

[11] A.H. Glasser, Green, Johnson, Phys. Fluids **19** 567 (1976)

[12] B. Coppi, J. W-K. Mark, L. Sugiyama, and G. Bertin Phys. Rew. Lett. **42** 1058 (1979).

[13] B.N. Kuvshinov, F. Pegoraro, T.J. Schep, Phys. Lett. A **191** 296 (1994).

[14] T.J. Schep, F. Pegoraro, B.N. Kuvshinov, Phys. Plasmas **1** 2843 (1994).

[15] E. Cafaro, D. Grasso, F. Pegoraro, F. Porcelli, A. Saluzzi, Phys. Rev. Lett. **80** 4430 (1998).

[16] B.N. Kuvshinov, V.P. Lakhin, F. Pegoraro, T.J. Schep, J. Plasma Physics **59** 727 (1998).

[17] P.J. Morrison, R.D. Hazeltine, Phys. Fluids **27** 886 (1984).

[18] V.P. Lakhin, T. J. Schep, E. Westerhof, Phys. Plasmas **5** 3833 (1998).

[19] J. Bergmans, B.N. Kuvshinov, V.P. Lakhin, T. J. Schep, Phys. Plasmas **7** 2388 (2000).

[20] T.S.Hahm, R.M. Kulsrud, Phys. Fluids **28** 2412 (1985).

[21] Rem J., Schep T. J., Plasma Phys. and Control. Fusion **40** 139 (1998).

[22] G.E. Vekestein, R. Jain, Phys. Plasmas **5** 1506 (1998).

[23] G. Vekestein, Phys. Plasmas **7** 3808 (2000).

[24] R.D. Hazeltine, D. Ross, Phys. Fluids **21** 1140 (1978).

[25] R.D. Hazeltine, J.D. Meiss, *Plasma Confinement*, Addyson–Wesley Publishing Company (Amsterdam 1992).

[26] R.D. Hazeltine, J.D. Meiss, P.J. Morrison, Phys. Fluids **29** 1633 (1986).

[27] F. Porcelli, Phys. Rew. Lett. **66** 425 (1991).

[28] L. Zakharov, B. Rogers, S. Migliuolo Phys. Fluids. B **5** 2498 (1993).

[29] F. Pegoraro, T.J. Schep, Plasma Phys. Control. Fusion **28** 647 (1986).

[30] W. Magnus, F. Oberhettimger, F.G. Tricomi, *Tables of integrals transforms*, McGrow-Hill Book Company (New York, 1954), vol.I, pag. 233.

[31] Xiogang Wang, A. Bhattachatjee, Phys. Fluids B **4** 1795 (1992).

[32] M. Ottaviani, F. Porcelli, Phys. Rev. Lett. **71** 3802 (1993).

[33] M. Ottaviani, F. Porcelli, Phys. Plasmas **2** 4104 (1995).

[34] G. Valori, H.J. de Blank, J. Rem, T.J. Schep, *Proceedings of the Joint Varenna – Lausanne international workshop on "Theory of Fusion Plasmas"*, Varenna, 1998, (Editrice Compositori, Bologna, 1999), p. 555 .

[35] H.J. de Blank, J. Rem, G. Valori, in *Proceedings of the 25th European Conference on Controlled Fusion and Plasma Physic*, Praha 1998, Europ. Conf. Abs. Vol. 22C, p. 2188.

[36] J.G. Blom, R.A. Trompert, J.G. Verwer, ACM Trans. Math. Soc. **22** 302 (1996).

[37] A.Y. Aydemir, Phys. Fluids **4** 3469 (1992).

[38] D. Grasso, F. Califano, F. Pegoraro, F. Porcelli, Phys. Rev. Lett. **86** 5051 (2001).

[39] D. Grasso, F. Califano, F. Pegoraro, F. Porcelli, Plasma Phys. Rep. **26** 512 (2000).

[40] G. Valori, D. Grasso, H.J. de Blank, Phys. of Plasmas **7** 178 (2000).

[41] M. Ottaviani, F. Porcelli, Phys. Rew. Lett. **71** 3802 (1993).

[42] D. Grasso, F. Pegoraro, F. Porcelli, F. Califano, Plasma Phys. Control. Fusion **41**1497 (1999).

[43] K. Avinash, S.K. Bulanov, T. Esirkepov, P. Kaw, F. Pegoraro, P.V. Sasorov, A. Sen, Phys. Plasmas **5** 2849 (1998).

[44] M. Ottaviani, F. Porcelli, Phys. of Plasmas **2** 4104 (1995).

[45] H. A. Rose and P. L. Sulem, J. Phys. France **39** 441 (1978).

[46] F.L. Hinton, R.D. Hazeltine, Rev. Mod. Phys. **48** 239 (1976).

[47] B.B. Kadomtsev, O.P. Pogutse, JETP Lett. **39** 269 (1984).

[48] R.M. Kulsrud, *MHD description of plasma*, Handbook of Plasma Physiscs, vol. 1, M.N. Rosenbluth, R.Z. Sagdeev, North Holland Publishing Company, Amsterdam (1983), p. 115 .

[49] H.J. de Blank, Phys. of Plasmas **8** 3927 (2001).

[50] G. Valori, H.J. de Blank, T.J. Schep, in *Proceedings of the 27th European Physical Society Conference on Controlled Fusion and Plasma Physics*, Budapest, 2000 (European Physical Society, Mulhouse, France, 2000), ECA Voi. 24B.

[51] G. Valori, H.J. de Blank, T.J. Schep, *Proceedings of the Joint Varenna – Lausanne international workshop on "Theory of Fusion Plasmas"*, Varenna, 2000, (Editrice Compositori, Bologna, 2000), p. 381.

[52] G. Valori, H.J. de Blank, T.J. Schep, “Kinetic effects in collisionless magnetic reconnection” in *Proceedings of the 28th European Physical Society Conference on Controlled Fusion and Plasma Physics*, Madeira, 2001, to be published.

[53] B. Coppi, J. W-K. Mark, L. Sugiyama, and G. Bertin Phys., Ann. of Phys. **119** (1979) 370.

[54] G.W. Hammett, W. Dorland, F.W. Perkins, Phys. Fluids B **4** 2052 (1992).

[55] P.B. Snyder, G.W. Hammett, W. Dorland, Phys. Plasmas **4** 3974 (1997).

[56] N. Mattor, Phys. Plasmas **5** 1822 (1998).

[57] J. Egedal, A. Fasoli Phys. Rev. Lett. **86** 5047 (2001).

Summary

Collisionless magnetic reconnection has been studied for many years in relation with the earth magneto-tail dynamics, solar flares and fast magnetic field changes in high temperature, magnetically confined plasmas. In strongly magnetized, high temperature plasmas flux conservation binds together the dynamical evolution of field lines and plasma. Magnetic reconnection is a local violation of flux conservation. Depending on local temperature and density values, magnetic reconnection can be allowed by altogether different mechanisms, leading to a variety of structures and time scales. It was the quest for clarification of rapid phenomena as flares or disruption which forced to abandon explanations based on resistive effects and to turn toward collisionless mechanisms. The possible mechanism examined in this thesis are electron inertia in the parallel motion, resistivity (mainly as a comparative case), and wave particle effects. Accordingly, the reconnection is said to be Hamiltonian, resistive or collisionless, respectively.

In the first part of this thesis a fluid model is adopted to describe collisionless magnetic reconnection allowed by electron inertia. The process of fast magnetic topology rearrangement takes place on scale lengths comparable with the electron inertial skin depth. The effect of parallel electron compressibility is also included in the model. The governing equations have a Hamiltonian structure, hence the denomination Hamiltonian reconnection. When written in Lagrangian form, the system of equations is given by two generalized fluxes which are pointwise conserved by the velocity fields generated by the corresponding streaming potentials. Both fluxes and potentials are combinations of the magnetic flux and the electrostatic potential and their Laplacian's, the current and the vorticity. The reconnection process is interpreted in terms of the generalized fluxes which are conserved by the dynamics, due to the Hamiltonian structure of the governing two fluid equations.

The numerical solution of the Hamiltonian equations is investigated for two dimensional, externally forced systems and unstable configurations. In both the forced and the unstable cases, the nonlinear structures formed during the reconnection process are determined by the conservations of the generalized fluxes.

Differences in the spatial structures of the current and vorticity are evident, due to the different ways in which the reconnection is driven in the two cases. However, despite the complete difference in the reconnection drive, the topology of the solutions close to the X point is found to be the same in both the forced and unstable case. A common behavior is found also when sub-layer structures are compared. A faster than exponential scale collapse takes place close to the X point, and creates structures that are much narrower than the inertial reconnection layer.

In the second part of this thesis, the problem of reconnection in the presence of temperature gradients is addressed. Magnetic reconnection merges flux tubes which extend through regions of space that can be far apart and, in the presence of temperature gradients, have different temperatures. Far from the resonant layer the phase velocity of the reconnecting mode is much smaller than the thermal velocity, and the temperature becomes a flux function. Close to the resonant layer the phase velocity exceeds the thermal velocity and the equation of state approaches the adiabatic law. Between these two zones wave-particle resonance effects are important. Fluid models cannot describe resonance effects, and a kinetic treatment of the problem is required instead.

A drift-kinetic kinetic model is then employed, first, to study stationarily reconnecting nonlinear solutions for an X point topology. In this case resonances are absent. The flux tubes in the inflow regions have different, constant temperature on opposite sides of the X point. The reconnection of inflowing flux tubes with different temperatures is shown to generate temperature gradients in the outflow region such that the temperature along the reconnected flux tubes is not constant any more.

Second, wave-particle resonance effects in a topology with a finite size island chain are investigated. In contrast with Hamiltonian or resistive reconnection processes, wave-particle resonance effects take place in locations where the parallel wave vector is small but non-vanishing. Wave-particle resonance effects violate the frozen in law for the magnetic flux, and they allow reconnection to occur. The location in space of the resonances depends on the mode wave vector. When the resonance layer is located far from the island chain a single harmonic treatment of the resonance is possible. In this case the results of the well known ”thin island” approximation are recovered: an unstable mode exists which has frequency close to the diamagnetic frequency and growth rate proportional to the square of the electron inertia skin depth. In the opposite case of a large equilibrium island chain, especially when the resonance layer is close to the island separatrix, modes becomes strongly coupled over a wide range of wave numbers. In this thesis a model is used which includes the effects of the two-dimensionality of the equilibrium and keeps the resonance effects. It is found that the real part of the mode frequency is basically determined by diamagnetic effects, while the imaginary part is strongly affected by the coupling between different harmonics along field lines due to the presence of the finite size island chain. For perturbations with wavelength comparable with the island dimensions, those terms in the dispersion relation which are responsible for the instability in the thin island approximation are enhanced by the narrowing of the resonance of each coupled mode due to the presence of the finite size island chain.

Samenvatting

Magnetische reconnectie in botsingsarme plasma's wordt reeds vele jaren bestudeerd in verband met verschijnselen in de staart van de magnetosfeer van de Aarde, zonnevlammen en snelle veranderingen in de magnetische veldlijnen in zeer hete magnetisch opgesloten plasma's. In sterk gemagnetiseerde hoge-temperatuur plasma's zijn de evolutie van veldlijnen en de beweging van het plasma gekoppeld door een behoudswet voor magnetische flux. Magnetische reconnectie is een plaatselijke schending van dit fluxbehoud. Afhankelijk van de temperatuur en dichtheid bestaan er verschillende mechanismen voor magnetische reconnectie, met tot gevolg de vorming van structuren op uiteenlopende tijdschalen. Waarnemingen van snelle reconnectieprocessen zoals zonnevlammen en disruptieve instabiliteiten in laboratoriumplasma's leidden tot de conclusie dat eerder geopperde mechanismen voor reconnectie, gebaseerd op de electrische weerstand van het plasma, te traag waren en dat er andere mechanismen moesten bestaan die niet afhankelijk waren van botsingen tussen plasmadeeltjes. In dit proefschrift worden twee botsingsloze reconnectiemechanismen beschouwd: het ene gebaseerd op golf-deeltjewisselwerkingen in het plasma, het andere, bekend staand als Hamiltoniaanse reconnectie, gerelateerd aan de traagheid van de elektronen. Ter vergelijking wordt het beter bekende resistieve reconnectieproces beschouwd.

Het eerste deel van dit proefschrift maakt gebruik van een twee-vloeistoffenmodel voor de elektronen en ionen in het plasma. Dit model beschrijft botsingsloze reconnectie als gevolg van de traagheid van de elektronen. Snelle veranderingen van de magnetische topologie treden zeer plaatselijk op, in zones met een dikte vergelijkbaar met de door de elektronentraagheid bepaalde indringdiepte. De samendrukbaarheid van de elektronenvloeistof in de richting van het magneetveld levert een effect dat ook in het model is opgenomen. Het stelsel vergelijkingen kan worden beschreven met een Hamiltoniaan; vandaar de naam Hamiltoniaanse reconnectie. Het Lagrange-beeld van deze vergelijkingen laat twee gegeneraliseerde fluxen zien die behouden zijn omdat ze precies meebewegen met twee onsamendrukbare stromingsvelden. De twee fluxen én de bijbehorende stromingspotentialen zijn lineaire combinaties van de magnetische fluxfunctie, de electrische potentiaal en hun respectievelijke Laplacianen: de electrische stroomdichtheid en de vorticiteit. Dankzij de Hamiltoniaanse structuur kan het reconnectieproces begrepen worden in termen van de twee soorten flux.

De Hamilton-vergelijkingen zijn numeriek opgelost voor twee soorten tweedimensionale reconnectieproblemen: extern gedreven systemen en instabiele configuraties. Zowel in de extern gedreven als de instabiele gevallen ontstaan gedurende de reconnectie niet-lineaire structuren waarin het behoud van de gegeneraliseerde fluxen duidelijk herkenbaar is. De stroom- en vorticiteitsverdelingen laten duidelijke verschillen zien tussen de gedreven en instabiele processen, maar de oplossingen rond het X-punt (waar de reconnectie plaatsvindt) zijn in beide gevallen gelijk. In beide gevallen ontstaat in het X-punt bovendien een structuur die nog dunner is dan de inertiële reconnectielaag. Opmerkelijk is dat deze substructuur zich sneller dan exponentieel vernauwt.

Het tweede deel van dit proefschrift is gewijd aan het probleem van reconnectie in de aanwezigheid van temperatuursgradiënten. Magnetische reconnectie zorgt voor de versmelting van fluxbuizen die ver uiteengelegen delen van het plasma met elkaar verbinden en daardoor duidelijk verschillende temperaturen hebben. Ver van de reconnectiezone geldt dat de fasesnelheid van de reconnectiemode veel kleiner is dan de thermische snelheid van de elektronen, zodat de temperatuur constant is op veldlijnen. In het centrum van de reconnectiezone is de fasesnelheid juist groter dan de thermische snelheid zodat daar een adiabatische toestandsvergelijking geldt. Tussen deze twee gebieden ligt en zone waar golf-deeltje resonanties een rol spelen. Zulke resonanties kunnen niet met vloeistofmodellen worden beschreven: een kinetische aanpak van het probleem is vereist.

Omdat geen enkele toestandsvergelijking overal geldig is wordt een driftkinetisch model geïntroduceerd. Ten eerste wordt dit model gebruikt om een stationair reconnecterend plasma in de vorm van een niet-lineaire X-punt structuur te bestuderen. Doordat de stroming stationair is ontbreken golf-deeltjeresonanties. De fluxbuizen die naar het X-punt toe bewegen hebben aan weerszijden van het X-punt verschillende constante temperaturen. Door reconnectie vormen die fluxbuizen met verschillende temperaturen nieuwe fluxbuizen die zich van het X-punt verwijderen. De temparatuur op deze fluxbuizen is niet constant. Ten tweede is het drift-kinetisch model toegepast op golf-deeltje-effecten in de buurt van een magnetische eilandketen met een eindige dikte. Een verschil met Hamiltoniaanse en resistieve reconnectie is dat golf-deeltje resonanties alleen daar plaatsvinden waar het golfgetal parallel aan het magneetveld klein (maar niet precies nul) is. Reconnectie treedt op doordat ten gevolge van deze golf-deeltjeresonanties de veldlijnen de plasmastroming niet meer precies volgen. De lokaties van de resonanties hangen af van het golfgetal van de mode. Wanneer de resonantie ver van de eilandketen af ligt kan dit ene golfgetal de hele mode beschrijven. Deze benadering, die geldig is als de eilandketen uiterst dun is, is uit de literatuur bekend: er is een instabiele mode met een groeisnelheid evenredig aan het kwadraat van de inertiële indringdiepte gecombineerd met een oscillatiefrequentie vergelijkbaar met de diamagnetische frequentie. Het tegenovergestelde geval, van een keten van grote eilanden, wordt in dit proefschrift behandeld. Deze benadering laat resonanties toe die dicht bij de eilandseparatrix liggen. In dit geval is er een sterke koppeling tussen een groot aantal golfgetallen. De benadering in het proefschrift houdt rekening met die twee-dimensionale vervorming van de resonante zones. De resultaten laten zien dat de oscillatiefrequentie van de mode door diamagnetische effecten wordt bepaald, terwijl de groeisnelheid sterk beïnvloed wordt door de koppeling tussen verschillende golfgetallen. Wanneer het golfgetal van de mode vergelijkbaar is met die van de eilandketen, is de groeisnelheid beduidend hoger dan in het geval van dunne eilanden. Dit komt doordat de resonantiezones veel nauwer zijn wanneer ze dicht bij een dik eiland liggen.

Curriculum Vitae

Gherardo Valori

was born on July 28*th* 1969 in Montecatini Terme, Italy

attended the secondary school (Liceo Scientifico Sperimentale) in Pescia

studied physics at the University of Florence from 1989 to 1996

did his community service in the Youth Center of Fiesole in 1995-96

wrote his thesis ”Effetti girocinetici di rilevanza astrofisica in fluidi magnetoidrodinamici” (“Gyrokinetic effects of astrophysical relevance in magneto hydrodynamic fluids”) under the wise and frank guide of Giorgio Einaudi

obtained on July 15*th* 1996 the master degree with *cum laude*

started his PhD in the FOM-Institute for Plasma Physics ”Rijnhuizen” in June 1997, which resulted in this thesis

Acknowledgements

My gratitude goes to Theo Schep, my promoter, for the opportunity to work in his group. During the years of my PhD, discussion in physics and life matters became more and more intense, as I could have found no better trainer for the lessons of Sun Tzu. A particular mention shall be devoted to his patience fighting against the sloppiness of my writing, and sometimes of my thinking, while editing this thesis. To Hugo de Blank I owe my largest debt of gratitude for my work at ”Rijnhuizen”. As a supervisor he was always ready to find time to answer my questions, no matter how silly they were. Generous in explanations, Hugo gave me the opportunity to learn the many aspects of many problems, to enjoy his enthusiasm and playful attitude in challenging all of them. Beside the job, I received from Hugo spontaneous help and understanding in dealing as a foreigner with the wildest of the Dutch habits. I suspect for this I have to thank Cristina too.

I like to thank all the members of theory department which resides in the so-called—not without some presumption— ”kastel”. Among the senior theoreticians which worked there, I want to thank in particular Jan Rem, Boris Kuvshinov, and Valdimir Lakhin. Jan was the person who gave me the exact measure of how bad my English was when I arrived in The Netherlands. It took me quite a long time before I managed to decrease the number of lines on his forehead below fifteen while I was trying to communicate with him. Boris is the personification of wit. His knowledge in plasma physics is equated only by his love for Russian jokes, admiration for his teacher, contempt of much of the scientific literature, both published and to come. Hence, of course, he never got a chance to have a glimpse at my thesis. Vladimir I thank because he is Vladimir: friendly, relaxed, helpful. I only regret the short time I could enjoy his company.

Jeroen Bergmans and Bart van der Holst have been my PhD mates since the very beginning. Involuntarily, they have been also my training with Dutch attitude in working relations. It is from the weird times of the summer school in Spa that we managed to cross cultural borders, thanks to Adams, some coffee, and lots of chats. Like schoolmates, indeed.

The atmosphere in the institute would have been much grimmer if we could not rely on the good mood and good heart of our reception staff. I do appreciate

the deep solidarity I got from Loes van de Ven, as an expert in Italian idiosyncrasy, in some particularly gray, wet or foggy days.

I am glad to thank also Daniela Grasso, Giorgio Einaudi, and Francesco Pegoraro. In different ways, they have been a valuable help and a guide in my job.

With Aurora (Hajnal), Arnold and Tarig a friendship developed during these years, special with each of them, and each one invaluable. I am happy that I met you, and that I will keep enjoying your friendship in the years to come. Many other friends, whose importance is enormous, are not mentioned here. I will have the time and the pleasure to thank them personally.

This thesis and the time I spent in The Netherlands have also one more important contribution: I could have never even seriously started without the colors and the life of Amsterdam.

To Ricarda, my brother, and my parents goes my deepest love. You have been charged of all the bad moods and angers that I was not able to leave out, and from you I subtracted care and time. Thank you. Ma fra i molti che ho trascurato in questi anni la persona a cui devo maggior riconoscenza e’ mia nonna. La lontanaza non ha fatto altro che rafforzare il legame e l’ammirazione che ti porto.

Gherardo, Amsterdam 2001